Material and structural mechanical modelling and reliability of thin-walled bellows at cryogenic temperatures. Application to LHC compensation system

Cédric Garion

September 2003

N° d'ordre: 1431
EDSPIC: 281

UNIVERSITÉ BLAISE PASCAL - CLERMONT II

ECOLE DOCTORALE
Sciences pour l'ingénieur de Clermont Ferrand

THÈSE

présentée par

Cédric Garion

DEA Mécanique et Matériaux, ENS de Cachan

pour obtenir le grade de

DOCTEUR D'UNIVERSITÉ

Spécialité: Génie Mécanique

Material and structural mechanical modelling and reliability of thin-walled bellows at cryogenic temperatures.

Application to LHC compensation system

soutenue publiquement le 17 septembre 2003 devant le jury:

M. Lemaitre J.	Université Paris VI	Président
M. Cailletaud G.	Ecole Nationale des Mines de Paris	Rapporteur
M. Jullien J. F.	Institut National des Sciences Appliquées, Lyon	Rapporteur
M. Lemaire M.	Université Blaise Pascal, Clermont Ferrand	Examinateur
M. Robert J. L.	Université Blaise Pascal, Clermont Ferrand	Examinateur
M. Skoczen B.	Cracow University of Technology, Poland & CERN, Geneva, Switzerland	Examinateur
M. Marquis D.	Ecole Normale Supérieure de Cachan	Directeur de Thèse

Laboratoire de Recherches et Applications en Mécanique Avancée (LaRAMA)
Institut Français de Mécanique Avancée, Clermont-Ferrand, France

The present work has been carried out during two and a half years at CERN in collaboration with the University of Clermont-Ferrand, under the supervision of Dr. Blazej Skoczen (Section Leader at CERN, Associate Professor at the Cracow University of Technology) and Professor Didier Marquis (Head of the Institut Français de Mécanique Avancée). I wish to express my gratitude to Prof. Didier Marquis for many valuable discussions, suggestions and encouragements. Infinitely thanks to Blazej for all he did during my Ph.D period at CERN.

I insist on thanking Prof. Lemaitre, who did me the honour of leading my Ph.D. board, Prof. Cailletaud and Prof. Jullien, who have the laborious task of reviewing my Thesis and Prof. Robert and Prof. Lemaire, who kindly accepted to participate in the board.

It has been a great privilege to work at CERN in the Large Hadron Collider Division. I would like to say how grateful I am to all the members of the Cryostats and Integration Group, especially the Group Leader Dr. A. Poncet and his deputy C. Hauviller, for their welcome and support. Thanks to Alain Bastard, for his support and his help in the fatigue machine assembly and the fatigue tests. I would like to extend my thanks to all those who have helped me in my work.

Finally, I address these last few lines to thank all my family for their support. My greatest debt is to Coralie, who, in addition to providing me the encouragements, endured with great understanding my long hours of the study.

CERN, Geneva, August 2002

Contents

List of Figures

List of Tables

Notation and Definitions

Latin Letters

a	Crack length
A	Phase transformation intensity parameter
C	Hardening modulus
C_0	Hardening modulus of austenite
$\underline{\underline{C}}$	Material damage parameter tensor
C_f	EJMA correction factor
d	Imperfection parameter
d_g	Average diameter of grain size
D	Isotropic damage variable
D^α	Isotropic damage variable in martensitic phase
D^γ	Isotropic damage variable in austenitic phase
$\underline{\underline{D}}$	Second order damage tensor
D_b	Inside diameter of bellows
D_{cr}	Critical damage at crach initiation
D_m	Mean diameter of bellows
D_o	Outside diameter of bellows
E_T	Modulus of elasticity at temperature T
$\tilde{E}$	Effective Young modulus
E_d^e	Elastic deformation energy
$\underline{\underline{E}}_0$	Homogeneous overall strain
$\underline{\underline{\underline{\underline{E}}}}$	Fourth-order elasticity stiffness tensor
$\underline{\underline{\underline{\underline{E^*}}}}$	Hill influence tensor
$\underline{\underline{\underline{\underline{E_H}}}}$	Homogenised fourth-order stiffness tensor
$\underline{\underline{\underline{\underline{E_{ps}}}}}$	Elastic stiffness tensor in plane stress

$\underline{\underline{\underline{\underline{E_{MT}}}}}$	Fourth-order stiffness tensor obtained by Mori-Tanaka homogenisation
$\underline{\underline{\underline{\underline{E_t}}}}$	Fourth-order tangent stiffness tensor
f	Failure density function
f_c	Yield surface
F_d	Potential of dissipation
F	Cumulative failure distribution function
h	Material parameter of hardening
H	Kinematic hardening modulus
$\underline{\underline{\underline{\underline{H}}}}$	Fourth-order tangent stiffness tensor
$\underline{\underline{I}}$	Identity tensor
k	Compressibility modulus
L_b	Free length of bellows
$\underline{\underline{\underline{\underline{M}}}}$	Damage effect tensor
n_c	Number of convolutions of bellows
n_p	Number of plies of bellows
$\vec{n}$	Normal unit vector
N_f	Number of cycles to failure
$\bar{N}_f$	Average number of cycles to failure
p	Accumulated plastic strain
p_D	Accumulated plastic strain threshold for martensitic transformation
p_ξ	Accumulated plastic strain threshold for damage
$\underline{\underline{\underline{\underline{P^\gamma}}}}$	Hills tensor
q	Pitch of bellows convolution
$\underline{\underline{s}}$	Deviatoric stress tensor
R	Isotropic hardening
R	Reliability
R_∞	Saturation level of isotropic hardening
R_ν	Triaxiality function
S	Sectional area
S_D	Damaged sectional area
t	Thickness of one ply
t_p	Corrected thickness of one ply
$\vec{u}$	Displacement vector
Δv	Relative volume change
w	Convolution depth of bellows
w_e	Elastic strain energy density
$\underline{\underline{X}}$	Back stress tensor

Y	Strain energy density release rate
Y_{cr}	Critical Strain energy density release rate at crach initiation
$\underline{\underline{Y}}$	Strain energy density release rate tensor

Greek Letters

α	Dilatation coefficient
$\underline{\underline{\hat{\alpha}}}$	Dilatation tensor
$\underline{\underline{\alpha}}$	Back strain
β	Apportionement isotropic/kinematic hardening parameter
β	Weibull shape parameter
χ	Magnetic susceptibilty
δ	Weibull parameter
Δ	Axial displacement of bellows
$\Delta\epsilon_p$	Plastic strain range
ϵ^p	Plastic strain
ϵ_D^p	Damage plastic strain threshold in pure tension
$\underline{\underline{\epsilon}}$	Strain tensor
$\underline{\underline{\epsilon}}^{bs}$	Bain strain tensor
$\underline{\underline{\epsilon}}^{e}$	Elastic strain tensor
$\underline{\underline{\epsilon}}^{p}$	Plastic strain tensor
$\underline{\underline{\epsilon}}^{PT}$	Distorsionnal strain tensor
$\underline{\underline{\epsilon}}^{th}$	Thermal strain tensor
$\underline{\underline{\epsilon}}_f$	Free strain tensor
$\underline{\underline{\epsilon}}_f^*$	Equivalent free strain tensor
$\underline{\underline{\epsilon}}'$	Strain tensor perturbation
$\underline{\underline{\epsilon}}^{L}$	Linear part of strain
$\underline{\underline{\epsilon}}^{Q}$	Quadratic part of strain
$\dot{\lambda}$	Failure rate function
$\dot{\lambda}$	Plastic multiplier
μ	Shear modulus
μ	Magnetic permeability
μ	Bellows stiffness correction factor
μ	Mean time to failure
ν	Poisson's ratio
Ψ	Helmholtz free energy
ρ	Mass density
σ_{eq}	Equivalent stress

σ_h	Hydrostatic stress
σ_u	Ultimate stress
σ_y	Yield stress
$\underline{\underline{\sigma}}$	Cauchy stress tensor
$\underline{\underline{\tilde{\sigma}}}$	Effective stress tensor
$\underline{\underline{\sigma}}^{\alpha}$	Stress tensor in martensitic phase
$\underline{\underline{\sigma}}^{\gamma}$	Stress tensor in austenitic phase
$\underline{\underline{\sigma}}'$	Stress tensor perturbation
Σ	Triaxiality
$\underline{\underline{\Sigma}}_0$	Homogeneous overall stress
$\underline{\underline{\tau}}$	Polarisation
ξ, $\xi_{\alpha'}$	Volume fraction of α' martensite
ξ_L	Martensite content limit

Operators

$< x >_{\Omega}$	Average value of the variable x on the domain Ω
$< x >$	Mac Auley bracket
$[\![x]\!]$	discontinuity of the variable x across a surface
H	Heaviside function

Chapter 1

Introduction

To well-understand the primary importance of this study, it is necessary to explain the framework of the work, carried out for two and a half years at CERN.

1.1 Lepton and hadron colliders in high energy physics at CERN

The modern high energy physics needs very sophisticated and complex tools in order to explore world of elementary particles constituting the matter. One of the most important aims over the past 30 years was confirmation of the so called Standard Model which assumes that the fundamental constituents of matter form three families of quarks and leptons. The relevant scientific tools are called accelerators, storage rings and colliders and their main function is to produce, accelerate, store and collide the beams of particules in order to search for the new elementary events, announcing the potential discoveries, and to provide more statistics for the already known reactions.
CERN's accelerator complex includes particle accelerators and colliders. It can handle beams of different types of particles (electrons, positrons, protons, antiprotons and "heavy ions"). Each type of particles is produced in a different way, but then passes through a similar succession of acceleration stages, moving from one machine to another. The first steps are usually provided by a linear accelerator, followed by a larger circular machine: Proton Synchroton (PS, 1959), Super Proton Synchroton (SPS, 1976), Large Electron Positron collider (LEP, 1989) and in the future Large Hadron Collider (LHC) (Fig. 1.1).

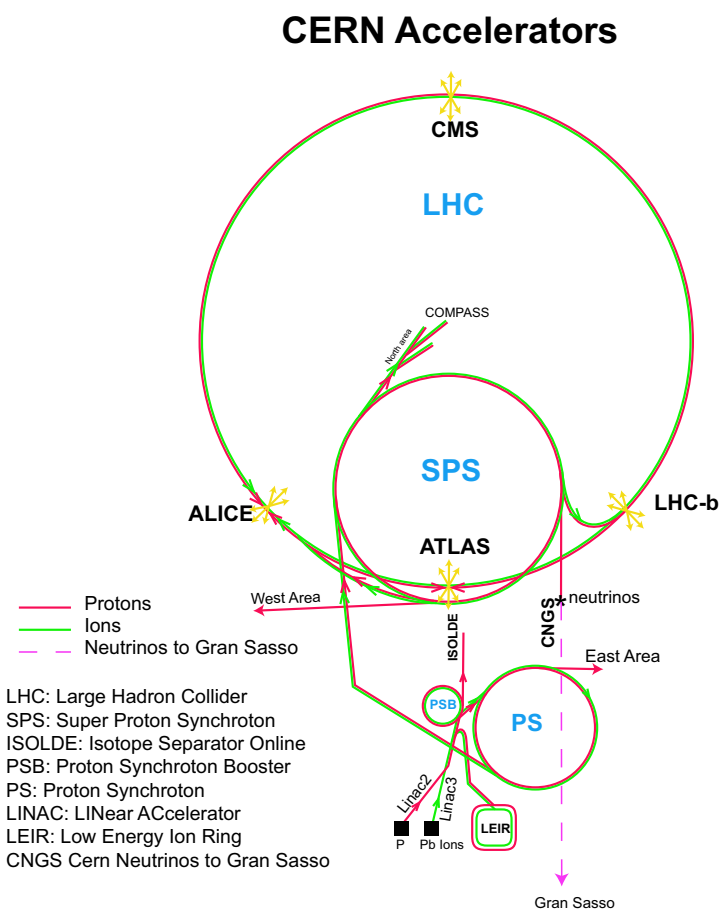

Figure 1.1: CERN's accelerator complex

1.2 Technologies applied in the construction of hadron colliders

The structure of a circular accelerator comprises usually accelerating cavities, bending main dipoles (MB) to keep the beam on its circular orbit and focusing/defocusing main quadrupole magnets. A typical cell of the LHC is shown Fig. 1.2. It is composed of 6 main dipoles (MB) and 2 Short Straight Section (SSS) containing the main quadrupoles.
The LHC will consist of two "colliding" synchrotons installed in the 27 km tunnel. Two superconducting magnetic channels will accelerate the protons to 7 TeV[1], after which the beams will counter-rotate, colliding at the experiments. The magnetic channels will be housed in the same yoke and cryostat, a unique configuration that not only

[1] 1 TeV=10^{12} eV

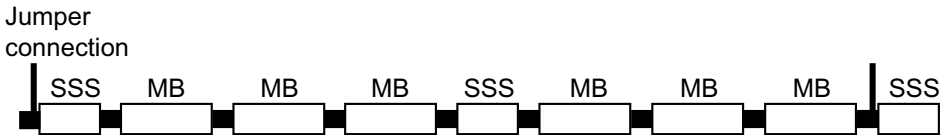

Figure 1.2: The LHC cell: Bending dipoles (MB) and focusing/defocusing main quadrupoles (SSS)

saves space but also gives 25 % cost saving over separate rings. High energy beams need high magnetic bending fields. To bend 7 TeV protons around the ring, the 1232 LHC dipoles (MB) must be able to produce fields of 8.36 T [1]. The dipole cold mass consists of 2 coils per aperture clamped around the cold bore by a common austenitic steel collar surrounded by an iron yoke and a shrinking cylinder, for a total mass of about 23.8 tons (Fig. 1.3).

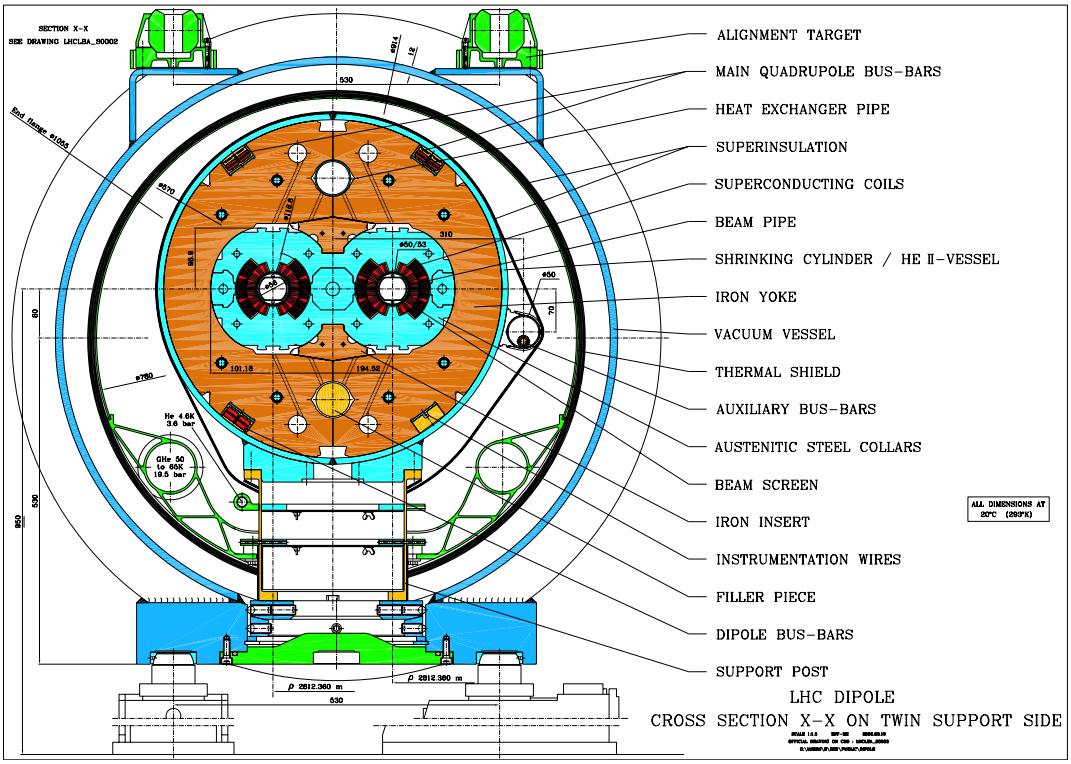

Figure 1.3: Cross section of a cryodipole in the LHC

The total length of Niobium-Titanium supraconductor per magnet is about 1180 m. Nominal current is about 12 kA for a nominal field of 8.36 T and a stored energy of 7.1 MJ per magnet. The service temperature of supraconducting coil is 1.9 K. The

cryogenic technology chosen for the LHC uses superfluid helium, which has unusually efficient heat transfer properties, allowing kilowatts of refrigeration to be transported over more than a kilometer with a temperature drop of less than 0.1 K. LHC superconducting magnets will float in a 1.9 K bath of superfluid helium at atmospheric pressure. This bath will be cooled by low pressure liquid helium flowing in heat exchanger tubes threaded along string of magnets. During initial cooldown of 31000 tons of material 700000 litres of liquid helium will be required. The cryogenic lines of the accelerator are linked to a seperated cryogenic transfert line via a jumper connection (Fig. 1.2) After cool-down, the thermal contraction is about 70 m. Compensation systems, composed mainly of bellows expansion joints, are installed between magnets. To achieve the maximum beam energy, the magnetic length has to be as high as possible. In the LHC, the ratio of non-magnetic to magnetic zones is close to 3 %. This implies an extremely compact design of interconnection system. An interconnection in the tunnel is illustrated in Fig. 1.4.

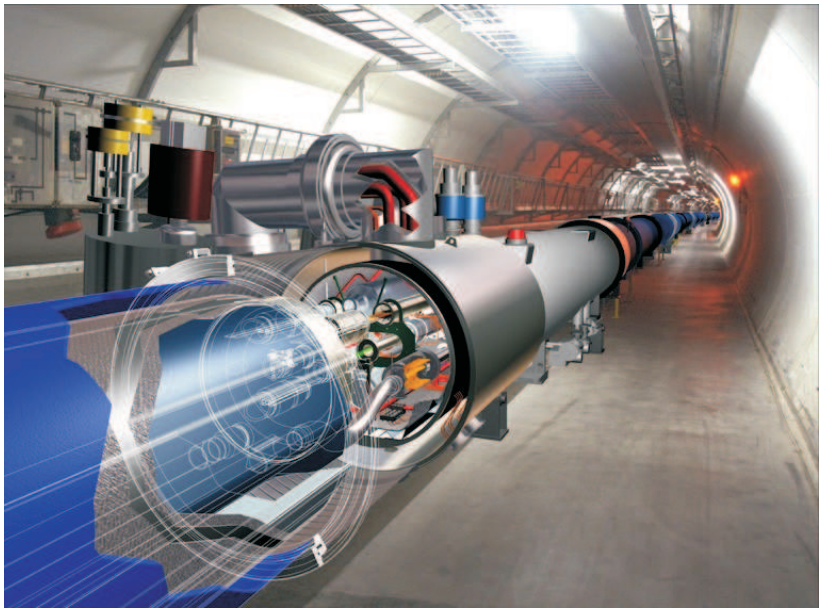

Figure 1.4: LHC in the tunnel - virtual reality (interconnections well visible)

The LHC is composed of about 1700 main magnets, dipoles (MB) and quadrupoles (SSS) and about 1700 main magnet-to-magnet interconnection zones. The function of the LHC interconnections are as follows [2]:

- continuity of the beam transport system
- continuity of the beam and insulation vacuum
- continuity of the electrical powering system

- continuity of the cryogenic system
- continuity of the thermal shield
- compensation for the thermal contraction of the adjacent components
- transverse flexibility for the alignment of the cryo-magnets

The interconnection can be decomposed into three systems: powering electrical system, beam image current continuity system and mechanical system composed of bellows expansion joints. The framework of this thesis covers to the thermo-mechanical compensation system (bellows expansion joints). It has to assure the continuity of the interconnection lines (cryogenic lines and beam vacuum lines) and compensate for the thermal contraction of magnets and thermal shields (Fig. 1.5). Compact design of the compensation elements, subjected to severe service conditions (low temperatures, high pressure, large deformation due to the thermal contraction of magnets) induces to use optimized bellows expansion, working in a non-standard low-cycle fatigue regime (cf. [3]).

1.3 Reliability aspects in design and optimisation of complex accelerators of particles

High availability level of the LHC is required. Each intervention needs at least 3 days for the warm-up, 5 days for the cool-down, which represents considerable time losses for the experiments. Clearly, it is indispensable to avoid any major intervention during the exploitation of the LHC.
All system are linked to each others. A high reliability level is required for each system of such machine.
The analysis of reliability of the mechanical compensation system is based on the study of behaviour of the materials at low temperatures, which means plasticity, ductile damage and phase transformations (cf. [4]). Two approaches are developed in the present work:
An experimental approch, that consists in testing the components under certain conditions. It is clear that it is very difficult to test the bellows under the real conditions (a fatigue test of bellows subjected - in laboratory conditions - to a cyclic axial displacement, that is associated with a variation of the temperature between 293 K and 1.9 K, under an internal pressure of 20 bars is difficult, time consuming and very expensive). The bellows are rather tested under particular conditions, namely under constant temperature. That gives an important knowledge concerning the dispersions

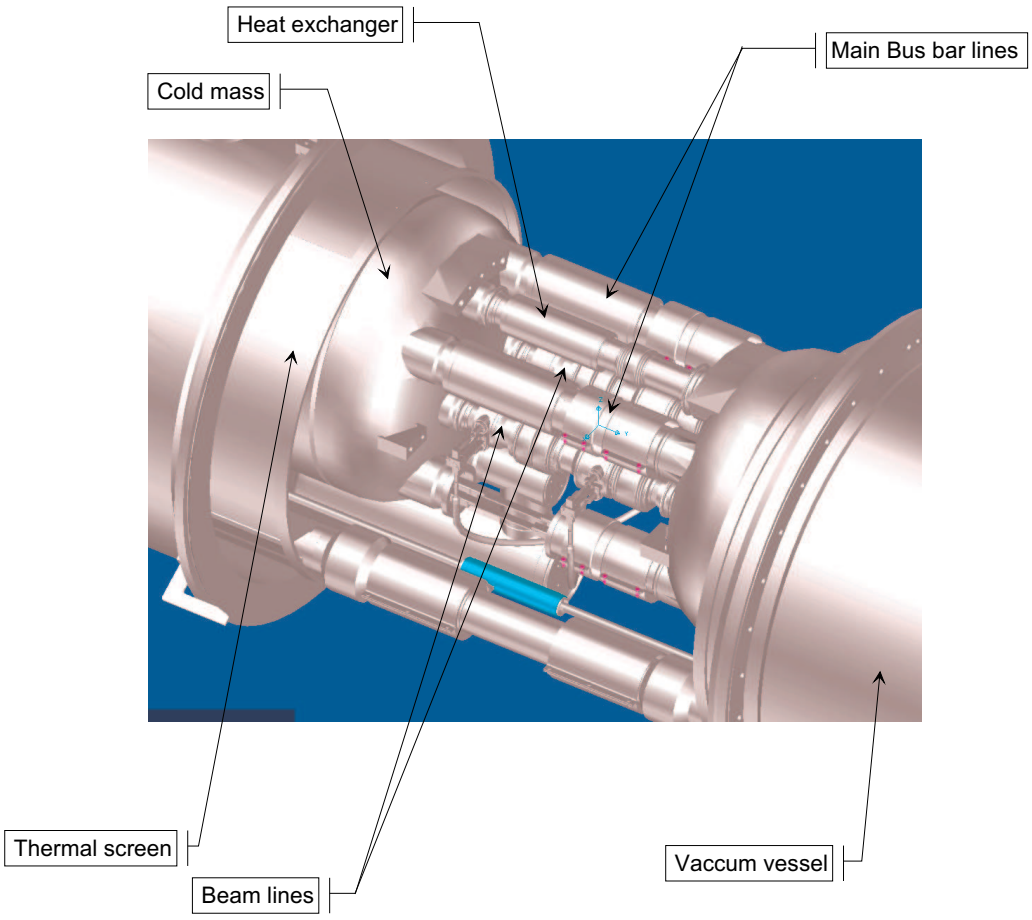

Figure 1.5: Interconnection between magnets of the LHC

of the results and allows to carry out cross-check between the numerical simulation and the experiments.
The second approach consists in a numerical simulation of the real thermo-mechanical cycle. Based on the FE method and a post-processor treatment, it allows to simulate behaviour of the bellows under complex loading. This approach implies modeling the behaviour of the materials at low temperatures. There are relatively few publications on this topic; most of the papers cover the behaviour of the materials at room or at higher temperatures. Up till now, the standard relation of Manson-Coffin was used to predict the low-cycle fatigue life of bellows containing strong plastic strain fields ([3, 5, 6]).

$$N_f^{\beta} \Delta\epsilon_p = C \tag{1.1}$$

where N_f denotes the fatigue life, $\Delta\epsilon_p$ the plastic strain range over a cycle, C and β are two material constants. This approach does not take into account the variation of

material properties during the lifetime of bellows: the variation due the temperature over one cycle and the variation due to the metallurgical change (phase transformation) during cycling. A more complex method based on the damage mechanics and the strain induced martensitic transformation is used to predict the lifetime of the components. The instability of the bellows turns out to be another failure mode. The instability of the mechanical compensation system can be decomposed into three categories:

- Global instability of the interconnect (pipe-bellows-pipe). The whole interconnect, under internal pressure, buckles as an Euler beam. Stability condition depends on the behaviour in flexure of the bellows and of the adjacent tubes. This instability is not analysed in this Thesis but has been solved by Skoczen [3].
- Semi-global instability. General shape of the bellows changes and the tubes of the line stay "rigid".
- Local instability. Thin-walled corrugated shell collapses locally. The impact on general shape of bellows remains small. The equation, describing this phenomenon, has been developed by Axelrad [7]. Here, an eigenvalue analysis has been used to define the stability.

The influence of material properties on the local stability is analysed in the further part of the present Thesis.

Chapter 2

Bellows expansion joints in the LHC interconnections

2.1 Introduction

Bellows expansion joints are employed in piping systems to absorb differential thermal contraction while containing the system pressure (or vacuum). The properties of an expansion joint depend mainly on two issues:

- The material: the bellows material must be compatible with the flowing medium, the external environment and the operating system temperature (§ 2.2).
- The design of the convolutions: the design shall correspond to the existing standards and accepted methods [8] and leads to definition of the mechanical properties of the bellows (stiffness, pressure capacity, stability, fatigue life, etc) (§ 2.3).

The reliability of the bellows expansion joints depends to some extent on the manufacturing quality. It includes the quality of the material and of the manufacturing process. The high level of reliability required for the LHC and - specifically - for the interconnection components (§ 2.4) implies a special attention to these two aspects.

2.2 Choice of material for cryogenic applications

2.2.1 Chemical composition and physical properties

The choice of material is a crucial point for the design of the bellows, that are subjected to severe conditions. They have to resist to cryogenic temperatures (down to 1.9 K),

radiation (annual dose up to $\sim$ 1000 Gy/y), mechanical loading (pressure, axial and transversal displacements). The bellows expansion joints are installed at the ends of the magnets, within the region of the stray field. The material used must therefore have a relative initial magnetic permeability of not more than 1.005 in a magnetic field of 80000 A.m^{-1} (magnetic induction of 0.1 T) at room temperature. The material must have a low specific surface outgassing rate (typically $\simeq 10^{-8}$ Pa.m^3.s^{-1}.m^{-2}). Commonly, austenitic stainless steels are used for cryogenic applications because of their ductility at low temperatures, their magnetic and vacuum properties. In order to avoid the ductile-fragile transition, high nickel content is used. The chosen material is the AISI 316L or X2CrNiMo17-12-2 (European notation). The specification of the chemical composition of the material is given Table 2.1 (cf. [9]).

Element	Content wt%
Cr	16.00 - 18.50
Ni	11.00 - 14.00
C	0.03 max.
Si	1.00 max.
Mn	2.00 max.
Mo	2.00 - 2.50
N	0.05 max.
P	0.03 max.
S	0.01 max.
Fe	Remainder

Table 2.1: Chemical composition of the 316L stainless steel for cryogenic applications

The structure after full quenching is supposed to be completely austenitic. The grain size has to be lower than 40 μm [9].

2.2.2 General mechanical behavior of austenitic stainless steel at low temperatures

Martensitic transformation and magnetic permeability.

The Fe-Cr-Ni stainless steels are commonly used to manufacture components of the superconducting magnets and the cryogenic transfer lines since they retain their ductility at low temperatures and are paramagnetic [3]. Under certain conditions the steels undergo martensitic transformation at cryogenic temperatures that lead to a considerable evolution of material properties and to a ferromagnetic behaviour. The martensitic transformations are induced mainly by the plastic strain fields and amplified by the high magnetic fields. Spontaneous transformations due to the cooling

process - identified with respect to some alloys - are not observed with respect to the most often used grades 304LN, 316L, 316LN. The stainless steels of series 300 show at room temperature a classical γ -phase of face centred cubic austenite (FCC). This phase may transform either to α' phase of body centred tetragonal ferrite (BCT) or to a hexagonal ϵ phase. The most often occurring $\gamma - \alpha'$ transformation leads to formation of the martensite sites dispersed in the surrounding austenite matrix. The spontaneous martensitic transformation starts at the temperature T_S and continues until the temperature drops below the temperature of termination of the process T_f. The strain induced transformation starts at much higher initiation temperature T_d. In the course of the strain induced transformation the martensite platelets modify the FCC lattice leading to local distortions. The amount of the martensite depends on the chemical composition, temperature, stress state, plastic strains and exposure to a magnetic field. It is well known that the solutes like Ni, Mn and N considerably stabilise the γ-phase. For instance the strain induced martensitic content in the grades 304LN, 316LN at low temperatures is much lower than in the grades 304L, 316L for the same level of plastic strain [10]. The martensitic transformation can be promoted by exposure to high magnetic field. The influence of the applied magnetic field on the martensitic fraction is defined by the following relation [11]:

$$Fr_\alpha(T,H) = Fr_\alpha(T,0)e^{C\frac{HM}{T}} \tag{2.1}$$

where $Fr_\alpha(T,H)$ denotes the martensitic fraction at the temperature T and field H, M stands for magnetic moment of α and C is a constant.

The increase in martensite fraction promoted by plastic deformation can be detected by measuring the magnetic permeability μ. The evolution of μ at low temperature corresponding to monotonic straining as well as to the cyclic loads for 304L and 316L stainless steels was investigated by Suzuki and al., 1988 [10]. Larbalestier and al. show that the magnetic permeability is linearly related to the martensite content for low martensitic fraction [12] .

Mechanical properties of stainless steels at low temperatures

Tensile tests at cryogenic temperatures are rather complex and expensive since the specimen must be immersed in a bath of liquid nitrogen (77 K) or liquid helium (4 K) inside a vacuum-insulated cryostat. The strains are generally measured by strain gauges or extensometers for larger strains (at rupture). Dependence of the material properties of stainless steels at low temperatures on the strain rate was discussed by Reed et al. [13–15] and Ogata et al. [16–19]. The tests have been carried out on samples made of three different alloys: 310, 304L and 316LN. It turned out that the yield point, elongation and reduction of cross-sectional area were rather insensitive to the strain rate. On the other hand, the ultimate strength σ_{ult} showed a considerable decrease above a critical value of the strain rate. This value of about $2.2.10^{-3}$ s^{-1} was nearly

identical for all the alloys. Below this value the ultimate strength increases slowly with the strain rate (Fig. 2.1, [13]).

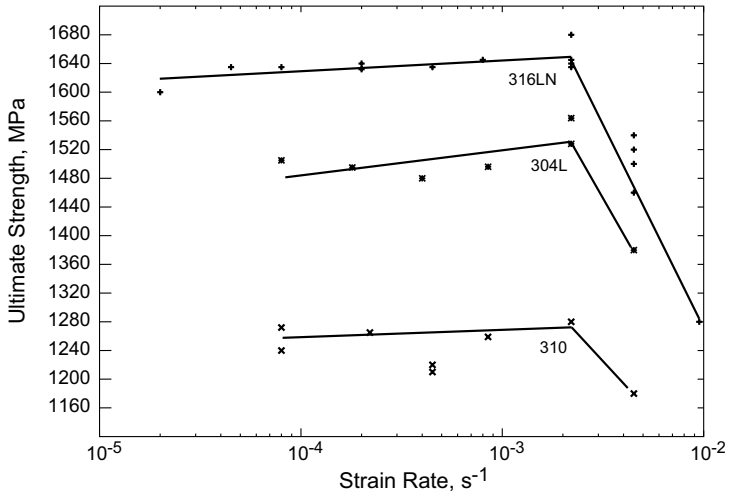

Figure 2.1: Ultimate strength at 4 K as a function of the strain rate for different grades of austenitic stainless steels

The mechanical strength of 316L was investigated by Suzuki et al. [10]. The tensile tests were carried out at the strain rates not exceeding 10^{-3} s^{-1}. Thus, the measured ultimate strength was rather stable (rate independent). Mechanical properties of grade 316L at room and at cryogenic temperatures are shown in Table 2.2 [10]. They have been obtained from specimens, prepared from the midthickness of 65 mm thick plate (with axis in the rolling direction). The diameter of test section is from 6 mm to 14 mm.

Temperature [K]	Young modulus [MPa]	Yield strength [MPa]	Tensile strength [MPa]	Elongation [%]
293	191 000	216	529	65
77	206 000	314	1235	49
4	206 000	431	1441	48

Table 2.2: Mechanical properties of grade 316L stainless steel

Mechanical properties of stainless steel depend on the amount of cold work. Generally, higher cold work enhances the yield strength and the ultimate strength and reduces the elongation (ductility of the material). They depend too on metallurgical parameters:

- the chemical composition (even for the same grade)

- the grain size: the yield strength is linearly related to $d_g{}^{-\frac{1}{2}}$ (where d_g is the average grain size) according to the well-known Hall-Petch relationship (2.2) (cf. [20, 21]).

$$\sigma_y = \sigma_0 + m d_g{}^{-\frac{1}{2}} \tag{2.2}$$

The relationship has been checked on two 316LN alloys by Reed et al. [22, 23] and on 304 and 316 stainless steels by Simon and Reed [24].

Serrated yielding

The process of plastic flow of stainless steels at cryogenic temperatures may be discontinuous (in terms of $\mathrm{d}\sigma/\mathrm{d}\epsilon$). The phenomenon of discontinuous plastic flow at cryogenic temperatures is called 'serrated yielding' (Fig. 2.2). The material presents Drucker's type instability (cf. [25, 26]). This is most probably due to low specific heat and thermal conductivity of stainless steels at low temperatures. The near-adiabatic local conditions lead to a conversion of a large portion of plastic work to heat and to local temperature rise. This effect has been shown by Reed et al. [13, 27] and Ogata et al. [19]. The local increase of the temperature may reach about 40 K. The increase in temperature leads to further local evolution of material properties. Transgranular shear bands develop locally. Since the deformation rate in the shear bands in much higher than the strain rate imposed on the sample, the global strain 'jumps', accompanied by a decrease of load. These phenomena were studied in detail by Tobler et al. [28], Reed et al. [13, 27], Ogata et al. [17, 18, 29] and Obst et al. [30, 31].

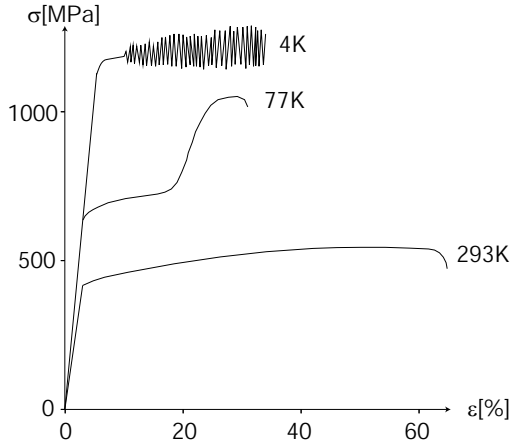

Figure 2.2: Tensile test of 316LN stainless steel at cryogenic temperatures (strain rate about 5.10^{-4} s^{-1}

It is worth pointing out that this phenomenon is highly rate dependent. It is observed

for higher strain rates ($> 10^{-3}$ s^{-1}). The temperature rise is rate dependent too. Measurements have been carried out by Ogata et al. [29] on the grade 316LN stainless steel samples equipped with thermocouples and subjected to cyclic load. The samples were cycled under the strain range of 3 % and under the frequencies 0.01-0.5 Hz. A good correlation was found between the thermal spikes and serrated yielding for low frequencies: The maximum temperature rise was of 10 K for the frequency of 0.01 Hz, of 18 K for 0.1 Hz and of around 40 K for the frequency of 0.5 Hz. More precise measurements have been carried on 316LN stainless steel by Obst (cf. [31]).
Simple one-dimensional models of serrated yielding were discussed by Skoczen [3].

Thermal strain

For austenitic stainless steels, the thermal contraction curve as a function of the temperature is shown in Fig. 2.3.

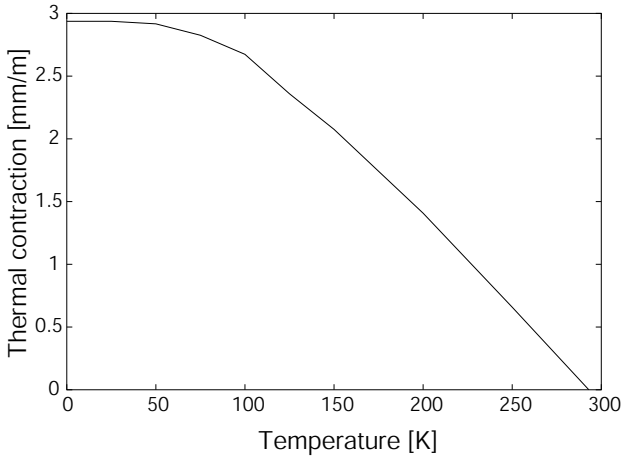

Figure 2.3: Thermal contraction as a function of the temperature for stainless steels

The expression of the thermal strain $\underline{\underline{\epsilon}}^{th}$ for an isotropic material is given by integration of the relation:

$$d\underline{\underline{\epsilon}}^{th} = \alpha(T) dT \underline{\underline{I}} \tag{2.3}$$

where α is the dilatation coefficient. The variation of the thermal strain with the temperature may be decomposed into two domains [32]:

$$\underline{\underline{\epsilon}}^{th} = \int_{T_i}^{T_f} \alpha(T) \mathrm{d}T \quad \begin{cases} \propto \int_{T_i}^{T_f} \mathrm{d}T \propto T & \text{for high temperature} \\ \propto \int_{T_i}^{T_f} T^3 \mathrm{d}T \propto T^4 & \text{for low temperature} \end{cases}$$

where $\propto$ denotes the proportionality symbol.

- For temperatures above 120 K, the thermal strain is linearly related to the temparature. The dilatation coefficient α is nearly constant: $\alpha \simeq 1.4.10^{-5}\,\mathrm{K}^{-1}$.
- For temperatures below 70 K, the coefficient of the term T^4 is low, thus the variation of the thermal strain is neglected.

The main portion of the thermal contraction is also due to the cool-down between the room temperature and about 70K.

2.2.3 Qualification of the material

Chemical analysis was carried out [33] in order to check the element content with respect to the specification. The inclusion content was determined with respect to the norm ASTM E45 [34].
The material was tested before forming by a formability test, called the Erichsen test. It was carried out on the metal sheet to assure the formability during the hydroforming process. The description of the test is given in Annex A.
A numerical simulation of the test, using a simplified model, has been used to estimate the material parameters, that assure the correct formability of the sheet. The initial material was tested after the rolling and the solution annealing. It did not present a sufficient ductility (a macrocrack was observed for a cupping of ∼6.6 mm instead of 7.2 mm as required by the manufacturer). The material parameters after cold-working are given in the table 2.3.

$\sigma_{0.2}$ [MPa]	$\sigma_{ultimate}$ [MPa]	A %
450	680	47

Table 2.3: Material properties after the rolling process (initial properties)

A heat treatment has been applied to modify the material parameters, namely the elongation at rupture and the yield point. Simulation shows that the elongation at break has to be at least 55% to make sure the hydroforming process will be successful. A serie of heat treatments has been done [35] to analyse the trends with respect to the main parameters: temperature T_{ht} and time, t_{ht} at the temperature T_{ht}. Samples, issued from different manufacturing procedures, have been heat treated at CERN and then subjected to the Erichsen test on the premises of the manufacturer. Three available materials have been elaborated with the following features [35, 36]:

- Material M1: Cold Rolling + Pre-heat treatment (900 °C) + Annealing (1000 °C) + Final Heat Treatment (1050 °C) + Skin Pass. The Erichsen test results, before additional heat treatment, are the following: 6.6 mm outside welded zone, 4.3 mm in the welded zone.

- Material M2: Cold Rolling + Pre-heat treatment (900 °C) + Annealing (1000 °C)+ Final Heat Treatment (1050 °C) + Skin Pass + Heat Treatment (1050 °C). The Erichsen test results, before additional heat treatment, are the following: 6.5-6.8 mm outside welded zone, 6.6-6.8 mm in the welded zone.

- Material M3: Cold Rolling + Pre-heat treatment (900 °C) + Annealing (1000 °C) + Final Heat Treatment (1090 °C)

The results of the Erichsen tests outside the welded zone, after heat treatment at temperature T_{ht} and during time t_{ht} at temperature T_{ht}, are the following (Table 2.4):

Material type	Temperature T_{ht}	Time t_{ht}	Punching depth
M1			6.6 mm
M1	1050 °C	15'	6.7-6.7 mm
M1	1090 °C	15'	6.5-6.7 mm
M1	1140 °C	15'	6.8-6.8 mm
M1	1140 °C	30'	7-7 mm
M2			6.6-6.8 mm
M2	1050 °C	15'	6.7-6.7 mm
M2	1090 °C	15'	6.9-7 mm
M2	1140 °C	15'	6.7-7 mm
M2	1140 °C	30'	7-7 mm
M3			7.2 mm
M3	1090°C	15'	7.2 mm
M3	1090°C	30'	7.2 mm

Table 2.4: Results of the Erichsen tests after heat treatment

Given the small number of tests (and dispersion), the study is more qualitative. As expected, a heat treatment at high temperatures increases the ductility and thus the punching depth in the Erichsen test is higher. Concerning the time of the heat treatment, two aspects have to be considered. On one hand, it seems that a long treatment increases the ductility, but on the other hand it induces a grain growth leading to unacceptable grain size. Moreover, the manufacturing feature has to be taken into account. The oven allows low duration of heat treatment (about 30 secondes). This time is sufficiently small to avoid the grain growth. But in order to keep the smallest grain size, the pre-heating temperature has been reduced. Final manufacturing process is the following:
Cold Rolling + Pre-heat treatment (700 °C) + Annealing (900 °C) + Final Heat Treatment (1100 °C).
This material has a good ductility (sufficient to form the bellows expansion joints).

The Erichsen test are quite repetitive and an average value of 7.05 mm is reached. It presents a small grain size (ASTM number: 10, average grain size: 11.2 μm) [36, 37], that ensures a good fatigue life.

2.3 Design of the interconnection bellows

2.3.1 Technological aspects

Metallic bellows expansion joints can be manufactured by three processes mainly:

- Welded plate bellows (also known as edge welded or diaphragm bellows).
  First, two discs are stamped to obtain diaphragm (classically, two different forming tools can be used: metal-to-metal or metal-to-rubber). The thickness of diaphragm is almost constant along the profile. Several different diaphragm shapes are used in metal bellows suitable for various applications (constant spring rate, more structural strength, behaviour under pressure, ...). After stamping, 2 diaphragms are welded together at the inside diameter to form a single convolution. The convolutions are stacked together (theorically unlimited) and welded at the outside diameter to create the bellows (Fig. 2.4). Different welding techniques can be applied: gas tungsten arc weld, electron beam weld, laser weld, plasma arc weld,...

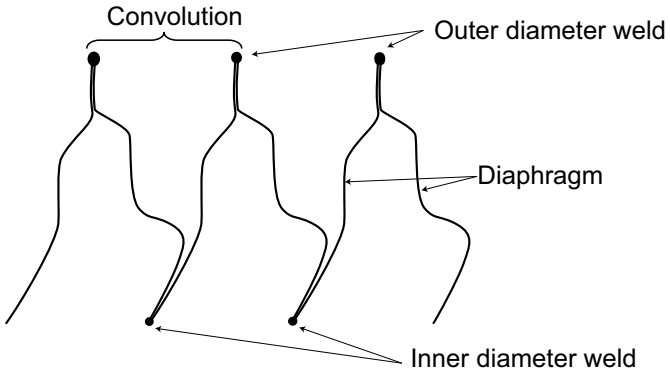

Figure 2.4: Bellows of the welded type

During manufacturing procedure, there is no displacement or elongation of metal. Thus, inner or outer diamater of convolutions are not restricted, which allows for a long stroke.

- Rolled formed bellows (mechanical forming)
  The manufacture is based on the forming of a tube, having a length equal to the contour of the finished unit. This is a roll forming operation in which one convolution at a time is created with tooling that forms the desired profil. Usually, a wide shallow convolution is formed and then is deepened by successive rolling operations. The metal is thinned as the convolutions become deeper.

- Hydraulic forming
  As mechanical forming procedure, hydroforming is based on forming of a tube. Hydraulic pressure expands the tube outwards into a set of longitudinally collapsing dies which form all the convolutions at one time. Shape of convolutions depends on the tooling profil. After forming, bellows may be annealed, but it is not considered beneficial. In radial outward forming, a small thinning occurs but this is compensated by an increase in yield strength due to cold work. When the bellows are subsequently annealed, the increase in yield is eliminated. Increased yield results in the increase of convolution deformation pressure and critical buckling pressure. Also, plastic strain due to deflection is reduced and it improves generally the fatigue life of expansion joint.

The choice of the bellows manufacturing procedure depends on application and volume of the production. Welded bellows are well-adapted for large stroke and small differential pressure. Due to weld, this procedure is not recommended for high pressure, ultra high vacuum (outgassing of the weld) or cryogenic temperatures (possible presence of brittle ferritic phase in the weld). Formed bellows contains only longitudinal weld. Hydraulic forming is generally used for high volume productions and/or for bellows which require uniformity (assurance quality).

Formed bellows expansion joints are categorized according to convolution shape, including, semi-toroidal, toroidal, S-shaped, U-shaped and nested (Fig. 2.5).

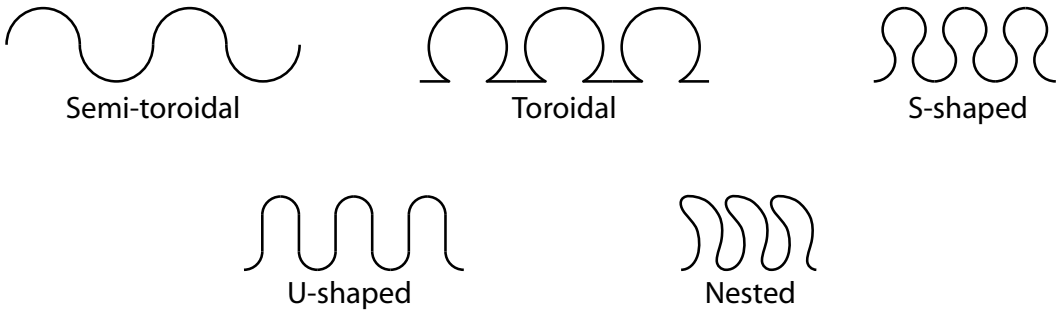

Figure 2.5: Bellows convolution shape

U-shaped bellows represents the most common type of bellows. Special very compact

thin-walled expansion joints, called nested bellows, are used for applications with high axial stroke. It has usually a sufficiently high curvature radius at root and at crest in order to allow for a fatigue life above 10^3 under vacuum conditions.
In many applications, bellows can have several plies. They are called multi-ply bellows. It allows to have high pressure capacity while keeping a good fatigue life. For a multi-ply structure, compared with the same total thickness of a single ply structure, the fatigue life increases due to a smaller thickness of a single ply.
Several technologies have been retained for the LHC interconnection bellows: single, multi-ply, U-shaped, nested bellows. All are obtained by using the hydraulic forming process. Details of the manufacturing procedure is given Fig. 2.6.

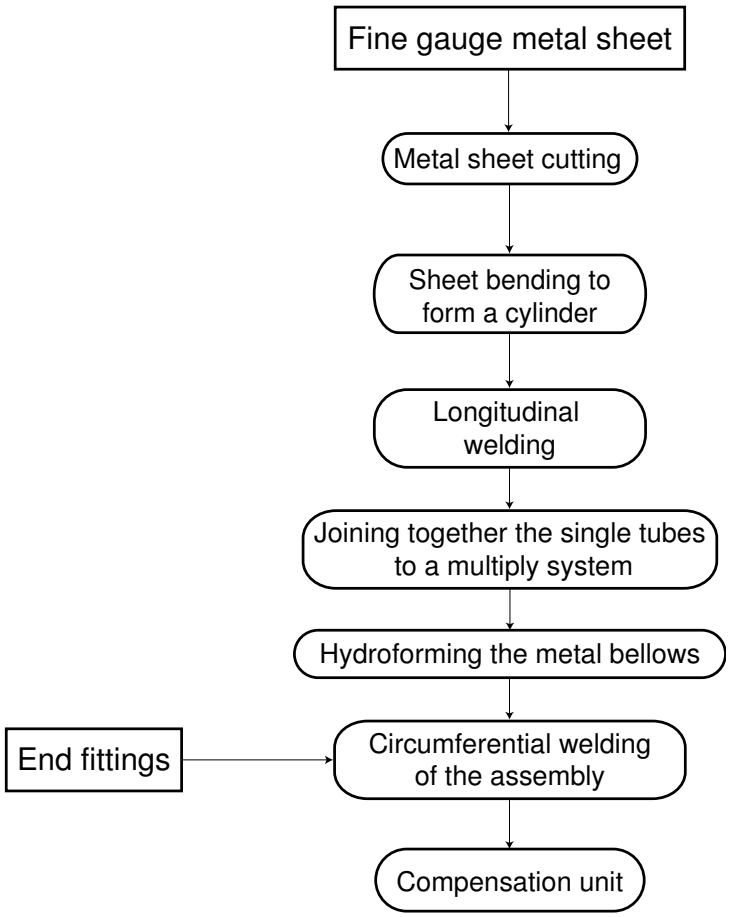

Figure 2.6: Manufacturing process for a hydroformed bellows

2.3.2 Structural response and main parameters

Two types of bellows expansion joints are used in the interconnections: standard U-type bellows (single or multi-ply bellows and universal joints) and nested bellows. The theoretical geometry of a U-type bellows is shown in Fig. 2.7. After the hydroforming process, a decrease of the initial thickness of the ply is measured, mainly at root and crest of the convolution; where a decrease of about $15 - 25\%$ is observed (cf. [38]).

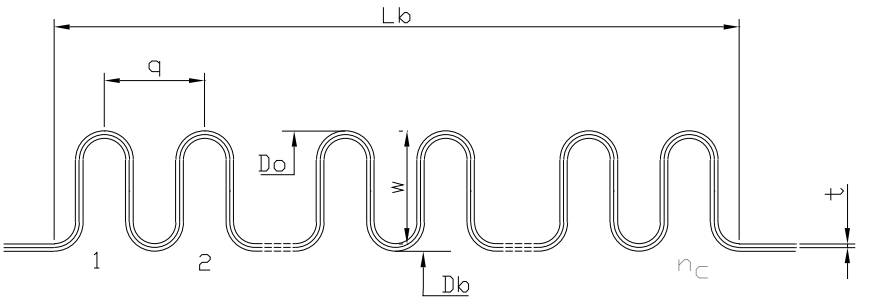

Figure 2.7: U-type bellows geometry

A local approach to the reliability oriented optimum design has been carried out in order to define the parameters of the expansion joints (cf. Skoczen [3]). The main parameters to determine are the following:

- Inside and outside diameters, D_b, D_o, respectively
- Free length, L_b
- Number of convolutions, n_c
- Number of plies, n_p
- Thickness of plies, t

Basic design conditions are the following: geometric constrains (diameters, length, ...), medium, pressure, temperature and motion. Generally, parameters of bellows are obtained from a compromise between fatigue life and stability: deflections result in meridional and circumferential stresses; in order to avoid premature fatigue failure, stresses must be kept as low as possible. Reducing bending stress resulting from a given deflection is easily achieved by reducing the thickness of bending part (that

means thickness of convolutions). However, in order to withstand the pressure, the convolution must have a thickness large enough so that the pressure induced membrane stresses are less than the allowable stress for the material at the design temperature.
The optimum design of bellows falls beyond the framework of the EJMA Standard (cf. [8]) . EJMA provides the formulas for stresses and for stability as well as fatigue evaluation. The EJMA approach is fully deterministic. The main objective of the optimisation (cf. [39]) is to reduce the bellows stiffness as much as possible since the bellows provide a mechanical decoupling between the neighbouring objects (cryomagnets). Usually the available space constitutes one of the serious limitations (constraints) for every expansion joint. Thus, one searches for minimum axial and transverse stiffness under the geometrical, stress, stability and fatigue constraints. The optimisation problem consists in the minimisation of the objective function, the axial stiffness, which is given by:

$$F_{ax} = \frac{\mu}{C_f}\Big(E_T\ D_m\Big(\frac{t_p}{w}\Big)^3\Big(\frac{n_p}{n_c}\Big)\Big) \tag{2.4}$$

where E_T denotes the modulus of elasticity at the temperature T, D_m stands for the bellows mean diameter ($D_m = D_b + w + n_p * t$) with D_b the inside diameter of bellows convolutions, t_p is the corrected bellows material thickness for one ply ($t_p = t\sqrt{\frac{D_b}{D_m}}$), w is the convolution depth, $\frac{n_p}{n_c}$ is the number of plies to number of convolutions ratio and μ, C_f are correction factors. The optimum parameters for the different LHC U-type bellows are the following (Table 2.5):

Type of bellows	Parameters of U-type bellows					
	n_p	n_c	q [mm]	D_b [mm]	w [mm]	t [mm]
RF Contact	1	15	5.2	82	8	0.15
QBX	2	16	4.5	54.4	8.9	0.3
M1, M2, M3	3	10	9.1	80	9.3	0.4
E	3	11	5.9	80	10	0.35

Table 2.5: Parameters of the U-type bellows

The convolution shape of the nested bellows is given in Fig. 2.8. The initial thickness of the wall of bellows is 0.15 mm. Minimum curvature radius is at root and equal to 6 mm.
The bellows are subjected to the following conditions [40]:
The outer pressure for every bellows corresponds to the insulation vacuum and is 10^{-6} mbar. The negative axial displacement corresponds to a compression of the bellows, obtained during the installation. The nested bellows for the MB-MB and MB-SSS interconnections have 14 convolutions whereas for the SSS-MB have 7 convolutions.

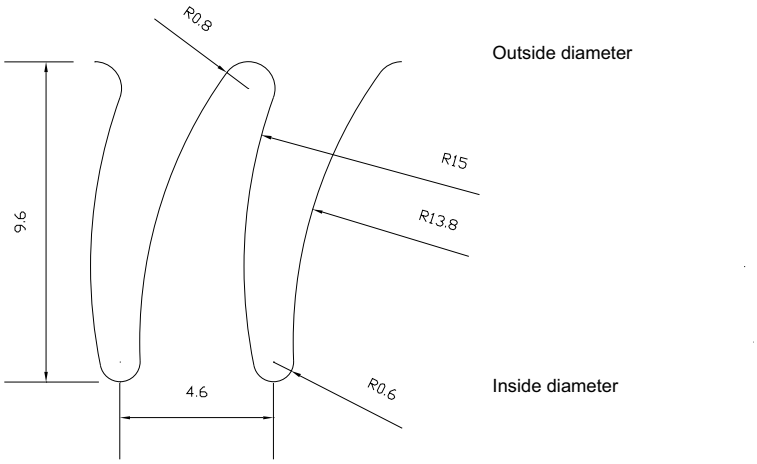

Figure 2.8: Shape of the convolutions of the nested bellows

Normal operating conditions (Table 2.6) and exceptional conditions (Table 2.7) are distinguished.

Type of bellows	Inner Pressure [bar]	Axial displacement [mm]		
		MB-MB	MB-SSS	SSS-MB
RF Contact	10^{-12}	-16/42.5	-16/35.5	-4/35.5
Nested bellows	10^{-12}	-30/32	-30/32	-11.5/13.5
M1, M2, M3	1.3	-16/30	-16/13	-16/20
QBX	0.016	-16/30	-16/13	-16/20
E	19.5	-10/55	-10/31	-10/41

Table 2.6: Normal operating conditions

2.4 Reliability of the expansion joints

The reliability of the LHC interconnections is determinated by the contribution of 3 systems: the mechanical compensation system, the electrical connections and the RF system. The thesis is dedicated to the analysis of the reliability of the mechanical compensation system comprising mainly the bellows expansion joints and the metal hoses. The expected global reliability of the mechanical compensation system is 99.8% [41]. Given the number of interconnections of LHC, the expected reliability of one interconnect is 99.9999% (Fig. 2.9). The apportionment of the reliability levels to the components within each reliability zone (Fig 2.10) is shown in Table 2.8.

Type of bellows	Inner Pressure [bar]	Axial displacement [mm]		
		MB-MB	MB-SSS	SSS-MB
RF Contact	10^{-12}	-16/45.5	-23/35.5	-4/35.5
Nested bellows	10^{-12}	-30/46	-30/46	-11.5/18
M1, M2, M3	12^a-20^b	-16/30	-16/13	-16/20
QBX	2^a	-16/30	-16/13	-16/20
E	19.5	-10/55	-10/31	-10/41

^{a}: Cooldown/Warmup
^{b}: Magnet quench

Table 2.7: Exceptional operating conditions

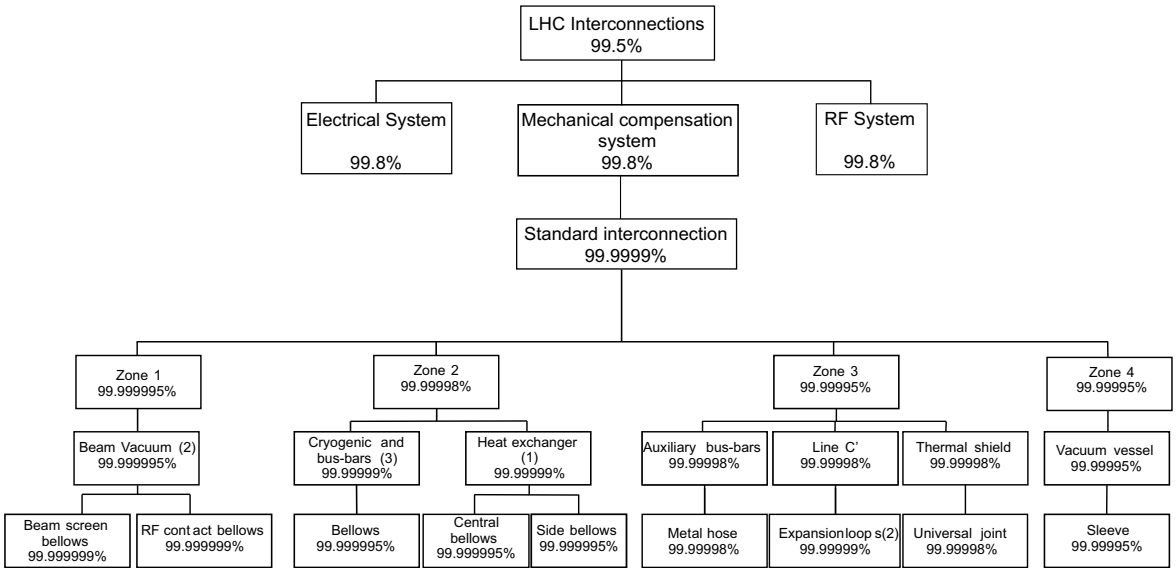

Figure 2.9: Reliability of the LHC interconnections - apportionment of expected reliability levels to sub-systems

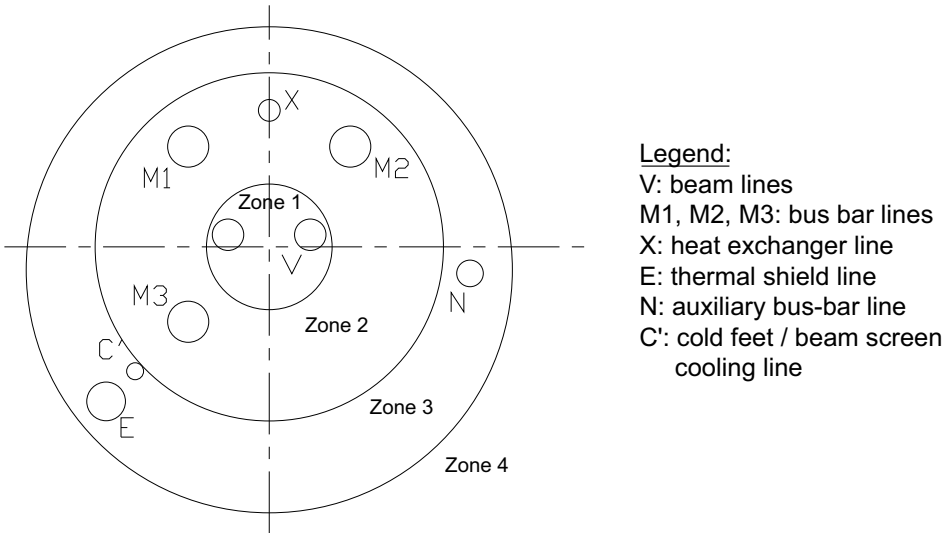

Figure 2.10: Reliability zones in the LHC interconnections

MB-MB standard interconnection - Availability 99.9999%		
Type of interconnect	Number of interconnects	Subsystems and components
Zone 1		
Beam vacuum V1 & V2 Reliability: 99.999995%	2	Beam screen bellows assembly Reliability 99.999999%
		RF contact bellows assembly Reliability 99.999999%
Zone 2		
Cryogenic and bus-bars M1 & M2 & M3 Reliability 99.99999%	3	Expansion joint assembly Reliability 99.999995%
Heat exchanger Reliability 99.99999%	1	Side bellows assembly Reliability 99.999995%
		Central bellows assembly Reliability 99.999995%
Zone 3		
Auxiliary bus-bars (line N) Reliability 99.99998%	1	Metal hose Reliability 99.99998%
Line C' Reliability 99.99998%	1	Expansion loops (2) Reliability 99.99999%
Thermal shield (line E) Reliability 99.99998%	1	Universal joint assembly Reliability 99.99998%
Zone 4		
Vacuum vessel sleeve Reliability 99.99995%	1	Sleeve assembly Reliability 99.99998%
		Seals (2) Reliability 99.99999%

Table 2.8: Expected reliability levels of the components of the mechanical compensation system

Chapter 3

Plastic strain induced martensitic transformation in stainless steels at cryogenic temperatures

Phase transformation occurs in austenitic stainless steels. General concept of thermodynamic and phase transformation is presented in [42] within the framework of solid state physics. Martensitic transformation is a displacive and diffusionless phenomenon with the creation of twins with particular orientations with respect to the initial austenitic lattice [43]. The present chapter is dedicated more to the mechanical behaviour and constitutive modeling than to physical and metallurgical aspects. A simplified model of martensitic transformation in stainless steels at cryogenic temperatures has been proposed in the papers [44–48]. The constitutive modeling of plastic flow under cryogenic conditions is based on the assumption of small strains (≤ 0.2) and the continuity of the plastic flow (no serrated yielding) [47]. The hardening law for the two-phase material (α' martensite platelets embedded in the austenite matrix) has been obtained from the Mori-Tanaka homogeneisation [47]. A mixed hardening with combined isotropic and kinematic contributions has been proposed. The constitutive model, containing a reasonable number of parameters, has been numerically implemented in CASTEM2000 and checked with respect to experimental data [11, 49].

3.1 Introduction

It is well known that the solutes like Ni, Mn and N considerably stabilise the γ-phase. For instance the strain induced martensitic content in the grades 304LN, 316LN at low temperatures is much lower than in the grades 304L, 316L for the same level of

plastic strain [11]. Nevertheless, even if no spontaneous martensitic transformation at low temperatures, martensite platelets can appear under plastic strain. The increase in martensite fraction promoted by plastic deformation can be detected by measuring the magnetic permeability μ. The evolution of μ at low temperature corresponding to monotonic straining as well as to the cyclic loads for 304L and 316L stainless steels was investigated by Suzuki et al., 1988 [10]. Tensile properties of stainless steels at low temperatures are strongly influenced by the plastic strain induced martensitic transformation. As a result of the transformation the initially homogenous α'-phase looses its homogeneity because of the inclusions of the harder martensite phase. The martensite platelets embedded in the soft austenite matrix provoke local stress concentration and block the movement of dislocations. Therefore the onset of the martensitic transformation leads to increase of the strain hardening. The curves showing the increase of α' martensite with strain for 304L and 304LN stainless steel at 77 K are reported by Morris et al., 1992. Similar studies for 304L and 316L stainless steels at 77 K and at 4 K were carried out by Suzuki et al., 1988 [10]. Transformation kinetics has been developed by Olson and Cohen, 1975 [50]. The authors attribute the strain-induced martensite nucleation sites to the shear-band intersections (the shear-bands being in the form of α' martensite, mechanical twins or stacking-fault bundles). The analysis leads to the following equation for the volume fraction of martensite versus plastic strain:

$$\xi_{\alpha'} = 1 - exp\left(-\beta\left(1 - exp\left(-\alpha\epsilon^{p}\right)\right)^{n}\right) \tag{3.1}$$

where α represents the rate of shear-band formation, β represents the probability that a shear-band intersection will become a martensite site and n is a fixed exponent. The transformation curves (volume fraction of martensite versus plastic strain) show a typical sigmoidal shape with saturation levels below 100 % (Fig. 3.1).

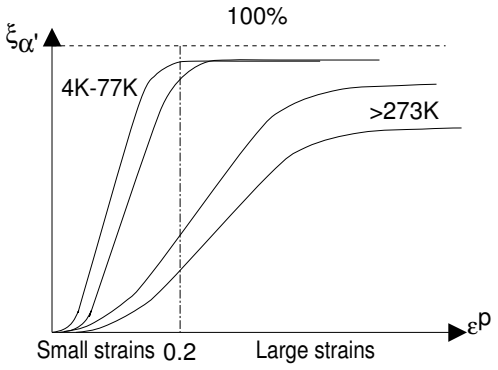

Figure 3.1: Volume fraction of martensite versus plastic strain at cryogenic temperatures

Constitutive modeling of steels exhibiting strain induced martensitic transformation

was initiated by Narutani, Olson and Cohen, 1982 [51]. The approach was based on the Voigt model with equal repartition of strains in both phases of the two-phase composite. A more complex constitutive model has been developed by Stringfellow, Parks and Olson, 1992 [52]. Here an isotropic hypoelastic formulation based on large strains was used. The inelastic streching was decomposed into two parts: slip in the austenite and martensite phases and the nucleation part resulting from the transformation process. Local and global stress and strain components were linked by using the Eshelby solutions for incompressible spherical inclusions in an infinite and incompressible isotropic matrix. The model was successfully validated on the Angel set of data [53]. Next complex constitutive modeling has been developed by Levitas, Idesman and Olson, [54]. The phase transformation model is based on the mesoscopic continuum thermodynamics. Generalisation of the Prandtl-Reuss equations with isotropic hardening to the case of large strains for elastic-plastic isotropic materials was used. The deformation gradient was decomposed into three parts: elastic, plastic and the transformation one. The elastic strains were assumed small when compared to the inelastic ones. A difference between the phase transformation under the displacement and the stress controlled boundary conditions was demontrated. Some further recent constitutive modeling of TRIP steels for the temperature above 77 K can be found in [55–58].
The above recalled constitutive modeling was based on the assumption of large inelastic strains. However, if the strain induced transformation occurs at very low temperatures (liquid nitrogen 77 K, liquid helium 4.5 K) then the steep part of the transformation curves (see Fig. 3.1) remains in the domain of relatively small strains (below 0.2). In such a case the constitutive modeling can be considerably simplified [47] and stays within the scope of the classical theories of plasticity. The relevant elastic-plastic model with linear mixed (isotropic/kinematic) hardening including the effect of strain induced martensitic transformation has been introduced in [47].

3.2 Transformation kinetics $(\gamma \rightarrow \alpha')$

Olson and Cohen [50] developed a one-dimensional model for the kinetics of martensitic transformation, called OC model. The evolution of the volume fraction of martensite as a function of plastic strain is derived by considering the course of shear band formation, the probability of shear-band intersections and the probability of an intersection generating a martensitic embryo. In this model, only temperature and plastic strain control the martensite evolution. Different improvements have been brought to this model, covering the influence of the stress state [52] and the strain rate [54]. However, a considerable number of parameters have to be identified for these models. In the present paper, a simplified model will be developed for the cryogenic applications. Generally, the volume fraction of martensite can be presented in the following form:

$$\xi = \xi\left(p,\ T,\ \underline{\underline{\dot{\epsilon}}}^{p},\ \underline{\underline{\sigma}}\right) \tag{3.2}$$

where the accumulated plastic strain, p is defined by:

$$p = \int_0^t \sqrt{\frac{2}{3}\underline{\underline{\dot{\epsilon}}}^p : \underline{\underline{\dot{\epsilon}}}^p} d\tau \tag{3.3}$$

with $\underline{\underline{\dot{\epsilon}}}^p$ the plastic strain rate and $\underline{\underline{\sigma}}$ the stress tensor. Under isothermal conditions, the classical sigmoidal curve has the following form (Fig. 3.2):

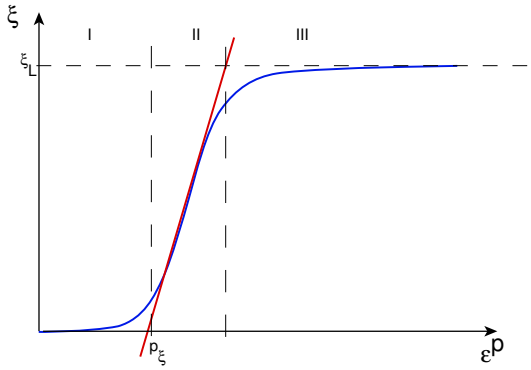

Figure 3.2: Volume fraction of martensite versus plastic strain

The curve may be decomposed into 3 phases:

- The phase I, which corresponds to a nonlinear increase of the martensitic content with the strain (primary phase)
- The phase II, where the volume percentage ξ is linearly related to plastic deformation ϵ^p [59] (secondary phase)
- The phase III, which corresponds to a saturation effect (tertiary phase)

A simplified law of evolution of the martensite content may be proposed for the phase II under the following form [45, 47]:

$$\dot{\xi} = A\left(T,\ \underline{\underline{\dot{\epsilon}}}^p,\ \underline{\underline{\sigma}}\right) \dot{p} H\left(\left(p - p_\xi\right)\left(\xi_L - \xi\right)\right) \tag{3.4}$$

where

- A is a function of the temperature, $\underline{\underline{\sigma}}$ the stress state and $\underline{\underline{\dot{\epsilon}}}^p$ the strain rate.
- p_ξ is the accumulated plastic strain threshold (to trigger the formation of martensite).
- ξ_L is martensite content limit, over which the martensitic transformation rate is considered equal to 0. Here, H represents the Heavyside function

Thus, the above shown 3 phases are simplified in the following way:

- Phase I: no martensitic transformation until p_ξ is reached.
- Phase II: the volume fraction of martensite (ξ) is linearly related to accumulated plastic strain (ϵ^p) until ξ_L is reached.
- Phase III: no martensitic transformation above ξ_L.

Stringfellow and al. [52] show that the stress state is taken into account by the triaxiality Σ, defined by the ratio between the hydrostatic stress and the equivalent stress.

$$\Sigma = \frac{1}{3}\frac{tr[\underline{\underline{\sigma}}]}{\sigma_{eq}} \tag{3.5}$$

with $\sigma_{eq} = \sqrt{\frac{3}{2}\underline{\underline{s}} : \underline{\underline{s}}}$, where $\underline{\underline{s}}$ is the deviatoric stress

$$\underline{\underline{s}} = \underline{\underline{\sigma}} - \frac{1}{3}tr[\underline{\underline{\sigma}}]\underline{\underline{I}} \tag{3.6}$$

and $\underline{\underline{I}}$ is the identity tensor.

3.3 Constitutive modelling of plastic flow at cryogenic temperatures

The present section aims at developing a mesoscopic modelling, capable to represent the hardening work and evolution of the martensite content for the material under different types of loads (monotonic or cyclic). The model is sufficiently simple to be integrated into a finite element code, without major effort. The plasticity model is based on a phenomenological mesoscopic approach. Microscopic model (polycristalline model) is an alternative way to represent the plastic flow [60–62]. It defines the mesoscopic plastic strains from plastic strains of each grains by homogeneisation. The yield surface is obtained as the collection of local criteria on each slip system, obeying Schmid law. Such a model is defined by a lot of internal variables and thus is quite difficult to implemente in a FE code for structure analysis.
The constitutive model is based on a classical approach to the plastic flow, that means on the linear mixed hardening. Since the material (stainless steel), containing a limited amount of martensite, can be described as a ductile austenitic matrix (γ-phase) containing rigid inclusions (α'-phase), dispersed in the whole volume of the RVE (Representative Volume Element), it is obvious that the material retains its ductility also at cryogenic temperatures. As long as the plastic flow mechanism is based mainly on the motion of dislocations (no serrated yielding), the classical models can be applied.

3.3.1 Constitutive formulation

Generally, the modeling is based on the following assumptions [47]:

1. The rate of increase of the volume fraction of the martensitic phase, $\dot{\xi}$, is given by
$$\dot{\xi} = A\left(T,\ \underline{\underline{\dot{\epsilon}}}^{p},\ \underline{\underline{\sigma}}\right)\dot{p}H\left(\left(p - p_{\xi}\right)\left(\xi_L - \xi\right)\right) \tag{3.7}$$

2. Small strains are considered (linear additive rule). The total strain is given by:
$$\underline{\underline{\epsilon}} = \underline{\underline{\epsilon}}^{e} + \underline{\underline{\epsilon}}^{p} + \underline{\underline{\epsilon}}^{th} + \xi\underline{\underline{\epsilon}}^{bs} \tag{3.8}$$
where $\underline{\underline{\epsilon}}^{e}$ denotes the elastic strain, $\underline{\underline{\epsilon}}^{p}$ and $\underline{\underline{\epsilon}}^{th}$ stand for the plastic and the thermal strain tensors, respectively. $\underline{\underline{\epsilon}}^{bs}$ is the free deformation called bain strain. It can be expressed in terms of relative volume change Δv, due to the phase transformation, as
$$\underline{\underline{\epsilon}}^{bs} = \frac{1}{3}\Delta v\underline{\underline{I}} \tag{3.9}$$
with
$$\Delta v = \frac{v_m - v_a}{v_a} \tag{3.10}$$
where v_a and v_m represent the unstressed specific volumes occupied by the austenite and the martensite, respectively. The value of Δv is about 0.02-0.05, depending on the alloy composition.
The expression of the thermal strain is given as a function of the dilatation tensor of the two-phase material $\underline{\underline{\hat{\alpha}}}$, by the general formula:
$$\mathrm{d}\underline{\underline{\epsilon}}^{th} = \underline{\underline{\hat{\alpha}}}(T,\ \xi)\mathrm{d}T \tag{3.11}$$
Considering both phases isotropic and under the assumption of global isotropy of the material, the tensor $\underline{\underline{\hat{\alpha}}}$ can be reduced to:
$$\underline{\underline{\hat{\alpha}}} = \alpha^{h}\underline{\underline{I}} \tag{3.12}$$
with α^h the homogenized dilatation coefficient.

3. The constitutive law is given by:
$$\underline{\underline{\sigma}} = \underline{\underline{\underline{\underline{E}}}} : \left(\underline{\underline{\epsilon}} - \underline{\underline{\epsilon}}^{p} - \underline{\underline{\epsilon}}^{th} - \xi\underline{\underline{\epsilon}}^{bs}\right) \tag{3.13}$$
where $\underline{\underline{\sigma}}$ denotes the stress tensor. For isotropic material, the elastic stiffness tensor $\underline{\underline{\underline{\underline{E}}}}$ is given by:
$$\underline{\underline{\underline{\underline{E}}}} = 3k\underline{\underline{\underline{\underline{J}}}} + 2\mu\underline{\underline{\underline{\underline{K}}}} \tag{3.14}$$

with

$$\begin{cases} \underline{\underline{\underline{\underline{J}}}} = \frac{1}{3}\underline{\underline{I}} \otimes \underline{\underline{I}} & (J_{ijkl} = \frac{1}{3}\delta_{ij}\delta_{kl}) \\ \underline{\underline{\underline{\underline{K}}}} = \underline{\underline{\underline{\underline{I}}}} - \underline{\underline{\underline{\underline{J}}}} & \text{and} \quad I_{ijkl} = \frac{1}{2}\left(\delta_{ik}\delta_{jl} + \delta_{il}\delta_{jk}\right) \end{cases}$$

and where $\mu = \frac{E}{2(1+\nu)}$, $k = \frac{E}{3(1-2\nu)}$ denote the shear and the compressibility moduli, respectively. To simplify the equations, we assume that the elastic properties of the two-phase material are not modified by the martensitic transformation (the elastic properties of the martensite and the austenite are quite similar). Nevertheless, the elastic properties of the austenite + martensite structure, i.e. the elastic coefficients, could be obtained by homogenisation.

4. The yield surface is defined as:

$$f_c\left(\underline{\underline{\sigma}},\ \underline{\underline{X}},\ R\right) = J_2\left(\underline{\underline{\sigma}} - \underline{\underline{X}}\right) - \sigma_y - R \tag{3.15}$$

where:

$$J_2\left(\underline{\underline{\sigma}} - \underline{\underline{X}}\right) = \sqrt{\frac{3}{2}\left(\underline{\underline{s}} - \underline{\underline{X}}\right) : \left(\underline{\underline{s}} - \underline{\underline{X}}\right)} \tag{3.16}$$

is the second invariant of the stress tensor. $\underline{\underline{X}}$ is the back stress tensor and σ_y, R stand for the yield point and the isotropic hardening, respectively.

5. It is assumed that the material is standard generalized that is to say it obeys the normality rule with the yield function postulated as the potential of plasticity. The plastic flow rate is given by:

$$\mathrm{d}\underline{\underline{\epsilon}}^p = \frac{3}{2}\frac{\underline{\underline{s}} - \underline{\underline{X}}}{J_2\left(\underline{\underline{\sigma}} - \underline{\underline{X}}\right)}\mathrm{d}\lambda \tag{3.17}$$

where λ is the plastic multiplier.

6. The hardening variables R and $\underline{\underline{X}}$ are altered by the presence of the martensite and the corresponding evolution laws are postulated:

$$\mathrm{d}R = F(\xi)\mathrm{d}p \tag{3.18}$$

$$\mathrm{d}\underline{\underline{X}} = \mathrm{d}\underline{\underline{X}}_a + \mathrm{d}\underline{\underline{X}}_{a+m} = \frac{2}{3}C(\xi)\mathrm{d}\underline{\underline{\epsilon}}^p + G(\xi)\mathrm{d}\underline{\underline{\epsilon}}^p \tag{3.19}$$

Here, we assume that the back stress increment is the sum of a classical term wich corresponds to the behaviour of the austenitic phase $\mathrm{d}\underline{\underline{X}}_a$ and a new term related to the presence of martensite $\mathrm{d}\underline{\underline{X}}_{a+m}$.

3.3.2 Hardening law for the two-phase material

The BCC martensite is much harder than the FCC austenite. The martensite platelets do not have the same orientation as the initial lattice [43]. If the movement of the dislocations occurs (plastic flow) then the dislocations are mobile in the austenitic matrix and are supposed to be stopped by the martensite inclusions. Thus, an elastic-plastic matrix and elastic inclusions are the principal components that constitute the two-phase material model.
Several models have been developed for austenitic materials and in particular for 316, 316L austenitic stainless steels. Among them, certain constitutive models are dedicated to cyclic loadings. Based on a model with isotropic and kinematic non-linear hardening variables [63], improvements have been done to take into account the effects of nonproportional cyclic loading [64–67]. All these models have not been identified and used at cryogenic temperatures.
Here, a simple linear kinematic hardening law may be used to model the plastic behaviour of the pure austenite phase:

$$\mathrm{d}\underline{\underline{X}}_{a0} = \frac{2}{3} C_0 \mathrm{d}\underline{\underline{\epsilon}}^p \tag{3.20}$$

Here C_0 represents the hardening modulus for the austenitic phase without the presence of martensite. For the two-phase material, the hardening modulus C_0 is replaced by the modulus C. The coefficient C is higher than C_0, defined for the pure austenite, because of the interactions between the dislocations in the austenite and the martensite inclusions. Generally, a function $\varphi(\xi)$ is defined:

$$C = C_0 \varphi(\xi) \tag{3.21}$$

with $\varphi(0) = 1$ (Fig. 3.3).

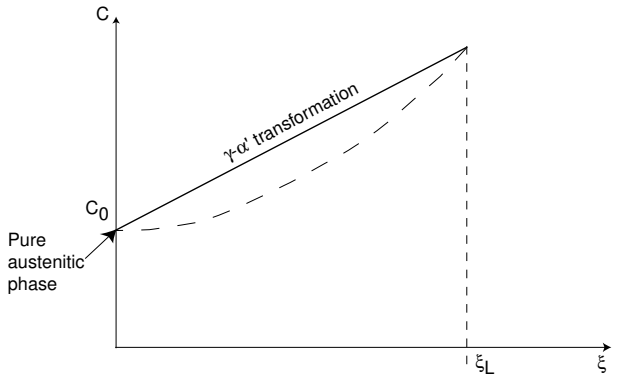

Figure 3.3: Evolution of the hardening modulus as a function of the martensite content

For the sake of simplicity, the function $\varphi(\xi)$ has been linearized and takes the form:

$$\varphi(\xi) = h\xi + 1 \tag{3.22}$$

where h is a parameter that depends on the material. The function $\varphi(\xi)$ represents the part of the hardening process that is related to the increase in volume fraction of martensitic inclusions and enhanced probability that a dislocation will be stopped by an inclusion. Here, the martensite platelets are regarded as hard small objects, embedded into γ phase, that act as the stoppers of motion of dislocations. Thus, the amount of plastic work corresponding to the same total strain considerably increases. The back stress increment can be subdivided into two components:

$$\mathrm{d}\underline{\underline{X}}_a = \mathrm{d}\underline{\underline{X}}_{a0} + \mathrm{d}\underline{\underline{X}}_{a\xi} = \frac{2}{3}C_0\mathrm{d}\underline{\underline{\epsilon}}^p + \frac{2}{3}C_0h\xi\mathrm{d}\underline{\underline{\epsilon}}^p \tag{3.23}$$

For the pure austenitic phase, a linearisation of the constitutive equations of plastic flow in the vicinity of the current state, leads to the following formula (provided that the process of plastic flow is active)

$$\Delta\underline{\underline{\sigma}}_a = \underline{\underline{\underline{\underline{E_t}}}} : \Delta\underline{\underline{\epsilon}} \tag{3.24}$$

where $\underline{\underline{\underline{\underline{E_t}}}}$ denotes the tangent tensor. If the same strain increment is applied to the austenite+martensite structure, the stress increment is obtained by homogenisation:

$$\Delta\underline{\underline{\sigma}}_{a+m} = \underline{\underline{\underline{\underline{E_H}}}} : \Delta\underline{\underline{\epsilon}} \tag{3.25}$$

The increment of hardening implied by the presence of the martensite is also given by:

$$\Delta\underline{\underline{\sigma}} = \Delta\underline{\underline{\sigma}}_{a+m} - \Delta\underline{\underline{\sigma}}_a = \left(\underline{\underline{\underline{\underline{E_H}}}} - \underline{\underline{\underline{\underline{E_t}}}}\right) : \Delta\underline{\underline{\epsilon}} \tag{3.26}$$

The homogenisation theory has been developed for elastic materials (matrix and inclusions) [68]. The matrix is considered isotropic. In the domain of plastic deformation (active processes) the linearization in the vicinity of the current state allows us to apply the homogenisation technique. Thus, over one load increment the matrix (γ phase) is represented by the corresponding tangent modulus:

$$\underline{\underline{\underline{\underline{E_{t_a}}}}} = 3k_{t_a}\underline{\underline{\underline{\underline{J}}}} + 2\mu_{t_a}\underline{\underline{\underline{\underline{K}}}} \tag{3.27}$$

where $\mu_{t_a} = \frac{E_t}{2(1+\nu)}$, $k_{t_a} = \frac{E_t}{3(1-2\nu)}$ and $E_t = \frac{EC}{E+C}$.
It is assumed that the inclusions are isotropic and elastic. The corresponding modulus of elasticity is given by:

$$\underline{\underline{\underline{\underline{E_m}}}} = 3k_m\underline{\underline{\underline{\underline{J}}}} + 2\mu_m\underline{\underline{\underline{\underline{K}}}} \tag{3.28}$$

where $\mu_m = \frac{E}{2(1+\nu)}$ and $k_m = \frac{E}{3(1-2\nu)}$.
Furthermore, the inclusions are supposed to be spherical and uniformly distributed in the austenite matrix. The Mori Tanaka's homogenisation (it is assumed that the interactions between inclusions are reduced to a homogeneous strain field in the inclusion) reads [68–70]:

$$\underline{\underline{\underline{\underline{E_H}}}} = \underline{\underline{\underline{\underline{E_{MT}}}}} = 3k_{MT}\underline{\underline{\underline{\underline{J}}}} + 2\mu_{MT}\underline{\underline{\underline{\underline{K}}}} \tag{3.29}$$

with $\underline{\underline{\underline{\underline{E_{MT}}}}}$ obtained from:

$$\left[\underline{\underline{\underline{\underline{E_{MT}}}}} + \underline{\underline{\underline{\underline{E^*}}}}\right]^{-1} = \sum_{i=a,m} f_i \left[\underline{\underline{\underline{\underline{E_i}}}} + \underline{\underline{\underline{\underline{E^*}}}}\right]^{-1} \tag{3.30}$$

where f_i denotes the volume fraction of the constituant "i" and $\underline{\underline{\underline{\underline{E^*}}}}$ stands for the Hill influence tensor.
Finally, the following equations are derived:

$$3k_{MT} + 3k^* = \left(\frac{1-\xi}{3(k_{t_a}+k^*)} + \frac{\xi}{3(k_1+k^*)}\right)^{-1} \tag{3.31}$$

$$2\mu_{MT} + 2\mu^* = \left(\frac{1-\xi}{2(\mu_{t_a}+\mu^*)} + \frac{\xi}{2(\mu_m+\mu^*)}\right)^{-1} \tag{3.32}$$

$$k^* = \frac{4}{3}\mu_{t_a} \text{ and } 2\mu^* = \frac{\mu_{t_a}(9k_{t_a}+8\mu_{t_a})}{3(k_{t_a}+2\mu_{t_a})}. \tag{3.33}$$

In what follows, it is assumed that the strain increment is mainly due to the plastic strains: $\Delta\underline{\underline{\epsilon}} \cong \Delta\underline{\underline{\epsilon}}^p$. Thus, the equation (3.26) becomes:

$$\Delta\underline{\underline{\sigma}} = \left(\underline{\underline{\underline{\underline{E_H}}}} - \underline{\underline{\underline{\underline{E_t}}}}\right) : \Delta\underline{\underline{\epsilon}}^p \tag{3.34}$$

As the plastic strains are represented by a deviatoric tensor (the trace is equal to 0) then: $\underline{\underline{\underline{\underline{J}}}} : \Delta\underline{\underline{\epsilon}}^p = \underline{\underline{0}}$ and $\underline{\underline{\underline{\underline{K}}}} : \Delta\underline{\underline{\epsilon}}^p = \Delta\underline{\underline{\epsilon}}^p$. Finally, the hardening due to the martensite formation becomes:

$$\Delta\underline{\underline{\sigma}} = 2(\mu_{MT} - \mu_{t_a})\Delta\underline{\underline{\epsilon}}^p \tag{3.35}$$

In order to obtain a sound response under the cyclic loads, the hardening has to be expressed in terms of the plastic variables: R, the isotropic hardening and $\underline{\underline{X}}$ the kinematic hardening.
If the pure kinematic hardening is considered, the increment of the back stress due to the martensite is obtained by:

$$\Delta\underline{\underline{X}}_{a+m} = \Delta\underline{\underline{\sigma}} \tag{3.36}$$

which leads to the equation:

$$\mathrm{d}\underline{\underline{X}}_{a+m} = 2(\mu_{MT} - \mu_{t_a})\mathrm{d}\underline{\underline{\epsilon}}^p \tag{3.37}$$

If the pure isotropic hardening is considered, the increment of the hardening parameter is obtained by the second invariant of the stress tensor:

$$\Delta R_{a+m} = \Delta R = J_2\left(\Delta\underline{\underline{\sigma}}\right) = 3(\mu_{MT} - \mu_{t_a})\Delta p \tag{3.38}$$

with $\Delta p = \sqrt{\frac{2}{3}\Delta\underline{\underline{\epsilon}}^p : \Delta\underline{\underline{\epsilon}}^p}$. So it leads to:

$$\mathrm{d}R = \mathrm{d}R_{a+m} = 3(\mu_{MT} - \mu_{t_a})\mathrm{d}p \tag{3.39}$$

This formulation is valid for a small martensite content (at the beginning of the strain induced transformation). Since the phase II at cryogenic temperatures corresponds approximately to $\epsilon^p \leq 0.2$ and goes to the saturation level of the martensite content a more general formulation of isotropic hardening has to be applied. The generalization leads to the following model:

$$\dot{R} = (R_\infty(\xi) - R)\dot{p} \tag{3.40}$$

This approach is compatible with the model of isotropic hardening with a saturation level R_∞ included, as proposed by Chaboche [71]. The linearisation of the equation (3.40) in the vicinity of the initial state leads back to the equation (3.39). The apportionment between the kinematic and isotropic hardening is made thanks to the parameter β defined by $0 \leq \beta \leq 1$.
Therefore, for mixed hardening, the following model has been postulated:

$$\dot{\underline{\underline{X}}} = 2b(\xi)\beta(\mu_{MT} - \mu_{t_a})\dot{\underline{\underline{\epsilon}}}^p \tag{3.41}$$

$$\dot{R} = b(\xi)(1-\beta)(R_\infty(\xi) - R)\dot{p} \tag{3.42}$$

Or in the expanded form:

$$\dot{\underline{\underline{X}}} = 2\beta(1-\xi)(\mu_{MT} - \mu_{t_a})\dot{\underline{\underline{\epsilon}}}^p \tag{3.43}$$

$$\dot{R} = (1-\xi)(1-\beta)(3(\mu_{MT} - \mu_{t_a}) - R)\dot{p} \tag{3.44}$$

Here, the term $b(\xi)$ is added in order to compensate for the strong assumption that the martensite inclusions are elastic. It tends to 0 for high content of martensite. In reality, the martensite inclusions shall rather be considered elastic-plastic. Therefore their contribution to the hardening of the two-phase material is slightly smaller. Also, it is assumed that when $\xi = 1$ (γ phase entirely replaced by the α' phase) the process of hardening linked to the phase transformation is terminated. For the sake of simplicity the relevant function $b(\xi)$ decribing these effects has been linerized.

The experimental curves, obtained under kinematically controlled cycling [10,72], show that, for symmetric strain loading, the compression stresses are higher than the tensile one's. This indicates a strong Bauschinger effect that can be described in terms of the parameter introduced by Życzkowski in 1981 [73]. The parameter β is related to the stress level at unloading (σ') and the stress level associated with the reverse active process (σ'^{-}), see Fig. 3.4.

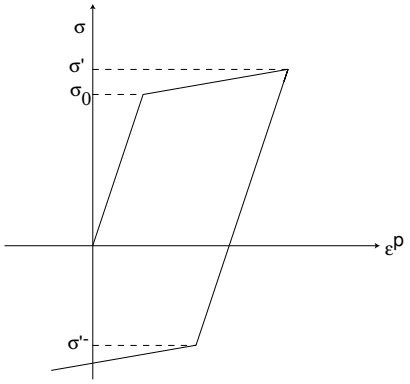

Figure 3.4: Illustration of the unloading and the reverse loading processes

It is defined by the following formula:

$$\beta = \frac{\sigma' + \sigma'^{-}}{2(\sigma' - \sigma_0)} \tag{3.45}$$

It varies between 0 for the isotropic hardening (no Bauschinger effect) and 1 for the kinematic hardening (perfect Bauschinger effect). Thus, it allows to describe the ratio between the isotropic and the kinematic hardening. The parameter has to be identified on experimental basis.

3.3.3 Final set of the constitutive equations

The final set of the constitutive equations resumes to [47]:

- Kinetics of martensitic tranformation

$$\dot{\xi} = A(T,\ \underline{\underline{\dot{\epsilon}}}^p,\ \underline{\underline{\sigma}})\dot{p}H((p - p_\xi)(\xi_L - \xi))$$

- The constitutive law:

$$\underline{\underline{\sigma}} = \underline{\underline{\underline{\underline{E}}}} : \left(\underline{\underline{\epsilon}} - \underline{\underline{\epsilon}}^p - \underline{\underline{\epsilon}}^{th} - \xi\underline{\underline{\epsilon}}^{bs}\right)$$

with

$$\begin{cases} \underline{\underline{\epsilon}}^{bs} = \frac{1}{3}\Delta v \underline{\underline{I}} \\ \underline{\underline{\epsilon}}^{th} = \int \underline{\underline{\hat{\alpha}}} \mathrm{d}T \end{cases}$$

- Yield surface is defined by:

$$f_c\left(\underline{\underline{\sigma}},\ \underline{\underline{X}},\ R\right) = J_2\left(\underline{\underline{\sigma}} - \underline{\underline{X}}\right) - \sigma_y - R$$

with

$$\begin{cases} J_2\left(\underline{\underline{\sigma}} - \underline{\underline{X}}\right) = \sqrt{\frac{3}{2}\left(\underline{\underline{s}} - \underline{\underline{X}}\right) : \left(\underline{\underline{s}} - \underline{\underline{X}}\right)} \\ \underline{\underline{s}} = \underline{\underline{\sigma}} - \frac{1}{3}Tr\left(\underline{\underline{\sigma}}\right)\underline{\underline{I}} \end{cases}$$

- The normality rule:

$$\mathrm{d}\underline{\underline{\epsilon}}^p = \frac{\partial f_c}{\partial \underline{\underline{\sigma}}}\mathrm{d}\lambda = \frac{3}{2}\frac{\underline{\underline{s}} - \underline{\underline{X}}}{J_2\left(\underline{\underline{\sigma}} - \underline{\underline{X}}\right)}\mathrm{d}\lambda$$

- The hardening laws:

$$\begin{cases} \dot{\underline{\underline{X}}} = \frac{2}{3}(C + 3\beta(1-\xi)(\mu_{MT} - \mu_{t_a}))\dot{\underline{\underline{\epsilon}}}^p \\ \dot{R} = (1-\xi)(1-\beta)(3(\mu_{MT} - \mu_{t_a}) - R)\dot{p} \end{cases}$$

with

$$C = C_0(1 + h\xi)$$

3.4 Implementation of the constitutive model

3.4.1 Numerical versus experimental results

The model has been implemented in the code CASTEM2000. The method of the "return mapping" is used to integrate the constitutive equations for an active plastic process [74]. The return mapping algorithm is based on the elastic plastic split, by first integrating the elastic equations to obtain an elastic predictor, which is used as the initial condition for the plastic return. The numerical algorithm can be illustrated in the following way:

- Current state variables: $\underline{\underline{\sigma}}_n$, $\underline{\underline{\epsilon}}^p_n$, $\underline{\underline{X}}_n$, R_n, ξ_n, p_n
- Elastic predictor defined from a total strain increment:
  $\underline{\underline{\sigma}}^0_{n+1}$, $\underline{\underline{\epsilon}}^{p^0}_{n+1} = \underline{\underline{\epsilon}}^p_n$, $\underline{\underline{X}}^0_{n+1} = \underline{\underline{X}}_n$, $R^0_{n+1} = R_n$, $\xi^0_{n+1} = \xi_n$, $p^0_{n+1} = p_n$.
- Test if the new state is elastic or not.
- If not ($f^0_{c_{n+1}} > 0$), the increment Δp and $\Delta\underline{\underline{\epsilon}}^p$ are computed.
- The increment $\Delta\xi = A\Delta p$ is calculated.
- The state variables (q) are updated from the evolution law. ($q^{i+1}_{n+1} = q^i_{n+1} + \Delta q$)

- The condition $\xi_{n+1}^{i+1} \leq \xi_L$ is checked. If $\xi_{n+1}^{i+1} > \xi_L$, no further accumulation of martensite takes place.
- The iterative process stops for $f_{c_{n+1}}^{i+1} \leq 0$.

Details of the numerical procedure are explained in the Section 5.2.
As the initial verification [47], the model has been checked with respect to the experimental results obtained on the 304L samples tested at 77K [11], under tensile monotonic loading (Fig. 3.5).

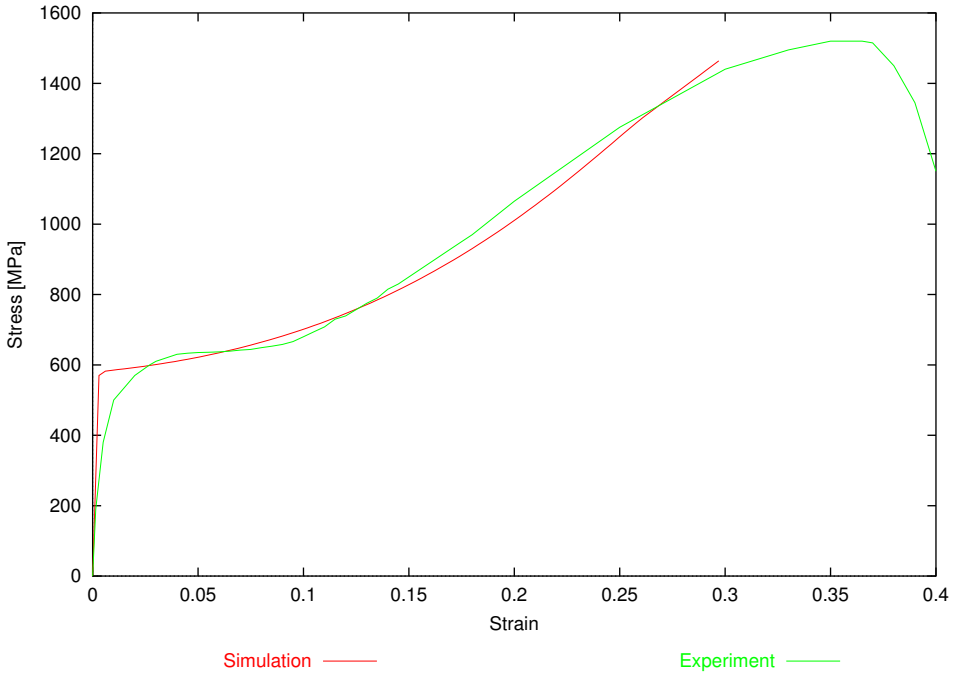

Figure 3.5: Tensile test for the grade 304L stainless steel at 77 K

The simulation is terminated just after having reached the strain level 0.2 which corresponds approximately to the martensite content saturation level (end of phase II). Figure 3.6 shows that the model is equally applicable to the cyclic loads, even if the full set of experimental data allowing determination of the material parameters is not yet available. It is roughly compatible with the results presented by Tomita [58].

The results were obtained from the following set of data (Table 3.1).
As the second verification, the model has been checked with respect to the experimental data of Iwamoto and al. [49]. Figure 3.7 shows the comparison between the numerical and experimental results for monotonic loading of SUS304 samples, tested at 128 K. Here, inelastic strain corresponds to the plastic strain ϵ^p and the bain strain

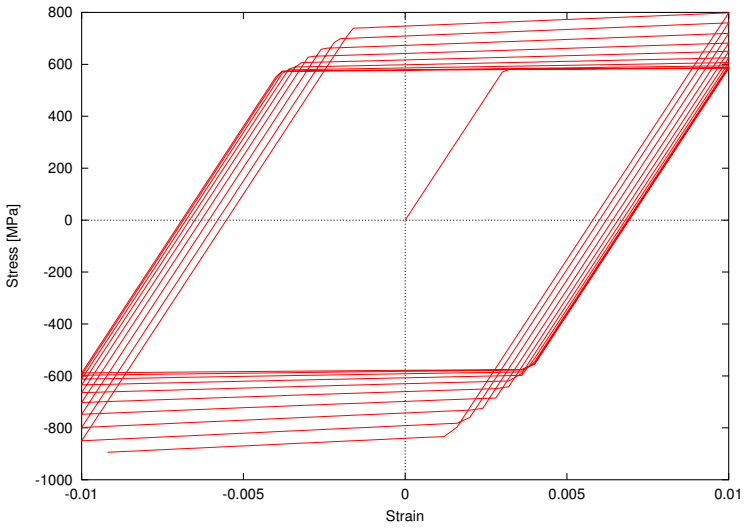

Figure 3.6: Hysteresis loops under cycling loading

E [GPa]	ν	σ_y [MPa]	C_0 [MPa]	h	A	p_ξ	ξ_L	β^a	Δv
190	0.3	580	750	1.9	4.23	0.004	0.9	0.45	0.05

[a]: Obtained from the Suzuki's data [10]

Table 3.1: Set of data for the 304L at 77 K.

$\xi\epsilon^{bs}$.
The difference of behavior in compression with respect to the tensile test is due to the bain strain which is associated with the $\gamma - \alpha'$ phase transformation. The martensite, having a compacity less than the austenite, induces a decrease of stress in tension and an increase in compression.
The results were obtained from the following set of data (Table 3.2).

E [GPa]	ν	σ_y [MPa]	C_0 [MPa]	h	β^a	Δv	ξ_L	p_ξ		A	
								T[b]	C[b]	T[b]	C[b]
190	0.3	600	1200	1.8	0.45	0.05	0.97	0.028	0.005	6.3	6.3

[a]: Obtained from the Suzuki's data [10]
[b]: T stands for tension and C stands for compression

Table 3.2: Set of data for the 304 at 128 K

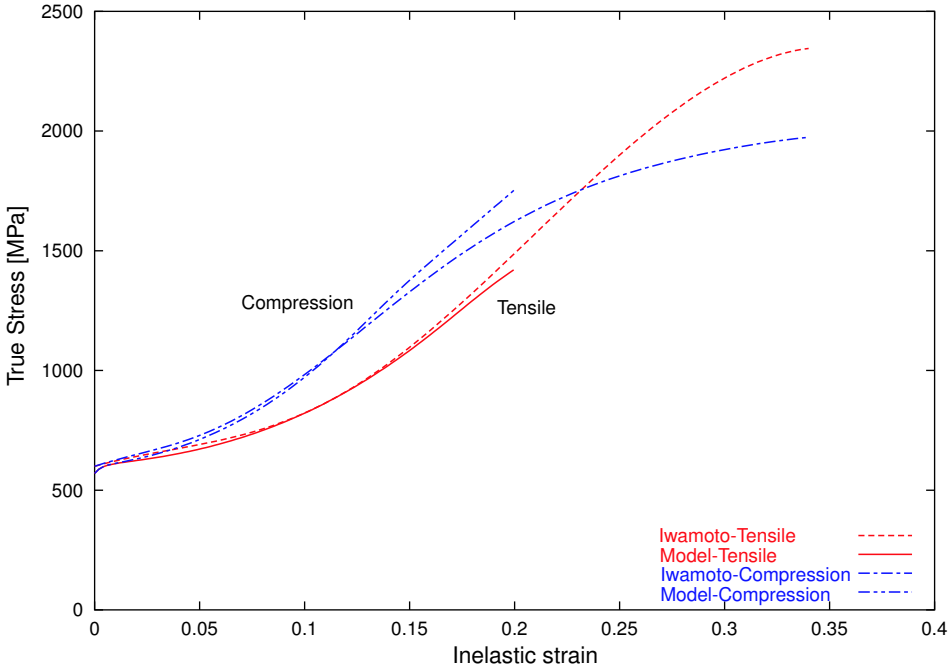

Figure 3.7: True stress as a function of the inelastic strain for grade 304 stainless steel at 128 K

3.4.2 Identification and interpretation of the hardening parameters

The particularity of the model is the definition of the hardening variables versus the martensite content. For the material parameters given in Table 3.3, the evolution of the hardening variables are shown in Figs. 3.8 and 3.9.

E [GPa]	ν	C_0 [MPa]	h	A
190	0.3	750	1.9	4.23

Table 3.3: Set of data for the 304L stainless steel

The term $T1(\xi)$ denotes the kinematic hardening variable, corresponding to the hardening of the γ austenitic phase due to the presence of martensitic phase. It reads:

$$T1(\xi) = \frac{2}{3} C_0 (1 + h\xi) \tag{3.46}$$

The term $T2(\xi)$ denotes the second kinematic hardening variable, corresponding to the

hardening due to the two-phase material. It reads:

$$T2(\xi) = 2\beta(1-\xi)(\mu_{MT}(\xi) - \mu_{t_a}(\xi)) \tag{3.47}$$

The term $T3(\xi)$ denotes the isotropic hardening modulus due to the two-phase material. $T3(\xi)$ is defined by:

$$\dot{R} = T3(\xi)\dot{p} \tag{3.48}$$

It reads:

$$T3(\xi) = (1-\xi)(1-\beta)(3(\mu_{MT}(\xi) - \mu_{t_a}(\xi)) - R(\xi)) \tag{3.49}$$

As demonstrated in Fig. 3.8, the hardening variables due to two-phase material in-

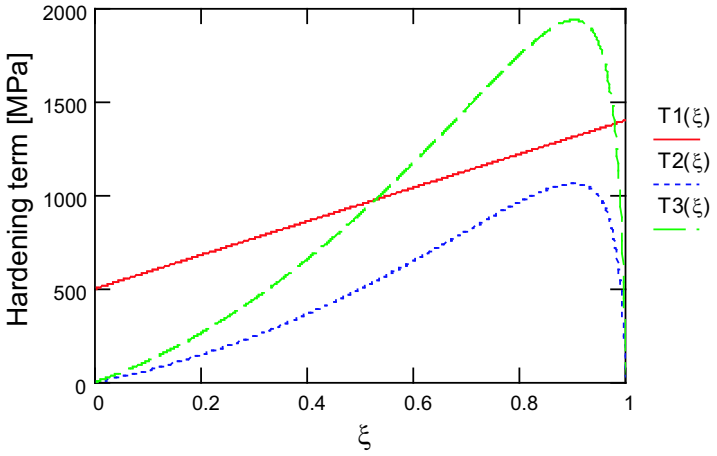

Figure 3.8: Evolution of the different hardening variables (moduli)

crease slightly for small martensite content and considerably for high volume fraction of martensite. The term $T1$ and $T3$ reach 0 for $\xi = 1$, that corresponds to a complete $\gamma - \alpha'$ transformation. The hardening modulus of the γ austenite increases linearly with the martensite content until it reaches the hardening modulus of martensite for $\xi = 1$.
Fig. 3.9 shows the isotropic and the kinematic hardening modulae as a function of the martensite content. $T4(\xi)$ is defined by:

$$\underline{\underline{\dot{X}}} = T4(\xi)\underline{\underline{\dot{\epsilon}}}^p \tag{3.50}$$

and it satisfies:

$$T4(\xi) = T1(\xi) + T2(\xi) \tag{3.51}$$

The hardening moduli vary in the same way with the volume fraction of martensite. The amount of kinematic hardening is larger than the isotropic one.

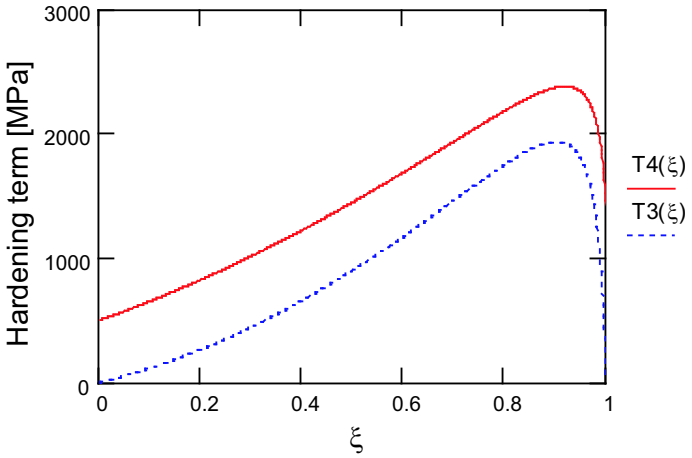

Figure 3.9: Evolution of the kinematic and the isotropic hardening variables

Chapter 4

Evolution of damage in the presence of inclusions

4.1 Introduction

The damage phenomena are associated with the decrease of the material properties, due to the nucleation and growth of microvoids and microcracks. Physically, the creation of these material imperfections may be due to severals processes:

- The creep damage due to the viscoplastic deformation leading to intergranular decohesions
- The high cycle fatigue damage where locally the microplasticity occurs
- The damage induced by the radiation which is due to the displacements of atoms
- The fragile damage due to cleavage
- The ductile damage for which large plastic strains induce dislocation stacking and then microfault

The theory of the continuum damage mechanics is based on the assumption of the difference of scale between the micro-damage (microcracks and microvoids) and the Representative Volume Element (RVE). The damage analysis gives criteria for the creation of mesocracks, then another theory has to be used to describe the phenomena: the fracture mechanics. It is important to use a unique formulation to describe the different damage processes [75]. It is based on the assumption that damage is driven by plastic strains, elastic strain energy and by an instability process. In the LHC interconnection system, the expansion joints are subjected to high deformations, that lead to the low cycle fatigue. The conditions of low temperatures and low strain rates

allow to neglect creep damage (associated with the viscoplasticity). The damage due to the radiation is neglected as fragile damage (no observation of cleavage, even in the martensitic phase [76, 77]). Several phenomena occur in the material used for the LHC expansion joints: the phase transformations, the ductile damage of the austenite phase and the ductile damage of the martensite phase. Both the martensite platelets and the microcrack fields develop simultaneously and co-exist in the same material volume (Fig. 4.1).

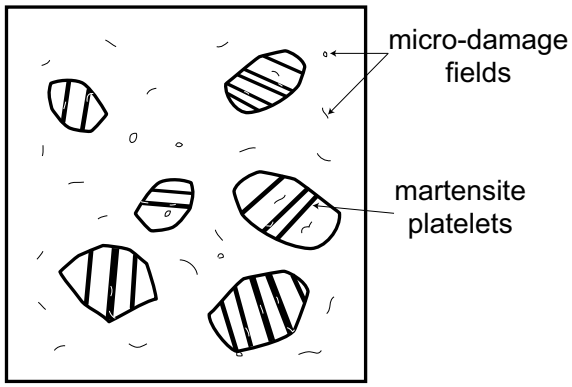

Figure 4.1: Plastic strain induced phase transformation and micro-damage fields

The influence of the phase transformation on the damage evolution is not obvious. Does the martensite, which can be defined as a hard phase, stop the growth of microcracks in the austenite or does the martensite enhance the nucleation of material imperfections due to the concentration of strains in the vicinity of the inclusions?
In order to describe damage evolution, three approaches are developed:

- the first one corresponds to a general formulation for which the material may be considered homogeneous (no difference between the martensite and the austenite is made). This approach can be developed because the damage is considered ductile for both phases.

- the second one aims at defining orthotropic damage to take into account the principal directions of thin-walled corrugated shell. The model is an extension of the isotropic ductile damage (Lemaitre, [78]). It is sufficiently simple to be applicable at cryogenic temperatures.

- the third one consists in defining the damage evolution in both phases, taking into account the difference of the material properties. Thanks to the mixing law, the mesoscopic damage variable can be defined.

4.2 General formulation

4.2.1 Reminder of the isotropic damage theory

The damage variable, as introduced by Kachanov [79], was defined on the basis of the irreversible processes leading to nucleation and growth of microvoids and microcracks in the entire volume of the sample. All types of voids and cracks (inter- and transgranular) that spoil the integrity of the material are accounted for. Damage variable is represented here by a scalar, defined as a surface intensity of intersections of microvoids and microcracks in the RVE (eq. 4.1 and Fig. 4.2).

$$D = \frac{S_D}{S} \tag{4.1}$$

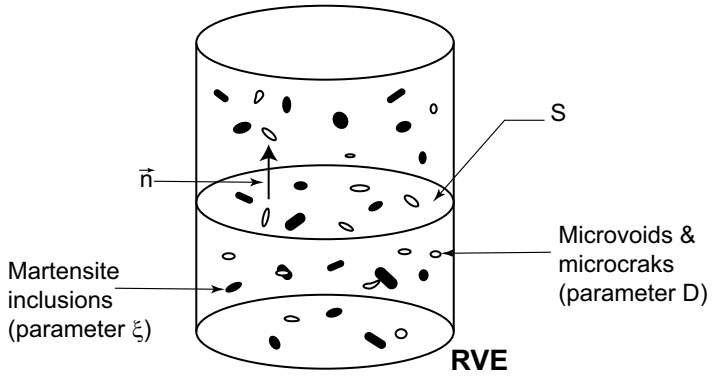

Figure 4.2: The Representative Volume Element (RVE): definition of the parameters D and ξ

In case of isotropic damage, the local value of D does not depend on the orientation of the plane of the section. By definition the damage variable satisfies the condition:

$$0 \leq D \leq 1 \tag{4.2}$$

$D = 0$ stands for a non-damaged material whereas $D = 1$ stands for a total decohesion of the sample. On the basis of the above-defined parameter, the so-called effective stress has been introduced by Rabotnov [80]. It is defined by:

$$\underline{\underline{\tilde{\sigma}}} = \frac{\underline{\underline{\sigma}}}{1 - D} \tag{4.3}$$

Lemaitre proposed the equivalence principle in terms of strains [78]. This leads to the definition of the damage as the loss of the elastic stiffness [81].

The damage has been defined on the basis of the irreversible thermodynamic process [82, 83]. It is assumed that the state potential is assimilated with the Helmholtz free energy and that for a damageable elastic-plastic material it can be be expressed as (cf. [78]):

$$\Psi = \Psi\left(\underline{\underline{\epsilon}}^e,\ T, r,\ \underline{\underline{\alpha}},\ D\right) = \Psi\left(\underline{\underline{\epsilon}} - \underline{\underline{\epsilon}}^p - \underline{\underline{\epsilon}}^{th},\ T, r,\ \underline{\underline{\alpha}},\ D\right) \tag{4.4}$$

or in the developed form:

$$\Psi = \frac{1}{\rho}\left(\frac{1}{2}(1-D)\underline{\underline{\underline{\underline{E}}}} : \underline{\underline{\epsilon}}^e : \underline{\underline{\epsilon}}^e + \frac{1}{3}H\underline{\underline{\alpha}} : \underline{\underline{\alpha}}\right) + \Psi_r \tag{4.5}$$

where H is the kinematic hardening modulus, $\underline{\underline{\alpha}}$ is the back strain and ψ_r stands for the part of the Helmholtz potential associated with the isotropic hardening. Based on the Helmholtz state potential, the constitutive law for the damageable material is given by:

$$\underline{\underline{\sigma}} = \rho\frac{\partial\Psi}{\partial\underline{\underline{\epsilon}}^e} = (1-D)\underline{\underline{\underline{\underline{E}}}} : \underline{\underline{\epsilon}}^e \tag{4.6}$$

The variable associated to the damage is the scalar:

$$Y = -\rho\frac{\partial\Psi}{\partial D} = \frac{1}{2}\underline{\underline{\underline{\underline{E}}}} : \underline{\underline{\epsilon}}^e : \underline{\underline{\epsilon}}^e \tag{4.7}$$

This scalar can be expressed [83, 84]:

$$Y = \frac{1}{2}\frac{\mathrm{d}w_e}{\mathrm{d}D}\bigg|_{\sigma,T} \tag{4.8}$$

which corresponds to the half of the variation of the elastic energy generated by a variation of damage at constant stress and temperature. This term is also called the strain energy density release rate. In case of isotropic material, it can be expressed as a function of the Von Mises equivalent stress and the triaxility rate (defined as the ratio of the hydrostatic stress and the Von Mises stress) [78, 85]:

$$Y = \frac{\sigma_{eq}^2}{2E(1-D)}\left(\frac{2}{3}(1+\nu) + 3(1-2\nu)\left(\frac{\sigma_h}{\sigma_{eq}}\right)^2\right) \tag{4.9}$$

The hydrostatic stress σ_h is given by:

$$\sigma_h = \frac{1}{3}Tr[\underline{\underline{\sigma}}] \tag{4.10}$$

The potential of dissipation F_d leads to the evolution law:

$$\dot{D} = \frac{\partial F_d}{\partial Y}\dot{\lambda} \tag{4.11}$$

It is a continuous convex scalar function of the dual variables. The potential can be postulated as (cf. [48, 78]):

$$F_d = \frac{S}{(s+1)(1-D)} \left(\frac{Y}{S}\right)^{s+1} \tag{4.12}$$

Such a formulation yields the following kinetic law of damage evolution (cf. [78, 86]):

$$\dot{D} = \left(\frac{Y}{S}\right)^{s} \dot{p} H(p - p_D) \tag{4.13}$$

where p_D is the so-called damage threshold and H denotes the Heaviside function.

4.2.2 Plastic strain induced phase transformation and isotropic damage model

The constitutive laws, presented in Section 3, were modified to take into account the evolution of damage, in the following way [48]:

- Kinetics of martensitic tranformation

$$\dot{\xi} = A(T,\ \underline{\underline{\dot{\epsilon}}}^p,\ \underline{\underline{\sigma}}) \dot{p} H((p - p_\xi)(\xi_L - \xi)) \tag{4.14}$$

- The constitutive law:

$$\underline{\underline{\tilde{\sigma}}} = \underline{\underline{\underline{\underline{E}}}} : \left(\underline{\underline{\epsilon}} - \underline{\underline{\epsilon}}^p - \underline{\underline{\epsilon}}^{th} - \xi \underline{\underline{\epsilon}}^{bs}\right) \tag{4.15}$$

  with

$$\underline{\underline{\tilde{\sigma}}} = \frac{\underline{\underline{\sigma}}}{1-D} \tag{4.16}$$

  where $\underline{\underline{\epsilon}}^{bs}$ is the distortional field associated with the phase transformation.

- Yield surface is defined by:

$$f_c\left(\underline{\underline{\tilde{\sigma}}},\ \underline{\underline{\underline{X}}},\ R\right) = J_2\left(\underline{\underline{\tilde{\sigma}}} - \underline{\underline{\underline{X}}}\right) - \sigma_y - R \tag{4.17}$$

  with

$$\begin{cases} J_2\left(\underline{\underline{\tilde{\sigma}}} - \underline{\underline{\underline{X}}}\right) = \sqrt{\frac{3}{2}\left(\underline{\underline{\tilde{s}}} - \underline{\underline{\underline{X}}}\right) : \left(\underline{\underline{\tilde{s}}} - \underline{\underline{\underline{X}}}\right)} \\ \underline{\underline{\tilde{s}}} = \underline{\underline{\tilde{\sigma}}} - \frac{1}{3} Tr\left(\underline{\underline{\tilde{\sigma}}}\right) \underline{\underline{I}} \end{cases} \tag{4.18}$$

- The normality rule:

$$\mathrm{d}\underline{\underline{\epsilon}}^p = \frac{\partial f_c}{\partial \underline{\underline{\sigma}}} \mathrm{d}\lambda = \frac{3}{2} \frac{\underline{\underline{\tilde{s}}} - \underline{\underline{\underline{X}}}}{J_2\left(\underline{\underline{\tilde{\sigma}}} - \underline{\underline{\underline{X}}}\right)} \frac{\mathrm{d}\lambda}{1-D} \tag{4.19}$$

  with

$$\mathrm{d}\lambda = (1-D)\mathrm{d}p \tag{4.20}$$

- The hardening laws:

$$\begin{cases} \dot{\underline{\underline{X}}} = \frac{2}{3}H(\xi)\dot{\underline{\underline{\alpha}}} = \frac{2}{3}H(\xi)\dot{\underline{\underline{\epsilon}}}^p(1-D) \\ \dot{R} = b(\xi)(R_\infty(\xi)-R)\dot{p}(1-D) = b(\xi)(R_\infty(\xi)-R)\dot{r} \end{cases} \tag{4.21}$$

  with

$$\begin{cases} H(\xi) = C + 3\beta(1-\xi)(\mu_{MT}-\mu_{t_a}) \\ b(\xi) = (1-\xi)(1-\beta) \\ R_\infty(\xi) = 3(\mu_{MT}-\mu_{t_a}) \\ C = C_0(1+h\xi) \end{cases} \tag{4.22}$$

- Modified Helmholtz free energy to account for the phase transformation:

$$\Psi == \Psi\left(\underline{\underline{\epsilon}} - \underline{\underline{\epsilon}}^p - \underline{\underline{\epsilon}}^{PT} - \underline{\underline{\epsilon}}^{th},\ T, r,\ \underline{\underline{\alpha}},\ D\right) \tag{4.23}$$

  Here, the assumption is made that both the density ρ and the elastic stiffness tensor $\underline{\underline{\underline{\underline{E}}}}$ depend weakly on the volume fraction of martensite ξ and the equation (4.5) can be adopted.

$$\Psi = \frac{1}{\rho}\left(\frac{1}{2}(1-D)\underline{\underline{\underline{\underline{E}}}} : \underline{\underline{\epsilon}}^e : \underline{\underline{\epsilon}}^e + \frac{1}{3}H\underline{\underline{\alpha}} : \underline{\underline{\alpha}}\right) + \Psi_r \tag{4.24}$$

- Damage evolution law:

$$\dot{D} = \left(\frac{Y}{S}\right)^s \dot{p}H(p-p_D) \tag{4.25}$$

  where Y is the damage coupled thermodynamic force.

It is worth pointing out that damage evolution and phase transformation are not coupled in the present model.

4.3 Orthotropic ductile damage

4.3.1 Second order damage tensor

For thin-walled shells, three principal directions can easily be defined: normal to the shell and two in-plane orthogonal directions. Thus, it is justified to propose a damage tensor in the form [87]:

$$\underline{\underline{D}} = \sum_{i=1,3} D_i \vec{n}_i \otimes \vec{n}_i \tag{4.26}$$

where $\vec{n}_i$ stands for the principal direction i and D_i denotes the damage parameter related to the direction i. It is defined by:

$$D_i = \frac{S_{D_{\vec{n}_i}}}{S_{\vec{n}_i}} \tag{4.27}$$

where $S_{D_{\vec{n}_i}}$ is the damage area in the section $S_{\vec{n}_i}$, represented by the normal $\vec{n}_i$.

4.3.2 The effective stress

The effective stress $\underline{\underline{\tilde{\sigma}}}$ is supposed to obey the strain equivalence principle:

$$\underline{\underline{\tilde{\sigma}}} = \underline{\underline{\underline{\underline{E}}}} : \underline{\underline{\epsilon}}^e \tag{4.28}$$

The relation between the stress and the effective stress tensors is based on the Murakami formulation [88] and is postulated under the form:

$$\underline{\underline{\sigma}} = \frac{1}{2}\left(\left(\underline{\underline{I}} - \underline{\underline{D}}\right)\underline{\underline{\tilde{\sigma}}} + \underline{\underline{\tilde{\sigma}}}\left(\underline{\underline{I}} - \underline{\underline{D}}\right)\right) \tag{4.29}$$

with $\underline{\underline{I}}$ the identity tensor. The general relationship between the stress and the effective stress tensors reads [89]:

$$\underline{\underline{\tilde{\sigma}}} = \underline{\underline{\underline{\underline{M}}}}^{-1} : \underline{\underline{\sigma}} \tag{4.30}$$

or

$$\underline{\underline{\sigma}} = \underline{\underline{\underline{\underline{M}}}} : \underline{\underline{\tilde{\sigma}}} \tag{4.31}$$

where $\underline{\underline{\underline{\underline{M}}}}$ stands for the symmetric damage effect tensor, that depends on the damage state and fulfils the conditions:

$$M_{ijkl} = M_{jikl} = M_{klij} \tag{4.32}$$

In its general form (linked to the eqn. 4.29), the damage effect tensor reads:

$$\begin{aligned}\underline{\underline{\underline{\underline{M}}}} &= \frac{1}{4}\left[\left(\underline{\underline{I}} - \underline{\underline{D}}\right)\underline{\otimes}\,\underline{\underline{I}} + \left(\underline{\underline{I}} - \underline{\underline{D}}\right)\bar{\otimes}\,\underline{\underline{I}} + \underline{\underline{I}}\,\underline{\otimes}\left(\underline{\underline{I}} - \underline{\underline{D}}\right) + \underline{\underline{I}}\,\bar{\otimes}\left(\underline{\underline{I}} - \underline{\underline{D}}\right)\right] \\ &= \frac{1}{2}\underline{\underline{\underline{\underline{I}}}} - \frac{1}{4}\left[\underline{\underline{D}}\,\underline{\otimes}\,\underline{\underline{I}} + \underline{\underline{D}}\,\bar{\otimes}\,\underline{\underline{I}} + \underline{\underline{I}}\,\underline{\otimes}\,\underline{\underline{D}} + \underline{\underline{I}}\,\bar{\otimes}\,\underline{\underline{D}}\right]\end{aligned} \tag{4.33}$$

or in the direct notation:

$$M_{ijkl} = \frac{1}{2}(\delta_{ik}\delta_{jl} + \delta_{il}\delta_{jk}) - \frac{1}{4}(D_{ik}\delta_{jl} + D_{il}\delta_{jk} + \delta_{ik}D_{jl} + \delta_{il}D_{jk}) \tag{4.34}$$

Here, $\otimes$, $\underline{\otimes}$ and $\bar{\otimes}$ are defined by:

$$\begin{cases} \underline{\underline{\underline{\underline{C}}}} = \underline{\underline{A}} \otimes \underline{\underline{B}} \Longleftrightarrow \underline{\underline{\underline{\underline{C}}}}|_{ijkl} = \underline{\underline{A}}|_{ij} \otimes \underline{\underline{B}}|_{kl} = A_{ij}B_{kl} \\ \underline{\underline{\underline{\underline{C}}}} = \underline{\underline{A}}\underline{\otimes}\underline{\underline{B}} \Longleftrightarrow \underline{\underline{\underline{\underline{C}}}}|_{ijkl} = \underline{\underline{A}}|_{ij}\underline{\otimes}\underline{\underline{B}}|_{kl} = A_{ik}B_{jl} \\ \underline{\underline{\underline{\underline{C}}}} = \underline{\underline{A}}\bar{\otimes}\underline{\underline{B}} \Longleftrightarrow \underline{\underline{\underline{\underline{C}}}}|_{ijkl} = \underline{\underline{A}}|_{ij}\bar{\otimes}\underline{\underline{B}}|_{kl} = A_{il}B_{jk} \end{cases}$$

Hence, the Helmholtz free energy state potential for linear elasticity coupled with damage is written in the following form:

$$\Psi = \frac{1}{\rho}\left(\frac{1}{2}\underline{\underline{\epsilon}}^e : \underline{\underline{\underline{\underline{M}}}} : \underline{\underline{\underline{\underline{E}}}} : \underline{\underline{\epsilon}}^e\right) + \Psi_p \tag{4.35}$$

where Ψ_p is the plastic part, which in principle does not depend upon $\underline{\underline{D}}$.

4.3.3 Kinetic law of damage evolution

The driving force of ductile damage evolution is the accumulated plastic strain. In the case of anisotropic ductile damage the damage parameter D is replaced by the damage tensor $\underline{\underline{D}}$ and the strain energy density release rate Y is replaced by the relevant tensor $\underline{\underline{Y}}$ (cf. [78]). Again both $\underline{\underline{D}}$ and $\underline{\underline{Y}}$ form a pair of dual state variables. In the present chapter, it is assumed that the driving force of evolution of anisotropic ductile damage remains the accumulated plastic strain. The strength energy of damage is replaced by a tensor $\underline{\underline{C}}$, which defines the material properties in the principal directions of damage (cf. [90]). Furthermore, it is assumed that as soon as the damage threshold p_D is reached, damage starts developing driven by the increase in the accumulated plastic strain p. However, damage evolution is different along the principal directions described by the eigenvectors of tensor $\underline{\underline{D}}$. Thus, the kinetic law of damage evolution is postulated in the following form (cf. [90, 91]):

$$\dot{\underline{\underline{D}}} = \underline{\underline{C}}\ \underline{\underline{Y}}\ \underline{\underline{C}}^T \dot{p} H(p - p_D) \tag{4.36}$$

which assures that the damage tensor is symmetric. It is worth pointing out that the eq. 4.36 reduces to eq. 4.13 in the case of isotropic damage, with $s = 1$. Tensor $\underline{\underline{C}}$ is defined as follows:

$$\underline{\underline{C}} = \sum_{i=1,3} C_i \vec{n}_i \otimes \vec{n}_i \tag{4.37}$$

and can be classified as the tensor containing the material moduli. $\underline{\underline{C}}$ is symmetric and positiv defini.
The strain energy density release rate tensor is defined by:

$$\underline{\underline{Y}} = -\rho \frac{\partial \Psi}{\partial \underline{\underline{D}}} \tag{4.38}$$

Eqs. 4.33 and 4.35 lead to the following conclusion:

$$\underline{\underline{Y}} = \frac{1}{4} \left[\underline{\underline{\epsilon}}^e \left(\underline{\underline{\underline{\underline{E}}}} : \underline{\underline{\epsilon}}^e \right) + \left(\underline{\underline{\underline{\underline{E}}}} : \underline{\underline{\epsilon}}^e \right) \underline{\underline{\epsilon}}^e \right] \tag{4.39}$$

Thus, the evolution law (4.36) imposes the symmetry of the tensor $\underline{\underline{D}}$. The power dissipation due to damage, $\dot{W}^D$, is given by:

$$\dot{W}^D = \underline{\underline{Y}} : \dot{\underline{\underline{D}}} = \underline{\underline{Y}} : \underline{\underline{C}}\ \underline{\underline{Y}}\ \underline{\underline{C}}^T \dot{p}|_{p>p_D} \tag{4.40}$$

The sign of $\dot{W}^D$ is the same as:

$$\underline{\underline{Y}} : \underline{\underline{C}}\ \underline{\underline{Y}}\ \underline{\underline{C}}^T = tr[\underline{\underline{Y}}\ \underline{\underline{C}}\ \underline{\underline{Y}}\ \underline{\underline{C}}^T] = tr[\underline{\underline{C}}^T\ \underline{\underline{Y}}\ \underline{\underline{C}}\ \underline{\underline{Y}}] \tag{4.41}$$

Since $\underline{\underline{C}}$ is symmetric, one obtains:

$$tr[\underline{\underline{C}}^T \ \underline{\underline{Y}} \ \underline{\underline{C}} \ \underline{\underline{Y}}] = tr[\underline{\underline{A}} \ \underline{\underline{A}}] \tag{4.42}$$

with $\underline{\underline{A}} = \underline{\underline{C}} \ \underline{\underline{Y}}$. Finally, developing trace operator:

$$tr[\underline{\underline{A}} \ \underline{\underline{A}}] = \sum_{i=1,3} A_i^2 \tag{4.43}$$

where A_i are the eigenvalues of $\underline{\underline{A}}$, leads to the following result:

$$\underline{\underline{Y}} : \underline{\underline{\dot{D}}} \geq 0 \tag{4.44}$$

which corresponds to the second thermodynamic principle. The relevant potential of dissipation reads:

$$F_d = \frac{1}{2} \left(\underline{\underline{C}} \ \underline{\underline{Y}} \ \underline{\underline{C}}^T \right) : \underline{\underline{Y}} \sqrt{\frac{(\underline{\underline{\tilde{s}}} - \underline{\underline{X}}) : \underline{\underline{\underline{\underline{L}}}} : (\underline{\underline{\tilde{s}}} - \underline{\underline{X}})}{(\underline{\underline{\tilde{s}}} - \underline{\underline{X}}) : (\underline{\underline{\tilde{s}}} - \underline{\underline{X}})}} \tag{4.45}$$

where

$$\underline{\underline{\underline{\underline{L}}}} \left(\underline{\underline{D}} \right) = \underline{\underline{\underline{\underline{M}}}}^{-1} \left(\underline{\underline{D}} \right) : \underline{\underline{\underline{\underline{M}}}}^{-1} \left(\underline{\underline{D}} \right) \tag{4.46}$$

or in direct notation:

$$L_{ijkl} = M^{-1}_{ijmn} M^{-1}_{mnkl} \tag{4.47}$$

F_d is a quadratic function of the conjugate force $\underline{\underline{Y}}$ and satisfies the following equation:

$$\underline{\underline{\dot{D}}} = \dot{\lambda} \frac{\partial F_d}{\partial \underline{\underline{Y}}} \tag{4.48}$$

Thus, the kinetic law of damage evolution (eq. 4.36) can be derived directly from the eq. 4.48.
The model has been built as a direct extrapolation of the isotropic reference case (see Table 4.1). The isotropic conjugate damage variables, D and Y, can be obtained from the orthotropic state variables $\underline{\underline{D}}$ and $\underline{\underline{Y}}$ by the following operations:

$$Y = Tr[\underline{\underline{Y}}] \tag{4.49}$$

and, assuming that $\underline{\underline{C}} = C\underline{\underline{I}}$ for isotropic material, the first invariant of damage rate tensor reads:

$$\dot{D} = Tr[\underline{\underline{\dot{D}}}] = C^2 Y \dot{p} \tag{4.50}$$

which corresponds to the isotropic damage evolution law with $S = 1/C^2$.

Isotropic model	Orthotropic model
Helmholtz free energy	
$\Psi = \frac{1}{2\rho}\underline{\underline{\epsilon}}^e : \underline{\underline{\underline{\underline{E}}}}(1-D) : \underline{\underline{\epsilon}}^e + \Psi_p$	$\Psi = \frac{1}{2\rho}\underline{\underline{\epsilon}}^e : \underline{\underline{\underline{\underline{M}}}}(\underline{\underline{D}}) : \underline{\underline{\underline{\underline{E}}}} : \underline{\underline{\epsilon}}^e + \Psi_p$
Effective stress	
$\underline{\underline{\sigma}} = (1-D)\underline{\underline{\tilde{\sigma}}}$	$\begin{aligned} \underline{\underline{\sigma}} &= \frac{1}{2}\left(\left(\underline{\underline{1}} - \underline{\underline{D}}\right)\underline{\underline{\tilde{\sigma}}} + \underline{\underline{\tilde{\sigma}}}\left(\underline{\underline{1}} - \underline{\underline{D}}\right)\right) \\ \Leftrightarrow \quad \underline{\underline{\sigma}} &= \underline{\underline{\underline{\underline{M}}}}(\underline{\underline{D}}) : \underline{\underline{\tilde{\sigma}}} \end{aligned}$
Conjugate force associated to damage	
$Y = -\rho\frac{\partial \Psi}{\partial D} = \frac{1}{2}\underline{\underline{\epsilon}}^e : \underline{\underline{\underline{\underline{E}}}} : \underline{\underline{\epsilon}}^e$	$\begin{aligned} \underline{\underline{Y}} &= -\rho\frac{\partial \Psi}{\partial \underline{\underline{D}}} \\ &= \frac{1}{4}\left(\underline{\underline{\epsilon}}^e\left(\underline{\underline{\underline{\underline{E}}}} : \underline{\underline{\epsilon}}^e\right) + \left(\underline{\underline{\underline{\underline{E}}}} : \underline{\underline{\epsilon}}^e\right)\underline{\underline{\epsilon}}^e\right) \end{aligned}$
Potential of dissipation associated to irreversible damage process	
$F_d = \frac{1}{2}\frac{Y^2}{S}\frac{1}{1-D}$	$\begin{aligned} F_d &= \frac{1}{2}\left(\underline{\underline{C}}\ \underline{\underline{Y}}\ \underline{\underline{C}}^T\right) : \underline{\underline{Y}}\, a(\underline{\underline{D}}) \\ a(\underline{\underline{D}}) &= \left(\frac{\left(\underline{\underline{\tilde{s}}} - \underline{\underline{X}}\right) : \underline{\underline{\underline{\underline{M}}}}^{-1} : \underline{\underline{\underline{\underline{M}}}}^{-1} : \left(\underline{\underline{\tilde{s}}} - \underline{\underline{X}}\right)}{\left(\underline{\underline{\tilde{s}}} - \underline{\underline{X}}\right) : \left(\underline{\underline{\tilde{s}}} - \underline{\underline{X}}\right)}\right)^{\frac{1}{2}} \end{aligned}$
Kinetic law of damage evolution	
$\dot{D} = \dot{\lambda}\frac{\partial F_d}{\partial Y} = \frac{Y}{S}\dot{p}\Big\vert_{p>p_D}$	$\underline{\underline{\dot{D}}} = \dot{\lambda}\frac{\partial F_d}{\partial \underline{\underline{Y}}} = \left(\underline{\underline{C}}\ \underline{\underline{Y}}\ \underline{\underline{C}}^T\right)\dot{p}\Big\vert_{p>p_D}$

Table 4.1: Comparison between isotropic and orthotropic models

4.3.4 Principal directions of damage versus principal directions of stress

As an example of texture induced damage anisotropy, let us consider a material that is characterized by long grains oriented along longitudinal direction (1) and narrow in the transverse direction (2) (Fig. 4.3).

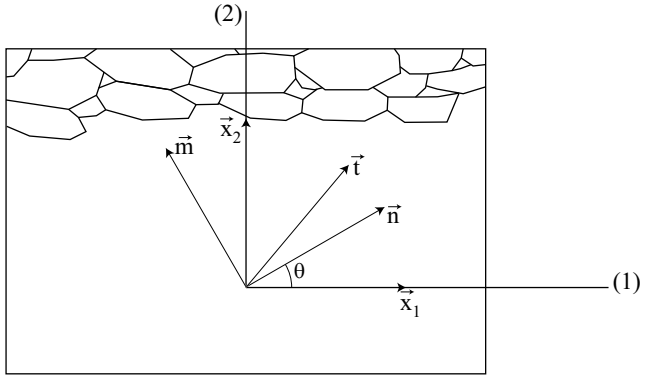

Figure 4.3: Principal base of material and uniaxial load

In order to simplify the analysis a two dimensional problem is considered. The tensor of material properties, expressed in the principal basis, reads (Fig. 4.3):

$$\underline{\underline{C}} = \begin{pmatrix} C_1 & 0 \\ 0 & C_2 \end{pmatrix}_{(\vec{x_1},\vec{x_2})} \tag{4.51}$$

Assume that the unixial load is applied in the direction $\vec{n}$, located at angle θ with respect to direction (1). Thus the stress tensor can be expressed by:

$$\underline{\underline{\sigma}} = \sigma \vec{n} \otimes \vec{n} \tag{4.52}$$

with $(\vec{n}, \vec{m})$ being the principal directions of stress. It is interesting now to trace the principal directions of damage rate $\underline{\underline{\dot{D}}}$ as a function of ratio between the components of tensor $\underline{\underline{C}}$: C_1/C_2. Since damage evolution may lead to redistribution of stress, it is assumed that the principal directions of $\underline{\underline{\dot{D}}}$ are searched at the moment when damage threshold is reached:

$$p = p_D$$

Thus, the following tensor will be brought to its principal directions:

$$\underline{\underline{V}}_D = \frac{\underline{\underline{\dot{D}}}}{\dot{p}}\Big|_{p=p_D} = \underline{\underline{C}}\ \underline{\underline{Y}}\ \underline{\underline{C}}^T \tag{4.53}$$

where $\underline{\underline{V}}_D$ is expressed by:

$$\underline{\underline{V}}_D = v_0 \vec{t} \otimes \vec{t} \tag{4.54}$$

Here, $\vec{t}$ denotes the principal direction of damage and $v_0\dot{p}$ stands for the initial ($p = p_D$) damage rate intensity. The principal direction of damage $\vec{t}$ has been illustrated in Fig. 4.4 for several C_1/C_2 ratios and as a function of angle θ.

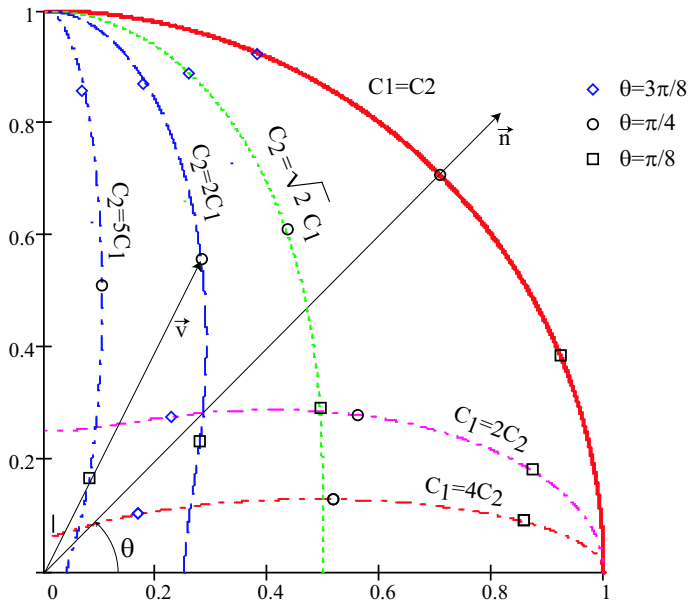

Figure 4.4: Evolution of initial normalized damage rate intensity vector $\vec{v}$ as a function of plastic strain at 4.2 K

Next, a normalized damage rate intensity vector $\vec{v}$ is introduced. Vector $\vec{v}$ is defined as follows (Fig. 4.4):

$$\vec{v} = \frac{v_0}{v_{0max}}\vec{t} \tag{4.55}$$

where v_{0max} is the maximum damage rate intensity, obtained always in the direction of highest C component ($\vec{x_1}$ if $C_1 > C_2$ and $\vec{x_2}$ if $C_2 > C_1$). It is worth pointing out that for $C_1 = C_2$ (isotropic case) $v_0 = v_{0max}$ and vector $\vec{v}$ has always length equal to 1. Also, the stress and damage rate principal directions are fully colinear. Finally, the illustration shows that the colinearity is obtained also in the case when vector $\vec{n}$ is parallel to directions (1) or (2), that means the load is applied in one of the principal texture directions. Such formulation of damage orthotropy is suitable not only for materials with strong texture but also for generalized composite materials, containing fibre orientation.

4.3.5 Complete set of equations for a two-phase material with orthotropic damage

The final set of the constitutive equations takes the following form (cf. [90, 91]):

- Kinetics of martensitic transformation ($\gamma \rightarrow \alpha'$):

$$\dot{\xi} = A(T, \underline{\underline{\sigma}})\dot{p}H((p - p_\xi)(\xi_L - \xi)) \tag{4.56}$$

- Kinetic law of damage evolution:

$$\dot{\underline{\underline{D}}} = \underline{\underline{C}}\ \underline{\underline{Y}}\ \underline{\underline{C}}^T \dot{p} H(p - p_D) \tag{4.57}$$

- The constitutive law:

$$\tilde{\underline{\underline{\sigma}}} = \underline{\underline{\underline{\underline{E}}}} : \left(\underline{\underline{\epsilon}} - \underline{\underline{\epsilon}}^p - \underline{\underline{\epsilon}}^{th} - \xi \underline{\underline{\epsilon}}^{bs}\right) \tag{4.58}$$

- The stress-effective stress relation:

$$\underline{\underline{\sigma}} = \underline{\underline{\underline{\underline{M}}}} : \tilde{\underline{\underline{\sigma}}} \tag{4.59}$$

  with the damage effect tensor:

$$\underline{\underline{\underline{\underline{M}}}} = \frac{1}{2}\underline{\underline{\underline{\underline{I}}}} - \frac{1}{4}\left[\underline{\underline{D}} \underline{\otimes} \underline{\underline{I}} + \underline{\underline{D}} \bar{\otimes} \underline{\underline{I}} + \underline{\underline{I}} \underline{\otimes} \underline{\underline{D}} + \underline{\underline{I}} \bar{\otimes} \underline{\underline{D}}\right] \tag{4.60}$$

- Yield surface is defined by:

$$f_c\left(\tilde{\underline{\underline{\sigma}}},\ \underline{\underline{X}},\ R\right) = J_2\left(\tilde{\underline{\underline{\sigma}}} - \underline{\underline{X}}\right) - \sigma_y - R \tag{4.61}$$

- The associated flow rule:

$$\mathrm{d}\underline{\underline{\epsilon}}^p = \frac{\partial f_c}{\partial \underline{\underline{\sigma}}} \mathrm{d}\lambda \tag{4.62}$$

- The evolution laws for the hardening parameters:

$$\dot{\underline{\underline{X}}} = \frac{2}{3} g(\xi) \dot{\underline{\underline{\epsilon}}}^p \tag{4.63}$$

$$\dot{R} = f(\xi)\dot{p} \tag{4.64}$$

  where the functions $g(\xi)$ and $f(\xi)$ were defined in the previous chapters.

4.4 Local approach in the damage mechanics

There is not much evidence for the interaction between the martensite sites and micro-damage fields. It has been postulated (cf. [92]) that short cracks nucleate in the austenite phase, like in stable steels, but their propagation is decelerated by brittle martensite islands which act as effective microstructural barriers. But this has not been verified. It seems that the so-called bain strain, associated with formation of the martensite inclusions, can favorize local development of damage fields. Also, the martensite platelets are usually carriers of the short cracks [93], that contribute to the state of damage. Thus, the phase transformation at cryogenic temperatures leads to

an increase in the intensity of local damage fields.
In a mesoscopic approach, the damage parameter is defined as the surface density of microcracks, microvoids in the RVE (eq. 4.1). In a microscopic approach, the local damage parameter at a point is defined by:

$$D_\mu = \frac{\mathrm{d}S_D}{\mathrm{d}S} \tag{4.65}$$

The mesoscopic damaged surface S_D is decomposed into the damaged surface in the austenite S_D^γ and in the martensite S_D^α (Fig. 4.5):

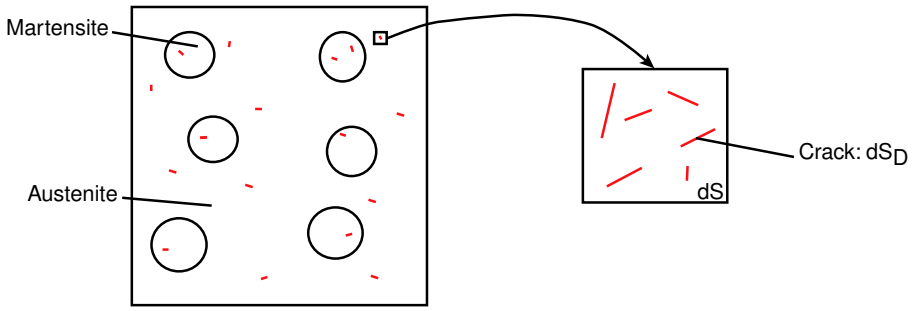

Figure 4.5: Damaged two-phase RVE

$$\begin{aligned} D &= \frac{S_D^\gamma}{S} + \frac{S_D^\alpha}{S} = \frac{1}{S}\int_{S^\gamma} \mathrm{d}S_D + \frac{1}{S}\int_{S^\alpha} \mathrm{d}S_D \\ D &= \frac{1}{S}\int_{S^\gamma} D_\mu \mathrm{d}S + \frac{1}{S}\int_{S^\alpha} D_\mu \mathrm{d}S \\ D &= D^\gamma(1-\xi) + D^\alpha \xi \end{aligned} \tag{4.66}$$

with

$$D^i = \frac{1}{S^i}\int_{S^i} D_\mu \mathrm{d}S \text{ with } i = \alpha, \gamma \tag{4.67}$$

D^i corresponds to the average damage for a given phase.

Several authors show that no clivage is observable after the rupture at low temperature [76, 77, 94]. The damage mechanism is also ductile. For each phase, we propose an evolution law, following the concept Lemaitre [78], that applies well to the ductile damage:

$$\begin{cases} \dot{D}^\gamma &= \left(\frac{Y^\gamma}{S^\gamma}\right) \dot{p}^\gamma H(p^\gamma - p_D^\gamma) \\ \dot{D}^\alpha &= \left(\frac{Y^\alpha}{S^\alpha}\right) \dot{p}^\alpha H(p^\alpha - p_D^\alpha) \end{cases} \tag{4.68}$$

The term Y is defined for each phase as follows:

$$Y^i = \frac{1}{2}\underline{\underline{\tilde{\sigma}}}^i : \underline{\underline{\underline{\underline{E}}}}^{i-1} : \underline{\underline{\tilde{\sigma}}}^i \tag{4.69}$$

where

$$\underline{\underline{\tilde{\sigma}}}^i = \frac{< \underline{\underline{\sigma}} >_i}{1 - D^i} \text{ with } i = \alpha, \gamma \tag{4.70}$$

Here, $< x > |_\Omega$ denotes the average of the variable x on the volume defined by Ω:

$$< x > |_\Omega = \frac{1}{V_\Omega} \int_\Omega x \mathrm{d}\Omega \tag{4.71}$$

Local variables have to be determined form the mesoscopic variables. Eshelby's analysis has been carried out to this end.

4.5 Problem of an elastic-plastic damageable inclusion in an elastic-plastic matrix

4.5.1 The Eshelby analysis

The standard Eshelby problem is related to an elastic inclusion embedded into an elastic matrix, both having the same elastic properties but with different free strains. In this Thesis, a similar problem of an inclusion in a matrix is considered (Fig. 4.6).

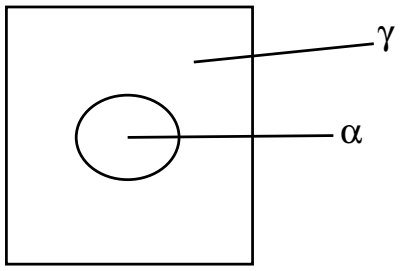

Figure 4.6: Inclusion in the matrix

The conditions at infinity are the following:

- Homogeneous strain field: $\underline{\underline{E}}_0$
- Homogeneous stress field: $\underline{\underline{\Sigma}}_0$

The local constitutive laws for each phase are given by:

$$\begin{cases} \underline{\underline{\sigma}}^\alpha = \underline{\underline{\underline{\underline{E}}}}^\alpha : \left(\underline{\underline{\epsilon}}^\alpha - \underline{\underline{\epsilon}}_f^\alpha \right) & \text{for the inclusion } \alpha \\ \underline{\underline{\sigma}}^\gamma = \underline{\underline{\underline{\underline{E}}}}^\gamma : \left(\underline{\underline{\epsilon}}^\gamma - \underline{\underline{\epsilon}}_f^\gamma \right) & \text{for the matrix } \gamma \end{cases} \tag{4.72}$$

where $\underline{\underline{\sigma}}$, $\underline{\underline{\epsilon}}$ and $\underline{\underline{\epsilon}}_f$ denote the stress tensor, the total strain tensor and the free strain tensor, respectively. The fourth order elasticity tensor of the phase i is given by:

$$\underline{\underline{\underline{\underline{E}}}}^i = 3k_i \underline{\underline{\underline{\underline{J}}}} + 2\mu_i \underline{\underline{\underline{\underline{K}}}} \tag{4.73}$$

The problem is transformed into a standard Eshelby analysis [70] [95], that is defined for an inclusion having the same properties as the matrix and subjected to a free strain (Fig. 4.7).

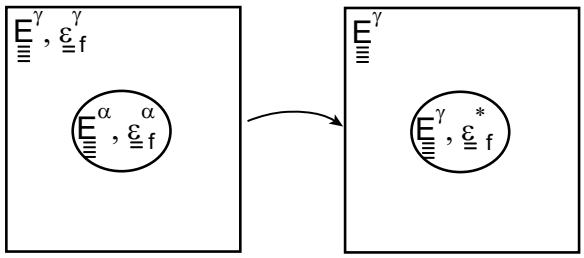

Figure 4.7: Transformation into an Eshelby analysis

$\underline{\underline{\epsilon}}_f^*$ denotes an equivalent free strain. It corresponds to a polarisation given by (cf. [68]):

$$\underline{\underline{\tau}} = \underline{\underline{\underline{\underline{E}}}}^\gamma : \underline{\underline{\epsilon}}_f^* \tag{4.74}$$

The solution of the problem is assumed as a sum of a term, which corresponds to the solution without the inclusion, and a term, which corresponds to the perturbation due to the inclusion:

$$\begin{cases} \underline{\underline{\epsilon}} = \underline{\underline{E}}_0 + \underline{\underline{\epsilon}}' \\ \underline{\underline{\sigma}} = \underline{\underline{\underline{\underline{E}}}}^\gamma : \left(\underline{\underline{E}}_0 - \underline{\underline{\epsilon}}_f^\gamma \right) + \underline{\underline{\sigma}}' \end{cases} \tag{4.75}$$

The set of equations 4.72 becomes:

$$\begin{cases} \underline{\underline{\sigma}}^\alpha = \underline{\underline{\underline{\underline{E}}}}^\alpha : \left(\underline{\underline{E}}_0 - \underline{\underline{\epsilon}}_f^\alpha \right) + \underline{\underline{\underline{\underline{E}}}}^\alpha : \underline{\underline{\epsilon}}^{\alpha\prime} & \text{for the inclusion } \alpha \\ \underline{\underline{\sigma}}^\gamma = \underline{\underline{\underline{\underline{E}}}}^\gamma : \left(\underline{\underline{E}}_0 - \underline{\underline{\epsilon}}_f^\gamma \right) + \underline{\underline{\underline{\underline{E}}}}^\gamma : \underline{\underline{\epsilon}}^{\gamma\prime} & \text{for the matrix } \gamma \end{cases} \tag{4.76}$$

Thus, the set 4.72 can be expressed as a function of the perturbation terms:

$$\begin{cases} \underline{\underline{\sigma}}^{\alpha\prime} = \underline{\underline{\underline{\underline{E}}}}^\alpha : \left(\underline{\underline{E}}_0 - \underline{\underline{\epsilon}}_f^\alpha \right) + \underline{\underline{\underline{\underline{E}}}}^\alpha : \underline{\underline{\epsilon}}^{\alpha\prime} - \underline{\underline{\underline{\underline{E}}}}^\gamma : \left(\underline{\underline{E}}_0 - \underline{\underline{\epsilon}}_f^\gamma \right) & \text{for the inclusion } \alpha \\ \underline{\underline{\sigma}}^{\gamma\prime} = \underline{\underline{\underline{\underline{E}}}}^\gamma : \underline{\underline{\epsilon}}^{\gamma\prime} & \text{for the matrix } \gamma \end{cases} \tag{4.77}$$

From the system 4.77, the equation for the inclusion reads:

$$\underline{\underline{\sigma}}^{\alpha\prime} = \underline{\underline{\underline{\underline{E}}}}^{\gamma} : \underline{\underline{\epsilon}}^{\alpha\prime} + \underline{\underline{\tau}} \tag{4.78}$$

with

$$\underline{\underline{\tau}} = \left(\underline{\underline{\underline{\underline{E}}}}^{\alpha} - \underline{\underline{\underline{\underline{E}}}}^{\gamma}\right) : \underline{\underline{\epsilon}}^{\alpha\prime} + \underline{\underline{\underline{\underline{E}}}}^{\alpha} : \left(\underline{\underline{E}}_0 - \underline{\underline{\epsilon}}_f^{\alpha}\right) - \underline{\underline{\underline{\underline{E}}}}^{\gamma} : \left(\underline{\underline{E}}_0 - \underline{\underline{\epsilon}}_f^{\gamma}\right)$$

Or in a different form:

$$\underline{\underline{\tau}} = \left(\underline{\underline{\underline{\underline{E}}}}^{\alpha} - \underline{\underline{\underline{\underline{E}}}}^{\gamma}\right) : \underline{\underline{\epsilon}}^{\alpha\prime} + \underline{\underline{\tau}}_0$$

Thus, the problem can be identified as Eshelby analysis [70]:

$$\begin{cases} \underline{\underline{\sigma}}^{\alpha\prime} = \underline{\underline{\underline{\underline{E}}}}^{\gamma} : \underline{\underline{\epsilon}}^{\alpha\prime} + \underline{\underline{\tau}} & \text{for the inclusion } \alpha \\ \underline{\underline{\sigma}}^{\gamma\prime} = \underline{\underline{\underline{\underline{E}}}}^{\gamma} : \underline{\underline{\epsilon}}^{\gamma\prime} & \text{for the matrix } \gamma \end{cases} \tag{4.79}$$

If the free strain field is assumed homogeneous in the inclusion and the inclusion is an ellipsoide, the Eshelby's solution gives:

$$\underline{\underline{\epsilon}}^{\alpha\prime} = -\underline{\underline{\underline{\underline{P}}}}^{\gamma} : \underline{\underline{\tau}} \tag{4.80}$$

where $\underline{\underline{\underline{\underline{P}}}}^{\gamma}$ is the Hills tensor (cf. [68]) which depends on the material properties of the matrix and on the inclusion geometry. The total strain in the inclusion is as follows:

$$\underline{\underline{\epsilon}}^{\alpha} = \underline{\underline{E}}_0 + \underline{\underline{\epsilon}}^{\alpha\prime}$$

$$\underline{\underline{\epsilon}}^{\alpha} = \underline{\underline{E}}_0 - \underline{\underline{\underline{\underline{P}}}}^{\gamma} : \left(\left(\underline{\underline{\underline{\underline{E}}}}^{\alpha} - \underline{\underline{\underline{\underline{E}}}}^{\gamma}\right) : \left(\underline{\underline{\epsilon}}^{\alpha} - \underline{\underline{E}}_0\right) + \underline{\underline{\tau}}_0\right) \tag{4.81}$$

Thus, the total strain tensor in the inclusion is given by:

$$\underline{\underline{\epsilon}}^{\alpha} = \underline{\underline{E}}_0 - \left(\underline{\underline{\underline{\underline{C}}}}^{*} + \underline{\underline{\underline{\underline{E}}}}^{\alpha}\right)^{-1} : \underline{\underline{\tau}}_0 \tag{4.82}$$

with

$$\underline{\underline{\underline{\underline{C}}}}^{*} = \underline{\underline{\underline{\underline{P}}}}^{\gamma-1} - \underline{\underline{\underline{\underline{E}}}}^{\gamma} \tag{4.83}$$

The stress tensor in the inclusion is given by:

$$\underline{\underline{\sigma}}^{\alpha} = \underline{\underline{\Sigma}}_0 - \underline{\underline{\underline{\underline{C}}}}^{*} : \left(\underline{\underline{\epsilon}}^{\alpha} - \underline{\underline{E}}_0\right) \tag{4.84}$$

$$\underline{\underline{\sigma}}^{\alpha} = \underline{\underline{\Sigma}}_0 + \underline{\underline{\underline{\underline{C}}}}^{*} : \left(\underline{\underline{\underline{\underline{C}}}}^{*} + \underline{\underline{\underline{\underline{E}}}}^{\alpha}\right)^{-1} : \underline{\underline{\tau}}_0 \tag{4.85}$$

In the matrix, the average stress tensor is given by:

$$< \underline{\underline{\sigma}} >_{\gamma} = \underline{\underline{\Sigma}}_0 - \frac{\xi}{1-\xi}\, \underline{\underline{\underline{\underline{C^*}}}} : \left(\underline{\underline{\underline{\underline{C^*}}}} + \underline{\underline{\underline{\underline{E^{\alpha}}}}} \right)^{-1} : \underline{\underline{\tau}}_0 \tag{4.86}$$

where ξ denotes the martensite volumic fraction.
If the inclusion is spherical and isotropic, the influence tensor is given by:

$$\underline{\underline{\underline{\underline{C^*}}}} = 3k^* \underline{\underline{\underline{\underline{J}}}} + 2\mu^* \underline{\underline{\underline{\underline{K}}}} = 4\mu^{\gamma} \underline{\underline{\underline{\underline{J}}}} + \frac{\mu^{\gamma}\left(9k^{\gamma}+8^{\gamma}\right)}{3\left(k^{\gamma}+2\mu^{\gamma}\right)} \underline{\underline{\underline{\underline{K}}}} \tag{4.87}$$

To introduce the damage and under the assumption that the initial elastic properties are equal for the phases, the elastic stiffness tensor of each phase reads:

$$\underline{\underline{\underline{\underline{E^{\alpha}}}}} = \underline{\underline{\underline{\underline{E}}}}\left(1-D^{\alpha}\right) \tag{4.88}$$

$$\underline{\underline{\underline{\underline{E^{\gamma}}}}} = \underline{\underline{\underline{\underline{E}}}}\left(1-D^{\gamma}\right) \tag{4.89}$$

where D^{γ} and D^{α} denote the damage in the matrix and in the inclusion, respectively.

Application to the strain induced martensitic transformation at low temperatures

Plastic strain can be regarded as free strain [96, 97]. In the case of the strain induced martensitic transformation, the free strains are defined by:

- $\underline{\underline{\epsilon}}_f^{\alpha} = \underline{\underline{\epsilon}}_{th}^{\alpha} + \underline{\underline{\epsilon}}_p^{\alpha} + \underline{\underline{\epsilon}}_{bs}$ for the inclusion
- $\underline{\underline{\epsilon}}_f^{\gamma} = \underline{\underline{\epsilon}}_{th}^{\gamma} + \underline{\underline{\epsilon}}_p^{\gamma}$ for the matrix

where $\underline{\underline{\epsilon}}_{th}$, $\underline{\underline{\epsilon}}_p$ and $\underline{\underline{\epsilon}}_{bs}$ denote the thermal strain, the plastic strain and the bain strain, respectively.

4.5.2 Mesoscopic-microscopic relations

To define the evolution of the behavior of each phase, the (microsopic) state variables of each phase have to be known from the mesoscopic ones. The Eshelby analysis allows writing the stress tensors in both phases (in average for the matrix) as a function of the mesoscopic stress tensor.

The mesoscopic constitutive law is given by:

$$\underline{\underline{\Sigma}} = \underline{\underline{\underline{\underline{E}}}}(1-D) : \left(\underline{\underline{E}} - \underline{\underline{E}}_p - \underline{\underline{E}}_{th} - \underline{\underline{E}}_{PT} \right) \tag{4.90}$$

where $\underline{\underline{E}}_p$, $\underline{\underline{E}}_{th}$ and $\underline{\underline{E}}_{PT}$ denote the mesoscopic plastic strain, the mesoscopic thermal strain and the distorsionnal strain field associated to the phase transformation, respectively.
The mesoscopic stress tensor is defined by:

$$\underline{\underline{\Sigma}} = <\underline{\underline{\sigma}}>|_{REV} \tag{4.91}$$

Thus

$$\underline{\underline{\Sigma}} = <\underline{\underline{\sigma}}>|_{REV} = <\underline{\underline{\underline{\underline{\tilde{E}}}}} : \underline{\underline{\epsilon}}_e>|_{REV} \tag{4.92}$$

$$\begin{aligned}\underline{\underline{\Sigma}} &= (1-\xi)(1-D^\gamma)\underline{\underline{\underline{\underline{E}}}} : \left(<\underline{\underline{\epsilon}}>_\gamma - <\underline{\underline{\epsilon}}_p>_\gamma - \underline{\underline{\epsilon}}^\gamma_{th}\right) \\ &\quad + \xi(1-D^\alpha)\underline{\underline{\underline{\underline{E}}}} : \left(<\underline{\underline{\epsilon}}>_\alpha - <\underline{\underline{\epsilon}}_p>_\alpha - \underline{\underline{\epsilon}}^\alpha_{th} - \underline{\underline{\epsilon}}_{bs}\right)\end{aligned} \tag{4.93}$$

By identification, one can define the following relations:

$$\underline{\underline{E}}(1-D) = (1-\xi)(1-D^\gamma)<\underline{\underline{\epsilon}}>_\gamma + \xi(1-D^\alpha)<\underline{\underline{\epsilon}}>_\alpha \tag{4.94}$$

$$\underline{\underline{E}}_p(1-D) = (1-\xi)(1-D^\gamma)<\underline{\underline{\epsilon}}_p>_\gamma + \xi(1-D^\alpha)<\underline{\underline{\epsilon}}_p>_\alpha \tag{4.95}$$

$$\underline{\underline{E}}_{th}(1-D) = (1-\xi)(1-D^\gamma)\underline{\underline{\epsilon}}^\gamma_{th} + \xi(1-D^\alpha)\underline{\underline{\epsilon}}^\alpha_{th} \tag{4.96}$$

$$\underline{\underline{E}}_{PT}(1-D) = \xi(1-D^\alpha)\underline{\underline{\epsilon}}_{bs} \tag{4.97}$$

The stresses in both phases are obtained from the Eshelby analysis (the previous section). The local increments of accumulated plastic strain (or of plastic strain) have to be defined for each phase as a function of the mesoscopic accumulated plastic strain increment (or of plastic strain increment), at least in average:

$$<\dot{p}>_i = f_i\left(\dot{P}\right) \text{ or } <\dot{\underline{\underline{\epsilon}}}_p>_i = f_i\left(\dot{\underline{\underline{E}}}_p\right)$$

with

$$\dot{P} = \sqrt{\frac{2}{3}\dot{\underline{\underline{E}}}_p : \dot{\underline{\underline{E}}}_p}$$

Considering the relation 4.95 and the assumption that if the equivalent stress in the inclusion is smaller than the yield point of martensite then the plastic strain rate is equal to 0 in the inclusion, the following relationships are proposed:

$$<\dot{\underline{\underline{\epsilon}}}_p>_\alpha = \dot{\underline{\underline{E}}}_p H(\tilde{\sigma}^\alpha_{eq} - \sigma^\alpha_y) \tag{4.98}$$

$$<\dot{\underline{\underline{\epsilon}}}_p>_\gamma = \frac{(1-D) - \xi(1-D^\alpha)H(\tilde{\sigma}^\alpha_{eq} - \sigma^\alpha_y)}{(1-D^\gamma)(1-\xi)}\dot{\underline{\underline{E}}}_p \tag{4.99}$$

where H denotes the Heavyside function.
These relations hold if the increments of damage and martensitic fraction are small. So the accumulated plastic strain rates, defined in the damage evolution law, read:

$$\dot{p}^{\alpha} = \dot{P} H(\tilde{\sigma}^{\alpha}_{eq} - \sigma^{\alpha}_{y}) \tag{4.100}$$

$$\dot{p}^{\gamma} = \frac{(1-D) - \xi(1-D^{\alpha}) H(\tilde{\sigma}^{\alpha}_{eq} - \sigma^{\alpha}_{y})}{(1-D^{\gamma})(1-\xi)} \dot{P} \tag{4.101}$$

The final set of the constitutive equations resumes to:

- Kinetics of the martensitic transformation

$$\dot{\xi} = A(T,\ \underline{\underline{\epsilon}}^{p},\ \underline{\underline{\sigma}}) \dot{P} H((p - p_{\xi})(\xi_{L} - \xi)) \tag{4.102}$$

- The constitutive law:

$$\underline{\underline{\Sigma}} = \underline{\underline{\underline{\underline{E}}}}(1-D) : \left(\underline{\underline{E}} - \underline{\underline{E}}_{p} - \underline{\underline{E}}_{th} - \underline{\underline{E}}_{PT} \right) \tag{4.103}$$

- The yield surface:

$$f_{c}\left(\underline{\underline{\tilde{\Sigma}}},\ \underline{\underline{X}},\ R \right) = J_{2}\left(\underline{\underline{\tilde{\Sigma}}} - \underline{\underline{X}} \right) - \sigma_{y} - R \tag{4.104}$$

- The associated flow rule:

$$\mathrm{d}\underline{\underline{\epsilon}}_{p} = \frac{\partial f_{c}}{\partial \underline{\underline{\Sigma}}} \mathrm{d}\lambda = \frac{3}{2} \frac{\underline{\underline{\tilde{s}}} - \underline{\underline{X}}}{J_{2}\left(\underline{\underline{\tilde{\Sigma}}} - \underline{\underline{X}} \right)} \frac{\mathrm{d}\lambda}{1-D} \tag{4.105}$$

- The hardening laws:

$$\underline{\dot{X}} = \frac{2}{3}(C + 3\beta(1-\xi)(\mu_{MT} - \mu_{t_a})) \underline{\underline{\dot{E}}}_{p}(1-D) \tag{4.106}$$

$$\dot{R} = (1-\xi)(1-\beta)(3(\mu_{MT} - \mu_{t_a}) - R) \dot{P}(1-D) \tag{4.107}$$

- The localisation relations:

$$D = (1-\xi)D^{\gamma} + \xi D^{\alpha} \tag{4.108}$$

$$\dot{p}^{\alpha} = \dot{P} H(\tilde{\sigma}^{\alpha}_{eq} - \sigma^{\alpha}_{y}) \tag{4.109}$$

$$\dot{p}^{\gamma} = \frac{(1-D) - \xi(1-D^{\alpha}) H(\tilde{\sigma}^{\alpha}_{eq} - \sigma^{\alpha}_{y})}{(1-D^{\gamma})(1-\xi)} \dot{P} \tag{4.110}$$

$$\underline{\underline{\sigma}}^{\alpha} = \underline{\underline{\Sigma}} + \underline{\underline{\underline{\underline{C}}}}^{*} : \left(\underline{\underline{\underline{\underline{C}}}}^{*} + \underline{\underline{\underline{\underline{E}}}}^{\alpha} \right)^{-1} : \underline{\underline{\tau}}_{0} \tag{4.111}$$

$$< \underline{\underline{\sigma}} >_{\gamma} = \underline{\underline{\Sigma}} - \frac{\xi}{1-\xi} \, \underline{\underline{\underline{\underline{C}}}}^{*} : \left(\underline{\underline{\underline{\underline{C}}}}^{*} + \underline{\underline{\underline{\underline{E}}}}^{\alpha} \right)^{-1} : \underline{\underline{\tau}}_{0} \tag{4.112}$$

with

$$\tau_0 = \underline{\underline{\underline{\underline{E}}}}^{\alpha} : \left(\underline{\underline{E}}_0 - \underline{\underline{\epsilon}}_f^{\alpha} \right) - \underline{\underline{\underline{\underline{E}}}}^{\gamma} : \left(\underline{\underline{E}}_0 - \underline{\underline{\epsilon}}_f^{\gamma} \right) \tag{4.113}$$

$$\underline{\underline{E}}_{th}(1-D) = (1-\xi)(1-D^{\gamma})\underline{\underline{\epsilon}}_{th}^{\gamma} + \xi(1-D^{\alpha})\underline{\underline{\epsilon}}_{th}^{\alpha} \tag{4.114}$$

$$\underline{\underline{E}}_{PT}(1-D) = \xi(1-D^{\alpha}) < \underline{\underline{\epsilon}}_{bs} > \tag{4.115}$$

- The damage evolution laws for both phases:

$$\dot{D}^{\gamma} = \left(\frac{Y^{\gamma}}{S^{\gamma}} \right) \dot{p}^{\gamma} H(p^{\gamma} - p_D^{\gamma}) \tag{4.116}$$

$$\dot{D}^{\alpha} = \left(\frac{Y^{\alpha}}{S^{\alpha}} \right) \dot{p}^{\alpha} H(p^{\alpha} - p_D^{\alpha}) \tag{4.117}$$

with

$$Y^{i} = \frac{1}{2} \underline{\underline{\tilde{\sigma}}}^{i} : \underline{\underline{\underline{\underline{E}}}}^{i-1} : \underline{\underline{\tilde{\sigma}}}^{i} \tag{4.118}$$

where

$$\underline{\underline{\tilde{\sigma}}}^{i} = \frac{< \underline{\underline{\sigma}} >_i}{1-D^i} \text{ with } i = \alpha, \gamma \tag{4.119}$$

4.6 Crack initiation criteria

4.6.1 Basic approach

For isotropic damage, the criterion of initiation of a mesocrack can be formulated in terms of critical damage [78, 98]:

$$D = D_{cr} \tag{4.120}$$

or in terms of energy:

$$Y = Y_{cr} \tag{4.121}$$

These criteria can be extended to anisotropic damage. Several limitations can be proposed either in terms of critical damage:

$$\text{Max}_i \; D_i = D_{cr} \tag{4.122}$$

where D_i are the eigenvalues of damage tensor, or taking into account the first invariant of damage tensor:

$$tr[\underline{\underline{D}}] = D_{cr} \tag{4.123}$$

or in terms of energy:

$$\text{Max}_i \; Y_i = Y_{cr} \tag{4.124}$$

or, finally:

$$tr[\underline{\underline{Y}}] = Y_{cr} \tag{4.125}$$

4.6.2 Localisation criteria

Other criteria can be based on the theory of strain localization [99]. Originally, it was applied to analyse shear bands in material: to predict the existence and orientation of shear bands within various types of materials. It was proposed by Hadamard [100] and developed by Rice [101].
The localization theory is based on the identification of a surface of discontinuity of the strain rate (displacements remain continuous) (Fig. 4.8). The surface S is defined

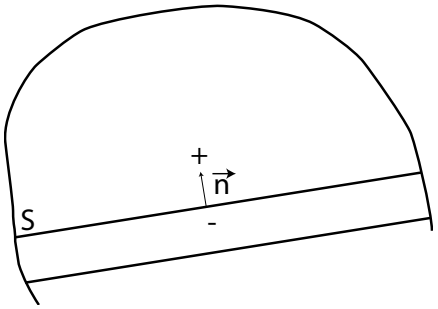

Figure 4.8: Discontinuity surface

by its normal $\vec{n}$. The variation of variable x across the surface S is defined as follows:

$$[\![x]\!] = x^+ - x^-$$

where the symbol $[\![x]\!]$ denotes a discontinuity of the variable (or function) x across the S surface. The problem can be formulated in terms of strain rate. The equations defining the localization phenomenon are the following:

$$\begin{cases} [\![\dot{\underline{\underline{\sigma}}}\vec{n}]\!] = \vec{0} & \text{Equilibrum equation at the surface S} \\ \dot{\underline{\underline{\sigma}}} = \underline{\underline{\underline{\underline{H}}}} : \dot{\underline{\underline{\epsilon}}} & \text{Constitutive law} \\ [\![\dot{\underline{\underline{\epsilon}}}]\!] = \frac{1}{2}(\vec{g} \otimes \vec{n} + \vec{n} \otimes \vec{g}) & \text{Compatibility equation (cf. [100])} \end{cases}$$

where $\underline{\underline{\underline{\underline{H}}}}$ stands for the tangent stiffness tensor, that depends on the damage D and $\vec{g}$ is a vector to be determined. If $\vec{g} = \vec{0}$ there is no discontinuity; $\vec{g} \neq \vec{0}$ is the sufficient

condition for existence of a discontinuity.
It has been shown that the condition of existence of a surface of discontinuity is equivalent to [78]:

$$\det[\vec{n}.\underline{\underline{\underline{\underline{H}}}}.\vec{n}] = 0 \tag{4.126}$$

The tensor $\vec{n}.\underline{\underline{\underline{\underline{H}}}}.\vec{n}$ corresponds to the acoustic tensor. If the equation 4.126 holds, a mesocrack will be initiated in the plane perpendicular to $\vec{n}$.

4.6.3 Propagation of a macrocrack in the anisotropic and heterogenous material

As soon as the crack initiation criteria is reached, a macrocrack can be considered in the material. The fracture mechanics has to be used to describe crack propagation. Usually, for homogeneous material, the direction of crack propagation is defined by the principal stress direction. The evolution of the size of the crack is linked to the stress intensity factor K, that is related to the stress field and to the crack geometry. For crack propagation in fatigue, a Paris law can be used to define the evolution of the length of the macrocrack, denoted by a:

$$\frac{\mathrm{d}a}{\mathrm{d}N} = C\Delta K^m \tag{4.127}$$

where ΔK denotes the range of the stress intensity factor over a cycle, m and C stand for material parameters.
For anisotropic material, the material parameters can influence the crack propagation direction. For the two-phase material, the influence of the martensite inclusions is not obvious. On one hand, martensite platelets could be considered as hard inclusion embedded in a soft matrix. So they could act as stoppers of the cracks. Moreover, the stress concentration in front of the crack tip induces plastic strain field and - consequently - plastic strain induced martensitic transformation, that decreases the stress level. Thus, on one hand the presence of martensite inclusions may reduce the crack propagation. On the other hand, the martensite platelets are usually carriers of short cracks, that can develop and create a macrocrack propagation through the martensite/austenite interface.
For thin-walled shells, the crack propagation is fast (measured via the vacuum degradation rate). It leads to a fracture of bellows in a few cycles.

4.7 Choice of the model

4.7.1 Mesoscopic approach

Two models have been presented: the first one corresponds to an Uncoupled Phase Transformation Isotropic DAmage MEsoscopic Model (UPTIDAMEM) and the second one is an Uncoupled Phase Transformation Orthotropic DAmage MEsoscopic Model (UPTODAMEM)
The UPTIDAMEM model is based on the model of phase transformation (Section 3) and the isotropic ductile damage model, as proposed by Chaboche [85] and Lemaitre [78]. The damage model is useful in any case. Damage parameters are easily identified. Nevertheless, it is not representative of all the observed phenomena: it does take into account the difference of behaviour of the two constitutive phases and does not represent the direction that is priviliged for the evolution of damage.
As the UPTIDAMEM model, the other model is based on the phase transformation (Section 3) but with an orthotropic ductile damage. It is well adapted for thin-walled shells, that are axisymetric in terms of the geometry and the applied loads. Damage parameters are easily identifiable. The damage model can be incoherent when one eigenvalue of the stress tensor is much smaller (negligible) with respect to the others . It takes into account the difference of behaviour of the two constitutive phases.
A comparison of the two models is made for an axisymmetric geometry (Fig. 4.9). For both models half convolution is subjected to the same cycle tension/compression.

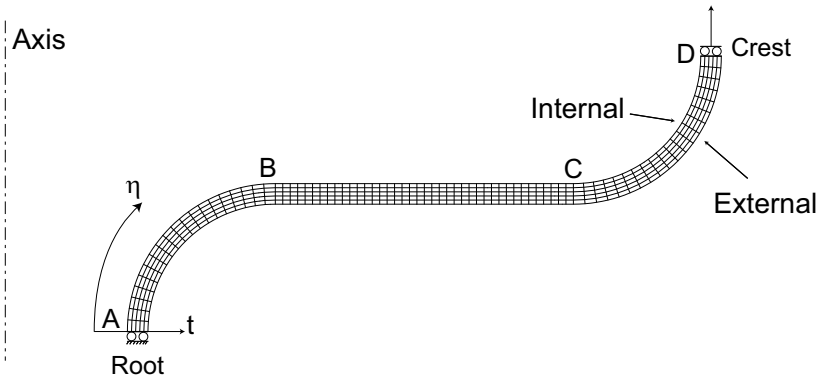

Figure 4.9: Axisymetric model

The parameters of elasticity, plasticity and of the kinetic law of phase transformation have been set equal for both models. For the isotropic damage law, the tensor of parameters is under the following form:

$$\underline{\underline{C}} = C\underline{\underline{I}} \tag{4.128}$$

where C is linked to the strength energy of damage, S, used in the isotropic damage evolution law. It obeys the following law:

$$C^2 = \frac{1}{S} \tag{4.129}$$

The evolution of damage for UPTIDAMEM and UPTODAMEM models, along the internal and external surface of the bellows convolution, are presented in Figs. 4.10 and 4.11, respectively. For UPTODAMEM model, the damage obtained in the direction normal to the mid-surface is not shown in Fig. 4.11 because it is negligible when compared to the other directions (as expected according to the shell theory). The global evolution of damage for both models is the same. The most intensive damage accumulation occurs at root and at crest of the convolution, where a strong localisation of plastic strains takes place.

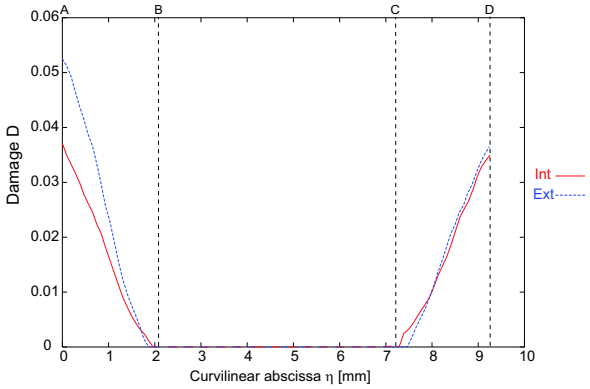

Figure 4.10: Isotropic damage along half-convolution of bellows

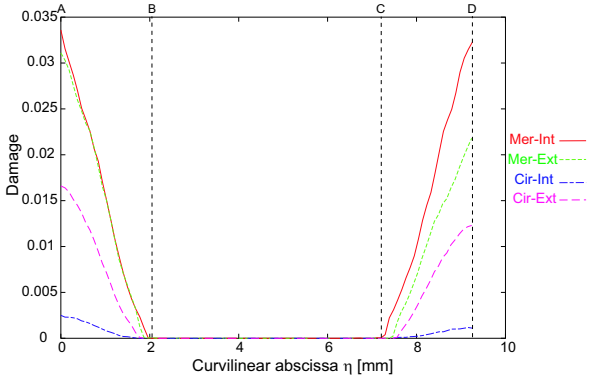

Figure 4.11: Meridional and circumferential damage along half-convolution of bellows

In this particular case (eq. 4.129), the isotropic damage intensity (D) can be regarded as a superposition of the meridional and the circumferential damage intensities (D_Φ, D_θ) in the orthotropic case (it is sufficient to perform a contraction of the eq. 4.36). The damage in the meridional direction seems to dominate, which induces circumferential micro-crack fields. This fact has been experimentally confirmed (Fig. 4.12).

4.7.2 Microscopic approach

It corresponds to an Uncoupled Phase Transformation Isotropic DAmage MIcroscopic Model (UPTIDAMIM). This model has been created to take into account the difference of behaviour between the two phases. Based on the average values of state variables, it does not take into account the strain localisation in the austenite, in the vicinity of

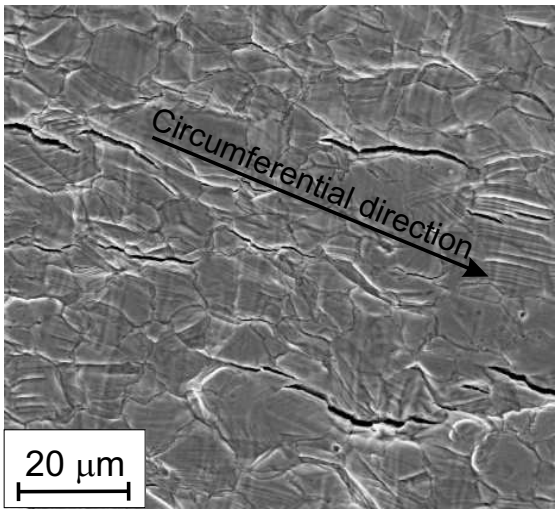

Figure 4.12: Crack field at root of convolution of a bellows tested at 77 K

the martensitic platelets which occurs due to the bain strain. Moreover, microscopic material parameters are difficult to determine, especially for the martensite.
It is not excluded that the increase of damage in the martensite leads to an increase of the martensite content (localisation of the strain in front of the crack tip). The coupling between damage and phase transformation might be introduced by reading the martensitic content rate as a function of the damage parameter in the martensite:

$$\dot{\xi} = A(T, D_\alpha)\dot{p}H((p - p_\xi)(\xi_L - \xi))$$

4.7.3 Retained model

Taking into account the difficulties to measure the parameters in a microscopic scale, the UPTIDAMIM model has been excluded, although it seems to be closer to the reality by distinguishing between the parameters of both phases.
Finally, the robustness of the UPTIDAMEM and the relative simplicity to identify the material parameters at cryogenic temperatures leads to the choice of this model when analysing the behaviour of the bellows expansion joints.

Chapter 5

Application of the constitutive model

5.1 Identification of the material parameters for different temperature levels

The material parameters have been identified at three levels of temperature: room temperature (293 K), 77 K and 4.2 K. Tensile tests at cryogenic temperatures are rather complex and expensive since the specimen must be immersed in a bath of liquid nitrogen (77 K) or liquid helium (4.2 K) inside a vacuum-insulated cryostat. The temperature of the bath has to be stabilized by using a cryogenic circuit. The strains are measured by two extensometers, calibrated at cold. A cell mounted outside the cryostat controls the force. Also, the strain rate has to be carefully controlled since the material behaviour at cold depends on the deformation rate. A photo of the set-up is presented in Fig. 5.1.

5.1.1 Plastic strain induced martensitic transformation at low temperatures

The method of measurement of the martensite content in the austenite phase is based on ferromagnetic properties of the BCC martensitic phase whereas the FCC austenitic phase is paramagnetic [102]. The increase in volume fraction of ferromagnetic martensite promoted by plastic deformation can be detected by measuring the magnetic permeability μ. Short reminder of magnetic features and methods of magnetic measurements are presented in Annex C.
Figure 5.2 (cf. [12]) shows a reference diagram which allows estimation of the martensitic content (volume fraction of martensite ξ). It presents the magnetic permeability μ as a function of the martensitic content ξ.
The diagram shows an initial permeability 1, which is not necessarily the case for

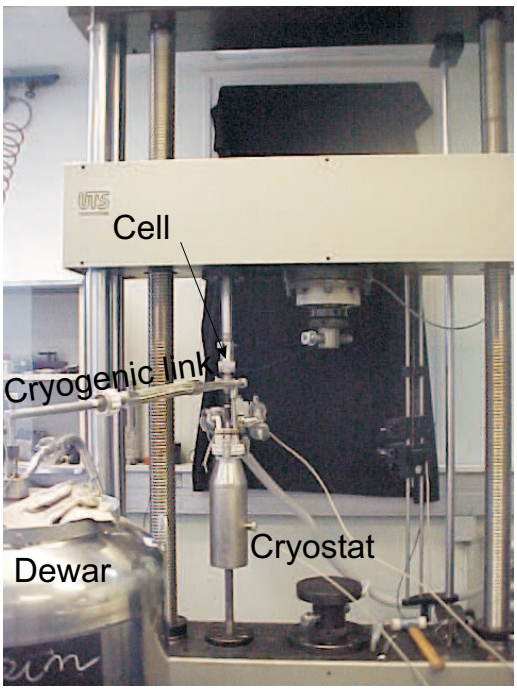

Figure 5.1: Tensile test set-up at 4.2 K

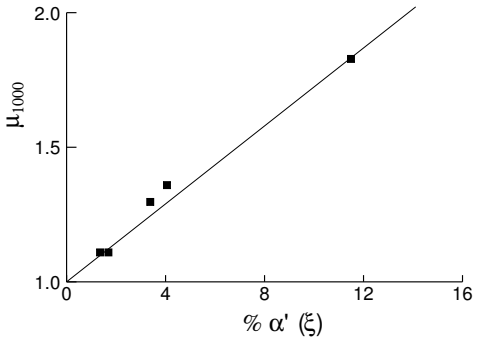

Figure 5.2: Magnetic permeability μ versus volume fraction of martensite for grades 304L, 321 and 347, strained at 4.2 K

austenitic stainless steels (typical values are 1.005). Thus, the presented diagram has to be regarded as a variation of permeability (with respect to 1).
The results of measurements of magnetic susceptibility as a function of the inelastic strains are shown in Fig. 5.3. They have been obtained (cf. [33, 102]) from 0.25 mm thick stainless steel sheets strained at three different temperatures (293 K, 77 K and 4.2 K). Figs. 5.3 through 5.6 show the primary importance of temperature for the strain induced martensitic transformation, with almost no phase transformation at

room temperature.

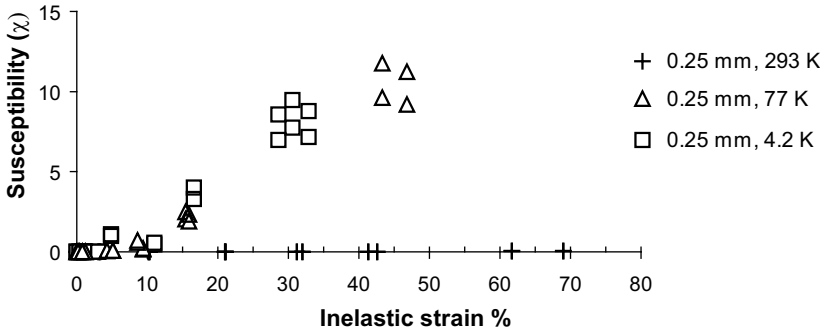

Figure 5.3: Magnetic susceptibility χ versus plastic strain at 293 K, 77 K and 4.2 K for the 316L stainless steel sheets, 0.25 mm thick

A more detailed analysis (Fig. 5.4) shows that the plastic strain induced martensitic transformation at 293 K occurs at high strain levels, but remains small (cf. [102]). Martensitic content does not exceed few precent (< 5 %).

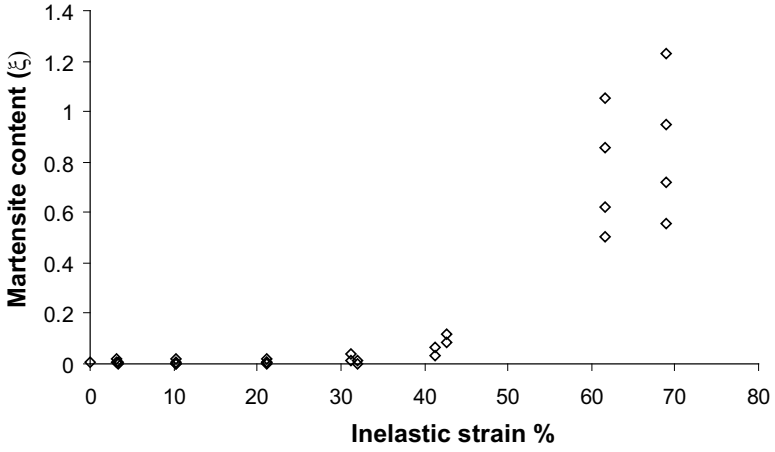

Figure 5.4: Martensitic content ξ versus plastic strain at 293 K for the 0.25 mm thick 316L stainless steel sheets

At cryogenic temperatures (Figs 5.5 and 5.6), the phase transformation is much more active. At 4.2 K, the test is more delicate because of the appearance of shear bands (serrated yielding) which lead to a localisation of plastic strains and thus of martensite platelets. Results presented in Fig. 5.6 have been obtained when no serrated yielding occured.
The identification of the parameters of the kinetic law of strain induced martensitic transformation is carried out on the basis of the curves of martensite content versus

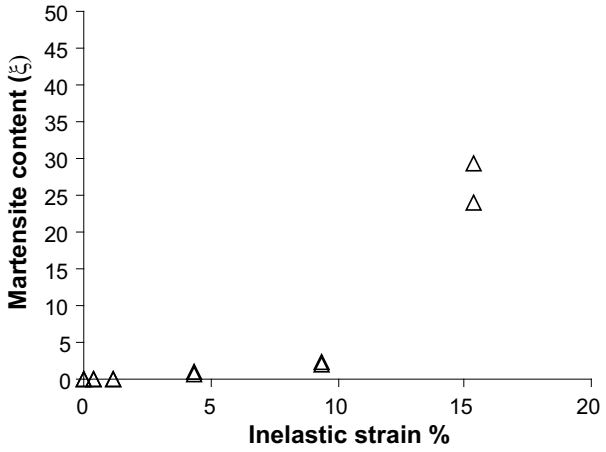

Figure 5.5: Martensitic content ξ versus plastic strain at 77 K for the sheet 0.25 mm thick

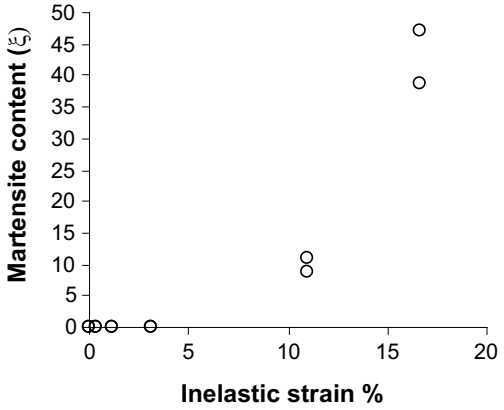

Figure 5.6: Martensitic content versus plastic strain at 4.2 K for the 0.25 mm thick stainless steel sheet

the inelastic strain (Figs. 5.4 through 5.6). The inelastic strain is decomposed into plastic strain ϵ^p and the bain strain ϵ^{bs}, according to the relationship:

$$\underline{\underline{\epsilon}}^{inel} = \underline{\underline{\epsilon}}^{p} + \xi \underline{\underline{\epsilon}}^{bs} \tag{5.1}$$

The volume fraction of martensite can be plotted as a function of the plastic strain. Linearization of the region II of the sigmoidal curve has been carried out by using the least square method (cf. [102]). The slope of the line and the intersection with the x-axis correspond to the function A and the threshold p_ξ, respectively. As an example, identification of the parameters for 0.25 mm thick 316L stainless steel sheet at 77 is shown in Fig. 5.7 (cf. [102]).

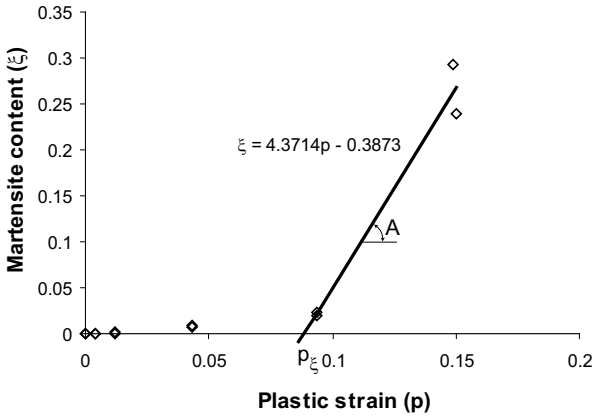

Figure 5.7: Identification of parameters of the kinetic law of martensitic transformation at 77 K for a 316L stainless steel sheet, 0.25 mm thick

The identification has been carried out for 3 temperatures (293 K, 77 K and 4.2 K). The values are shown Table 5.1 .

Temperature [K]	p_ξ	A
293	0.39	0.02
77	0.09	4.37
4.2	0.08	5.1

Table 5.1: Parameters of kinetic law of martensitic transformation at three temperature levels (293 K, 77 K and 4.2 K)

Evolution of the two parameters describing the plastic strain induced martensitic transformation, p_ξ and A, is given in Figs. 5.8 and 5.9 (cf. [102]).
It is worth pointing out, that the threshold p_ξ drops from 0.4 at room temperature to below 0.1 at 77 K and at 4.2 K. Thus, the material is more susceptible to plastic strain induced phase transformation at cold. As far as the intensity parameter A is concerned, it increases from $\simeq 0$ at room temperature to $4 \div 5$ at cryogenic temperatures (77-4.2 K).

5.1.2 Plastic strain induced damage

Identification of the parameters of the kinetic law of damage evolution is based on the loading/unloading uniaxial tensile test [78]. In the classical one-dimensional and

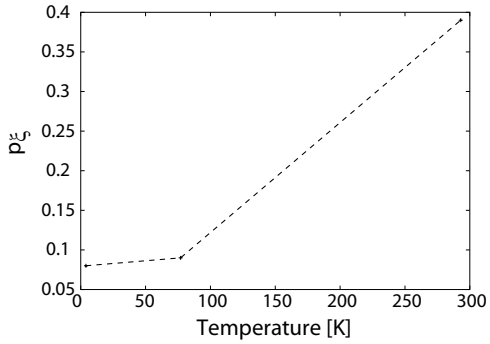

Figure 5.8: Plastic strain threshold (p_ξ) as a function of temperature

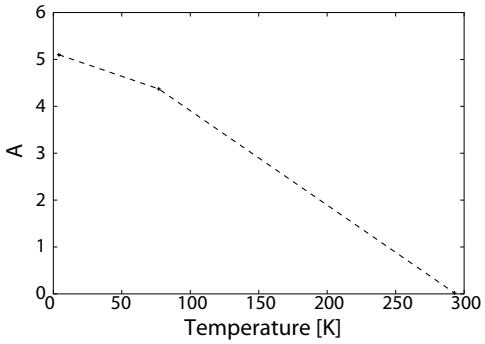

Figure 5.9: Intensity parameter (A) of the martensitic transformation as a function of temperature

isotropic case one obtains (cf. [78]):

$$Y = \frac{\sigma^2}{2E(1-D)^2} \tag{5.2}$$

and

$$\dot{D} = \frac{\sigma^2}{2ES(1-D)^2}\dot{\epsilon}^p H(\epsilon^p - \epsilon_D^p) \tag{5.3}$$

By tracing the evolution of the elasticity modulus during several loading/unloading trials, the damage parameter is obtained from:

$$D = 1 - \frac{\tilde{E}}{E} \tag{5.4}$$

where E and $\tilde{E}$ denote the initial and the current elasticity moduli, respectively (Fig. 5.10).
As an example, tensile curve obtained at 4.2 K from a 316 L fine gauge sheet of 0.25 mm

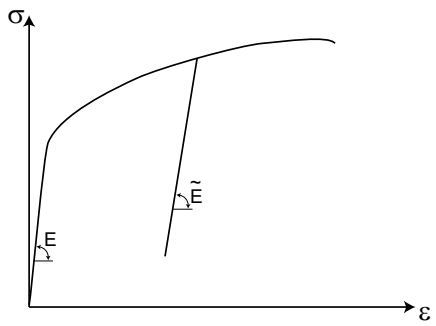

Figure 5.10: Identification of damage evolution in the one-dimensional case

thickness is shown in Fig. 5.11 (cf. [103]). The corresponding evolution of the damage parameter D as a function of the accumulated plastic strain is illustrated in Fig. 5.12.

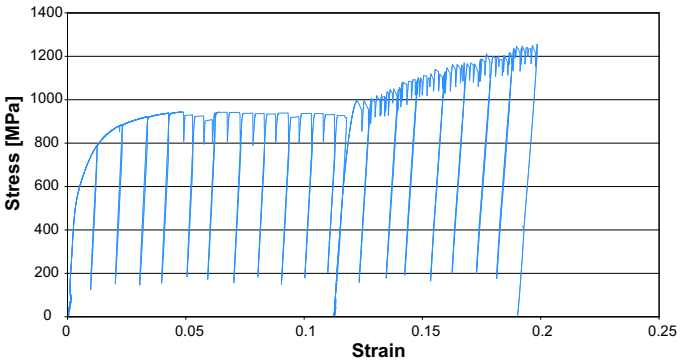

Figure 5.11: Tensile curve obtained at 4.2 K

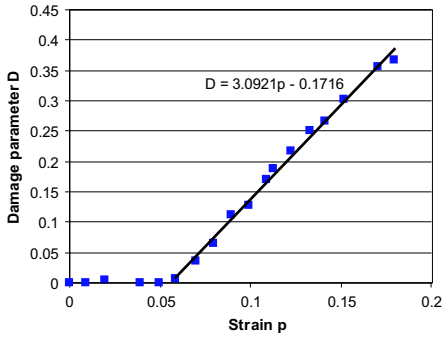

Figure 5.12: Evolution of damage parameter D as a function of plastic strain at 4.2 K

In this particular case the damage threshold, ϵ_D^p, has been identified close to 5.5 %. Above the threshold, the curve can be linearized and $\frac{\mathrm{d}D}{\mathrm{d}p}$ can be calculated leading to evaluation of the strength energy of damage S [78]:

$$S = \frac{\sigma^2}{2E(1-D)^2 \frac{\mathrm{d}D}{\mathrm{d}p}} \tag{5.5}$$

where p is equivalent to the plastic strain ϵ^p (one-dimensional case). Several points on the path are considered to obtain S as the best average. The identification has been carried out for 3 temperatures (293 K, 77 K and 4.2 K) and the corresponding values are presented in Table 5.2. The evolution of S with temperature is shown in Fig. 5.13.

Temperature [K]	293	77	4.2
S	0.43	1.05	1.27

Table 5.2: Strength energy of damage as a function of temperature for 316L fine gauge stainless steel sheets

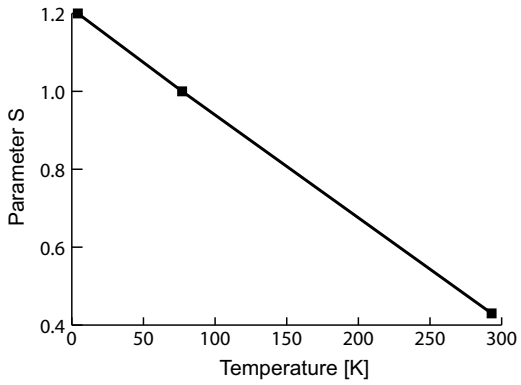

Figure 5.13: Evolution of the parameter S with temperature

It seems that a linear interpolation of the strength energy of damage with the temperature can be proposed:

$$S(T) = a.T + b \tag{5.6}$$

After identification of the parameters for grade 316L, the interpolation (Eq. 5.6) takes the form:

$$S(T) = -2.7\ 10^{-3}.T + 1.2085 \tag{5.7}$$

The values of the uniaxial damage threshold ϵ_D^p at different temperature levels are given in table. 5.3.

Temperature [K]	293	77	4.2
ϵ_p^D	0.02	0.024	0.026

Table 5.3: Uniaxial damage threshold as a function of temperature

Under the monotonic uniaxial loading, p_D corresponds to the uniaxial damage threshold ϵ_D^p, but under the cyclic loads p_D is a function of the applied stress [78]. The damage threshold is related to the amount of stored energy. Lemaitre [78] shows that the stored energy is equal to:

$$w_s = \int_0^p (\sigma_{eq} - \sigma_y)\mathrm{d}p \tag{5.8}$$

with

$$\sigma_{eq} = \sqrt{\frac{3}{2}\underline{\underline{\sigma}}^D : \underline{\underline{\sigma}}^D} \tag{5.9}$$

where $\underline{\underline{\sigma}}^D$ denotes the deviatoric stress and σ_y the yield point.
Chrysochoos [104] shows that the stored energy decreases with the plastic strain. Thus, an improvement of eq. 5.8 has been made by Sermage [105]:

$$\mathrm{d}w_s = (\sigma_{eq} - \sigma_y)\mathrm{d}p\frac{\epsilon_D^p}{\epsilon_D^p + p} \tag{5.10}$$

By transferring the stored energy to the three-dimensional case and in pure tension, having the damage threshold ϵ_D^p and with saturated hardening $\sigma_{eq} = \sigma_u$ at the level of the ultimate stress (reference case), the eq. 5.10 leads to the following relationship between p_D and ϵ_D^p (eq. 5.11) [105]:

$$p_D = \epsilon_D^p \left(exp\left(\frac{\sigma_u - \sigma_y}{\sigma_{eq} - \sigma_y} ln(2) \right) - 1 \right) \tag{5.11}$$

This relationship has been determined, considering that the material is perfectly plastic. In case of an elastic-plastic material with a kinematic hardening, the relationship between p_D and ϵ_D^p is as follows:

- For pure tension, the stored energy, until reaching the damage threshold, is determined by:

$$w_{sref} = \int_0^{\epsilon_D^p} Cp\frac{\epsilon_D^p}{\epsilon_D^p + p}\mathrm{d}p \tag{5.12}$$

  where C denotes the kinematic hardening modulus.

- For a cyclic loading, defined by the maximum equivalent stress σ_{eq}, the stored energy can be defined step by step (Fig. 5.14):

$$w_{si} = \sum_i \int_{i\frac{\sigma_{eq}-\sigma_y}{C}}^{(i+1)\frac{\sigma_{eq}-\sigma_y}{C}} C(p - i\frac{\sigma_{eq} - \sigma_y}{C})\frac{\epsilon_D^p}{\epsilon_D^p + p}\mathrm{d}p \tag{5.13}$$

  which leads to:

$$\begin{aligned} w_{si} \;=\; & \sum_i C\epsilon_D^p \left(\frac{\sigma_{eq} - \sigma_y}{C} - \epsilon_D^p ln\left(\frac{(i+1)\frac{\sigma_{eq}-\sigma_y}{C} + \epsilon_D^p}{i\frac{\sigma_{eq}-\sigma_y}{C} + \epsilon_D^p} \right) \right) \\ & -i(\sigma_{eq} - \sigma_y)\epsilon_D^p ln\left(\frac{(i+1)\frac{\sigma_{eq}-\sigma_y}{C} + \epsilon_D^p}{i\frac{\sigma_{eq}-\sigma_y}{C} + \epsilon_D^p} \right) \end{aligned} \tag{5.14}$$

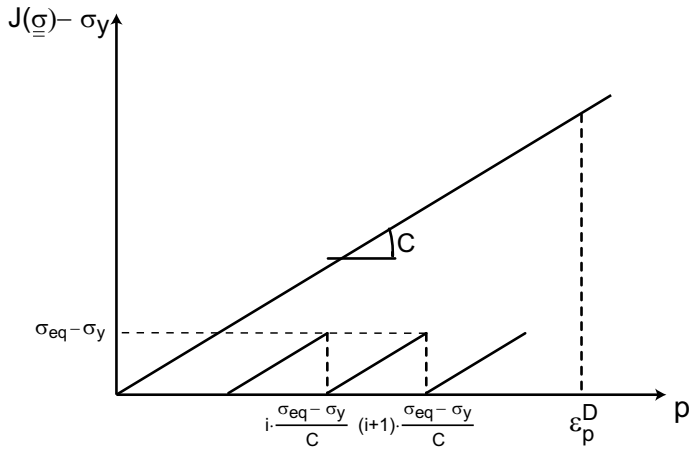

Figure 5.14: Stored energy in an elastic-plastic material with a linear kinematic hardening

- By equality of Eq. 5.12 and Eq. 5.14, the parameter "i" can be determined as larger, that satisfies:

$$w_{sref} > w_{si_D} \tag{5.15}$$

- The damage threshold is equal to:

$$p_D = i_D \frac{\sigma_{eq} - \sigma_y}{C} \tag{5.16}$$

5.2 Numerical integration of the constitutive equations

The constitutive model has been implemented in the finite element code CASTEM2000. The method of the type "radial return", originally proposed by Wilkins [106], is used to integrate the constitutive equations for an active plastic process. Definition of the finite element is based on the Updated Lagrangian formulation [107]. The integration of the constitutive modelling is based on the elastic-plastic split, by first integrating the elastic equations to obtain an elastic predictor, which is used as the initial condition for the plastic return [74]. A plastic corrector is calculated, whereby the elastically predicted stresses are relaxed onto a suitably updated yield surface. The algorithm is schematized in Fig. 5.15.
As an example, the damageable elastic-plastic model, taking into account the phase transformation and presented in section 4.2.1, is integrated. The other models do not present additional difficulties. The set of equations chosen for the numerical study is

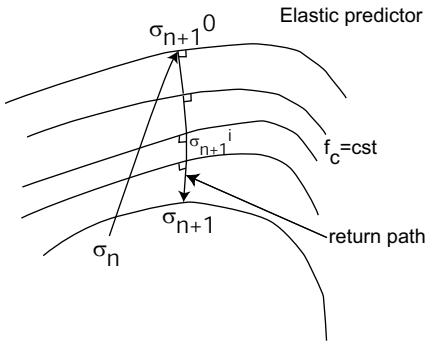

Figure 5.15: Return mapping algorithm

as follows:

$$\underline{\underline{\sigma}} = \underline{\underline{\underline{\underline{E}}}}(1-D) : \left(\underline{\underline{\epsilon}} - \underline{\underline{\epsilon}}^p - \xi \underline{\underline{\epsilon}}^{bs}\right) \tag{5.17}$$

$$f_c\left(\underline{\underline{\tilde{\sigma}}},\ \underline{\underline{X}},\ R\right) = J_2\left(\underline{\underline{\tilde{\sigma}}} - \underline{\underline{X}}\right) - \sigma_y - R \tag{5.18}$$

with $J_2\left(\underline{\underline{\tilde{\sigma}}} - \underline{\underline{X}}\right) = \sqrt{\frac{3}{2}\left(\underline{\underline{\tilde{s}}} - \underline{\underline{X}}\right) : \left(\underline{\underline{\tilde{s}}} - \underline{\underline{X}}\right)}$ and $\underline{\underline{\tilde{s}}} = \frac{\underline{\underline{\sigma}}}{1-D} - \frac{1}{3}Tr\left(\frac{\underline{\underline{\sigma}}}{1-D}\right)\underline{\underline{I}}$.
The normality rule reads:

$$\mathrm{d}\underline{\underline{\epsilon}}^p = \frac{\partial f_c}{\partial \underline{\underline{\sigma}}}\mathrm{d}\lambda = \underline{\underline{n}}\mathrm{d}\lambda \tag{5.19}$$

with

$$\underline{\underline{n}} = \frac{3}{2}\frac{\underline{\underline{\tilde{s}}} - \underline{\underline{X}}}{J_2\left(\underline{\underline{\tilde{\sigma}}} - \underline{\underline{X}}\right)}\frac{1}{1-D} \tag{5.20}$$

$$\mathrm{d}\lambda = (1-D)\mathrm{d}p \tag{5.21}$$

The evolution laws of the variables are as follows:

$$\mathrm{d}R = f(\xi)(1-D)\mathrm{d}p \tag{5.22}$$

$$\mathrm{d}\underline{\underline{X}} = \frac{2}{3}(1-D)g(\xi)\mathrm{d}\underline{\underline{\epsilon}}^p \tag{5.23}$$

$$\mathrm{d}\xi = A(T,\ \underline{\underline{\dot{\epsilon}}}^p,\ \underline{\underline{\sigma}})\mathrm{d}pH((p-p_\xi)(\xi_L - \xi)) \tag{5.24}$$

$$\mathrm{d}D = \left(\frac{Y}{S}\right)^s \mathrm{d}pH(p-p_D) \tag{5.25}$$

All variables are known at the time t. An increment of the total strain is applied:

$$\underline{\underline{\epsilon}}_{t+1} = \underline{\underline{\epsilon}}_t + \Delta\underline{\underline{\epsilon}} \tag{5.26}$$

The other variables are computed at the time $t+1$. The integration of the equations, to find a solution, is performed in two phases:
Phase 1: Elastic predictor.
The evolution is assumed to be elastic. Thus, all the variables, evolution of which depends on plasticity, are constants:

$$Q^0_{t+1} = Q_t \tag{5.27}$$

where

$$Q = \{R,\ p,\ D,\ \xi,\ \underline{\underline{\epsilon}}^p,\ \underline{\underline{\underline{\underline{X}}}}\} \tag{5.28}$$

The stress tensor is updated by performing the following operation:

$$\underline{\underline{\sigma}}^0_{t+1} = \underline{\underline{\sigma}}_t + \underline{\underline{\underline{\underline{E}}}}(1-D_t) : \Delta\underline{\underline{\epsilon}} \tag{5.29}$$

The term $f^{\,0}_{ct+1}$ defined by

$$f^{\,0}_{ct+1} = J_2\left(\underline{\underline{\tilde{\sigma}}}^0_{t+1} - \underline{\underline{\underline{\underline{X}}}}^0_{t+1}\right) - \sigma_y - R^0_{t+1} \tag{5.30}$$

is computed. If $f^{\,0}_{ct+1} \leq 0$ then the elastic predictor becomes the solution at the time $t+1$:

$$Q_{t+1} = Q_t \tag{5.31}$$

and

$$\underline{\underline{\sigma}}_{t+1} = \underline{\underline{\sigma}}^0_{t+1} \tag{5.32}$$

If $f^{\,0}_{ct+1} > 0$ then an iterative process of correction begins from the initial state defined by the elastic predicator.
Phase 2: Plastic corrector.
The term Q^i_{t+1} stands for the variable Q at the time $t+1$ and for the iteration i.
The relaxation process for stresses and variables associated with plasticity is carried out in a step-by-step way. At every iteration, the yield function f_c is linearized around the current value of the state variables to obtain

$$f_c = f^{\,i}_{ct+1} + \Delta f^{\,i}_{ct+1} \tag{5.33}$$

with

$$\begin{aligned}
\Delta f^{\,i}_{ct+1} &= \frac{\partial f_c}{\partial \underline{\underline{\sigma}}}\Big|^i_{t+1} : \left(\underline{\underline{\sigma}} - \underline{\underline{\sigma}}^i_{t+1}\right) \\
&+ \frac{\partial f_c}{\partial \underline{\underline{\underline{\underline{X}}}}}\Big|^i_{t+1} : \left(\underline{\underline{\underline{\underline{X}}}} - \underline{\underline{\underline{\underline{X}}}}^i_{t+1}\right) \\
&+ \frac{\partial f_c}{\partial D}\Big|^i_{t+1} : \left(D - D^i_{t+1}\right) \\
&+ \frac{\partial f_c}{\partial R} : \left(R - R^i_{t+1}\right)
\end{aligned} \tag{5.34}$$

and where

$$\frac{\partial f_c}{\partial \underline{\underline{\sigma}}} = \underline{\underline{n}} \tag{5.35}$$

$$\frac{\partial f_c}{\partial \underline{\underline{X}}} = -(1-D)\underline{\underline{n}} \tag{5.36}$$

$$\frac{\partial f_c}{\partial D} = \underline{\underline{\tilde{\sigma}}} : \underline{\underline{n}} \tag{5.37}$$

The criterion has to be checked now at the time $t+1$, that means the solution for the iteration $i+1$ is defined by the equation:

$$f_{ct+1}^{\ i} + \Delta f_{ct+1}^{\ i} = 0 \tag{5.38}$$

with

$$\begin{aligned} \Delta f_{ct+1}^{\ i} &= \frac{\partial f_c}{\partial \underline{\underline{\sigma}}}|_{t+1}^{i} : \left(\underline{\underline{\sigma}}_{t+1}^{i+1} - \underline{\underline{\sigma}}_{t+1}^{i}\right) + \frac{\partial f_c}{\partial \underline{\underline{X}}}|_{t+1}^{i} : \left(\underline{\underline{X}}_{t+1}^{i+1} - \underline{\underline{X}}_{t+1}^{i}\right) \\ &+ \frac{\partial f_c}{\partial D}|_{t+1}^{i} : \left(D_{t+1}^{i+1} - D_{t+1}^{i}\right) + \frac{\partial f_c}{\partial R} : \left(R_{t+1}^{i+1} - R_{t+1}^{i}\right) \end{aligned} \tag{5.39}$$

For the return at total strain constant ($\mathrm{d}\epsilon = 0$), the constitutive law (eq. 5.17) gives:

$$\mathrm{d}\underline{\underline{\sigma}} = -\underline{\underline{\underline{\underline{E}}}}(1-D) : \left(\mathrm{d}\underline{\underline{\epsilon}}^{p} + \mathrm{d}\xi \underline{\underline{\epsilon}}^{bs}\right) - \mathrm{d}D\underline{\underline{\tilde{\sigma}}} \tag{5.40}$$

This equation and the equations 5.22-5.25 define the set of relaxation equations for stresses and state variables evolving with plasticity. They can be discretized as a function of a plastic increment δp and the variables at the iteration i of the state $t+1$:

$$Q_{t+1}^{i+1} - Q_{t+1}^{i} = \mathcal{F}(Q_{t+1}^{i})\delta p \tag{5.41}$$

Combining the equations 5.38, 5.39 and 5.41, the value of δp can be derived as a function of the variables at the iteration i of the state $t+1$.
Substitution of this value into 5.41 yields finally the updated state Q_{t+1}^{i+1}.

5.3 Sensitivity of the solution with respect to principal parameters

The influence of parameters of modelling of the plastic strain induced martensitic transformation has been evaluated from the following reference set of data (Table. 5.4). The set of 10 parameters represents typical values of parameters, obtained either in the literature [10, 49, 108] or by tests [102]. The parameters were identified by the procedure reported in [102].

E [GPa]	ν	σ_y [MPa]	C_0 [MPa]	h	β	Δv	ξ_L	p_ξ	A
206	0.3	550	750	1.8	0.45	0.05	0.8	0.02	4.2

Table 5.4: Reference set of data

5.3.1 Monotonic loading

Monotonic tensile tests have been numerically simulated. The sensitivity of the model with respect to the parameters is shown in Figs. 5.16 through 5.19.
The influence of the parameter p_ξ is shown in Fig. 5.16. Higher p_ξ leads to a forward shift of the onset of hardening. The curves may nearly be obtained from a translation with respect to the strain axis. After saturation ($\xi = \xi_L$), the slope $\frac{\mathrm{d}\sigma}{\mathrm{d}\epsilon}$ is independent of the parameter p_ξ.

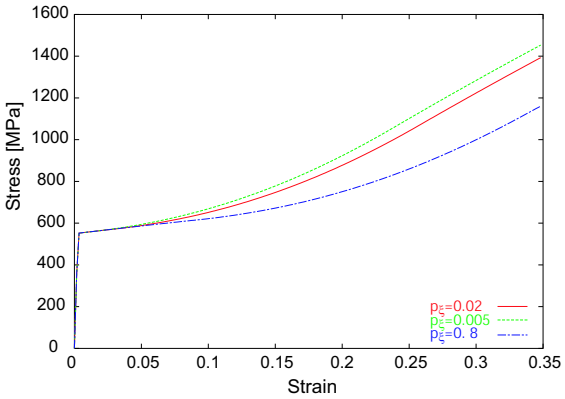

Figure 5.16: Influence of the parameter p_ξ on the tensile curve

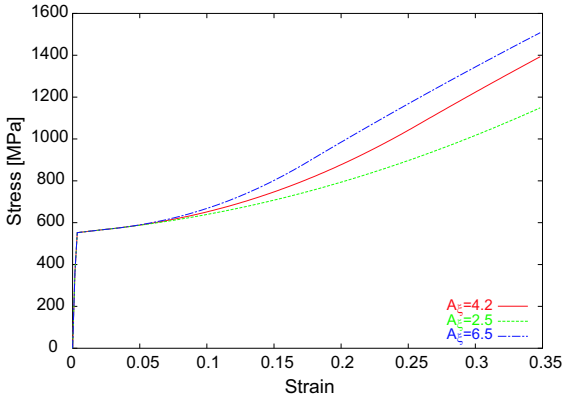

Figure 5.17: Influence of the parameter A on the tensile curve

The influence of the parameter A is shown in figure 5.17. The onset of hardening due to the phase transformation starts at the same strain level. The increasing A leads to a considerable increase of the stress level.
The influence of the parameter ξ_L is shown in Fig. 5.18. Higher ξ_L implies higher stress levels. The beginning of the curve is independent of ξ_L. The divergence occurs once ξ_L is reached. However, the applicability of the model is limited to the plastic strain not exceeding 0.2.
The influence of the parameter h is shown in figure 5.19. Again, the stress levels increase with the increasing h. Here, the divergence of the curves occurs as soon as the phase transformation initiates. After saturation ($\xi = \xi_L$), the slope $\frac{\mathrm{d}\sigma}{\mathrm{d}\epsilon}$ increases with the parameter h.
It is worth pointing out that the model has been created under the assumption of the small strains. The model is applicable for plastic strains not exceeding 0.2. For larger

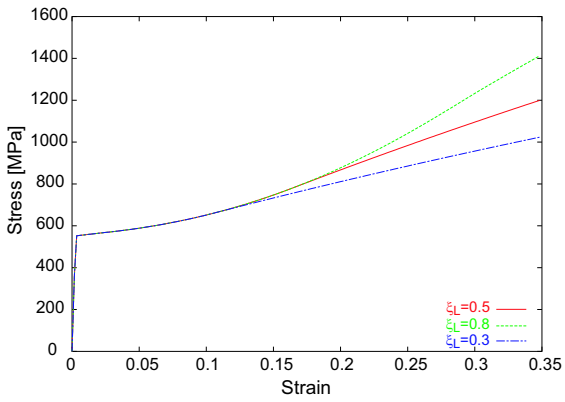

Figure 5.18: Influence of the parameter ξ_L on the tensile curve

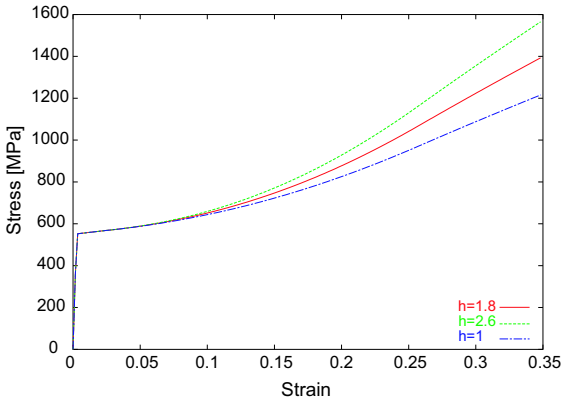

Figure 5.19: Influence of the parameter h on the tensile curve

plastic strains, the above presented curves have exclusively an indicative meaning.

5.3.2 Cyclic loading

The sensitivity of the model is analysed under uniaxial cyclic loading with a strain amplitude of ± 1 %. The stress amplitude, which is taken into account here, corresponds to the average of the extremum stresses over a cycle:

$$\sigma = \frac{|\sigma_{max}| + |\sigma_{min}|}{2} \tag{5.42}$$

The mean stress is defined by:

$$\sigma = \frac{\sigma_{max} + \sigma_{min}}{2} \tag{5.43}$$

Evolution of the stress amplitude and mean stress on cycle as a function of the number of cycles, shown in Fig. 5.20, has been obtained for the reference set of data, presented in the Table. 5.4. It is worth pointing out that the mean stress decreases when the number of cycles increases. It means that compressive stress becomes higher than tensile stress. It is mainly due to the bain strain, that occurs during martensitic transformation.
The stress amplitude is almost constant (or increases slightly) in the first 5 cycles then, it increases sharply until about 50 cycles. From that moment on the slope starts decreasing. After 100 cycles, the stress amplitude increases by more than a factor 3.
The parameters p_ξ and A affect the fatigue curves for low number of cycles (Fig. 5.21 and 5.22). The increasing A or the decreasing p_ξ lead to an increase of the stress level for the first cycles (up to 30 cycles).
The parameters ξ_L, h and β influence the fatigue curve for high number of cycles

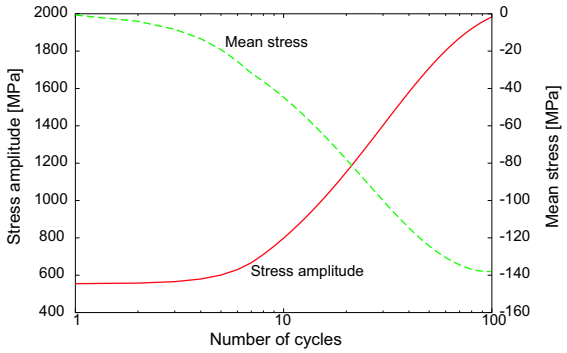

Figure 5.20: Stress amplitude and mean stress on cycle as a function of number of cycles

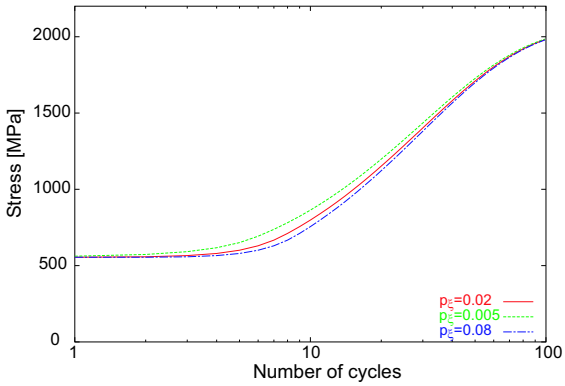

Figure 5.21: Influence of the parameter p_ξ on the stress amplitude

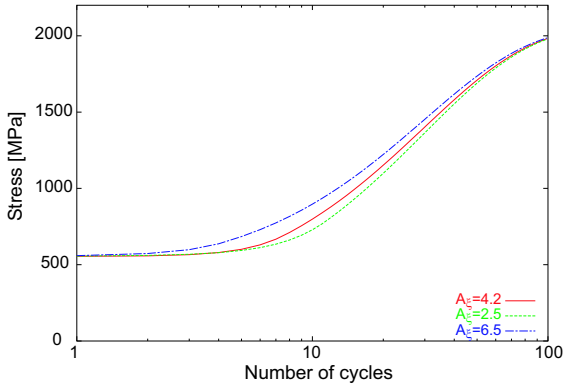

Figure 5.22: Influence of the parameter A on the stress amplitude

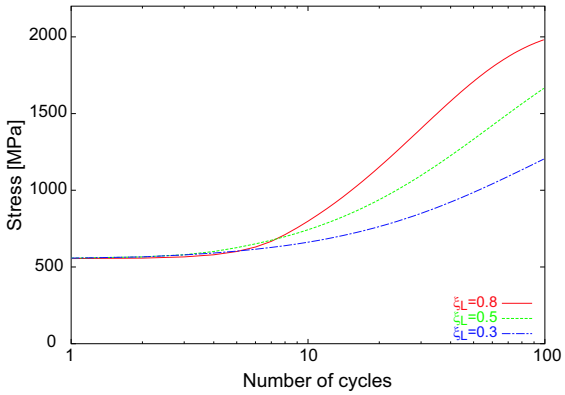

Figure 5.23: Influence of the parameter ξ_L on the stress amplitude

(> 50 cycles) (Figs. 5.23 through 5.25). The number of cycles to reach the stabilisation of the stress level depends strongly on these parameters.

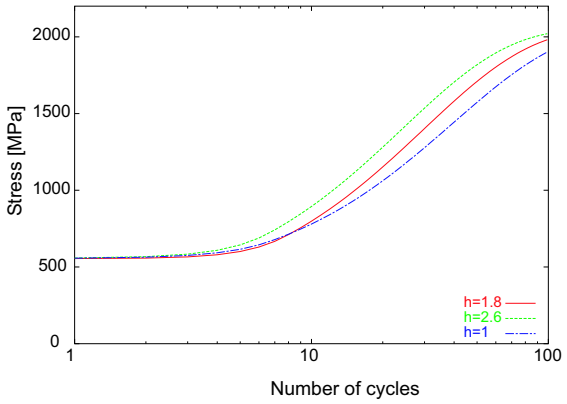

Figure 5.24: Influence of the parameter h on the stress amplitude

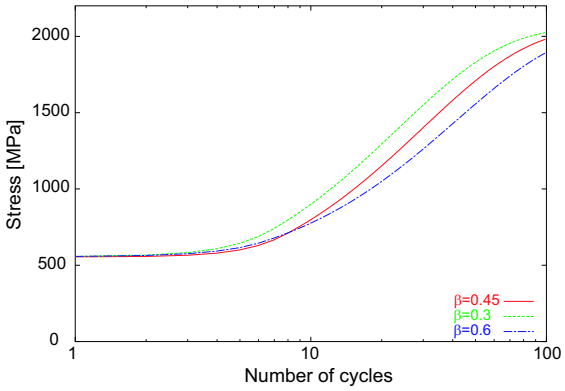

Figure 5.25: Influence of the parameter β on the stress amplitude

Chapter 6

Experimental verification of the constitutive model

6.1 Loading/unloading tests and cyclic loads at cryogenic temperatures

The bellows have been tested under loading and unloading conditions at two temperatures (room temperature and 77 K). The fatigue tests have been carried out with the set-up presented in Appendix B and a classical tensile machine has been used to perform tensile tests on bellows. This test aims at determining the global behavior of the bellows subjected to compression and tensile cycles.

6.1.1 Numerical model

Different models have been used to determine the global behavior of the bellows.

- Model 1: Axisymmetric 2D model. The model, presented in Fig. 6.1, corresponds to a half convolution meshing. The displacements at the extremities are radially free and axially blocked or imposed. The size of the model is small which allows to have a good discretization of the geometry. The elements have quadratic shape functions. The thickness of the wall can evolve along the profile of the convolution. It means that the variation of thickness due to the localisation of the plastic strain at root and crest of the convolution, during the forming process, are easily taken into account. The stress or plastic strain fields are well represented in such a model.

- Model 2: 3D shell model. This model represents a quarter of the bellows (Fig. 6.2) and it is meshed by using shell elements. The elements have several integration

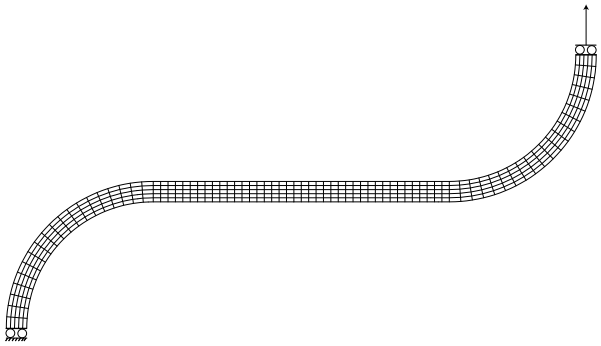

Figure 6.1: Plane axisymmetric model

points through the thickness of the shell. In case of plasticity, the generalized stresses are not overestimated. The profile of the thickness along the convolution can not be easily taken into account. Generally, uniform thickness, which corresponds to the thickness measured at the root of the convolution, is applied over the whole bellows.
Such a model can be used to determine the behavior of the bellows expansion joint under transversal offset or for the stability analysis.

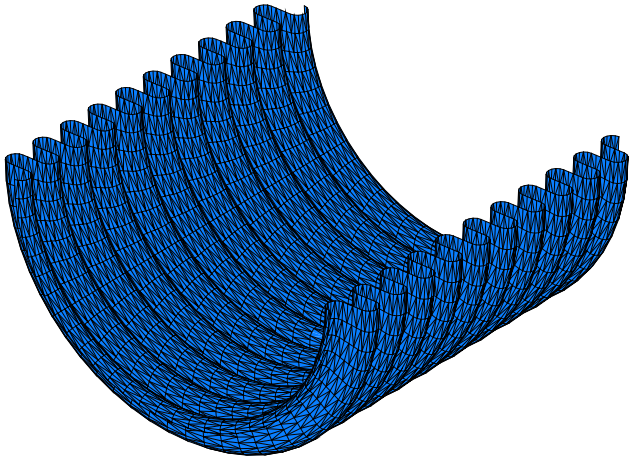

Figure 6.2: 3D shell model

A comparison of response of the models is given Fig. 6.3. The wall thickness has been fixed uniform for both models. The relative error does not exceed 7 %. It seems that the shells models are less stiff than the axisymmetric ones. Increase of the number of the integration points through the wall yields the model softer. The number of load

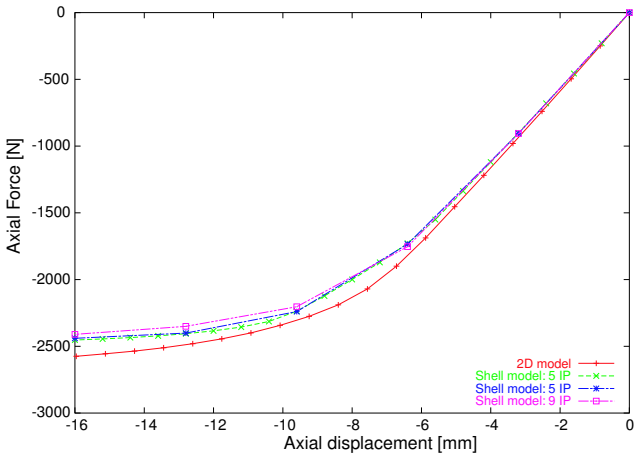

Figure 6.3: Comparison of different models

steps does not have any influence on the global behavior of the expansion joint. The application domain of each model is presented in the Table 6.1.

Model	Global behavior		State variable fields	Stability Analysis	CPU time
	Axial	Transversal			
Axisymmetric model	++	×	++	×	++
3D shell model	++	++	+	++	-

++: very well adapted +: well adapted -: not well adapted ×: irrelevant

Table 6.1: Applicability of different models

For the multi-ply bellows, the friction between the plies and the differences in geometry are not taken into account. That means that only one ply is calculated and the global forces are multiplied by the number of plies, accordingly.

6.1.2 Axial cyclic loads at cryogenic temperatures

The axial cyclic behaviour of the bellows expansion joints has been determined experimentally and numerically. An axisymmetric model has been used to simulate the axial response of the bellows. Figures 6.4 and 6.5 represent the behaviour of the short nested bellows (with 7 convolutions) at room temperature and at 77 K, respectively. The correlation of the simulation and the experiment is good. The hysteresis loops, corresponding to the energy dissipation due to plasticity, are quite narrow. The non-linear response, even in quasi-elastic regime (low plastic disspation) is well represented.

Figures 6.6 and 6.7 represent the behaviour of RF-contact bellows (beam line) at room

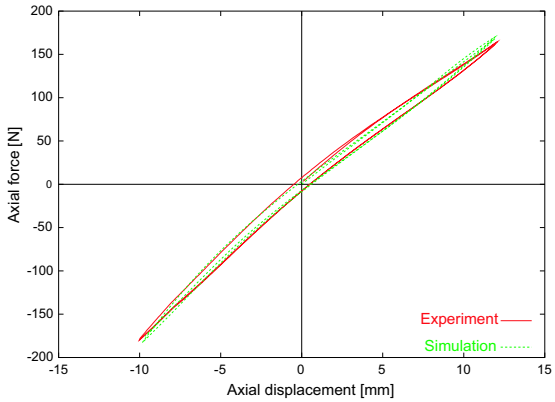

Figure 6.4: Experimental curve obtained at 293 K and numerical simulation for the short nested bellows

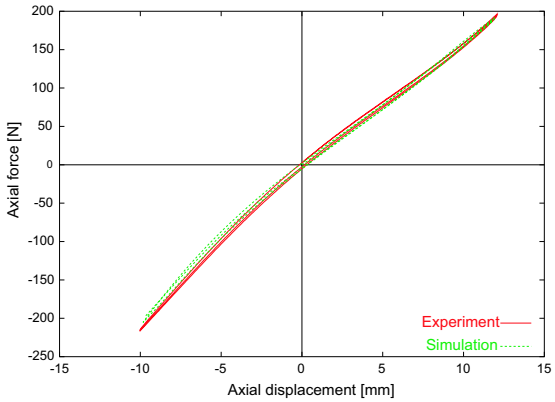

Figure 6.5: Experimental curve obtained at 77 K and numerical simulation for the short nested bellows

temperature and at 77 K, respectively. The experimental and the numerical results are similar in terms of plastic dissipation and maximum axial force in tension. The simulation gives higher absolute value of the force in compression. The relative error is about 20 %.

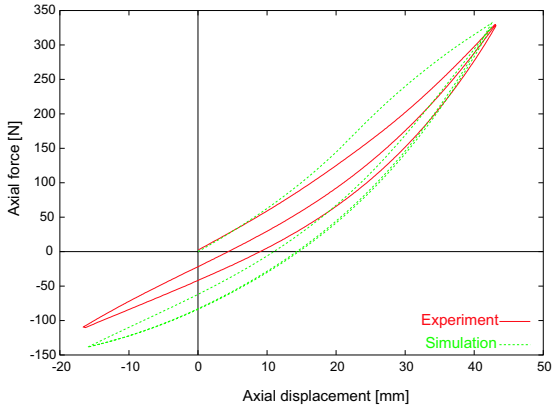

Figure 6.6: Experimental cyclic curves obtained at 293 K and numerical simulation for the RF contact bellows

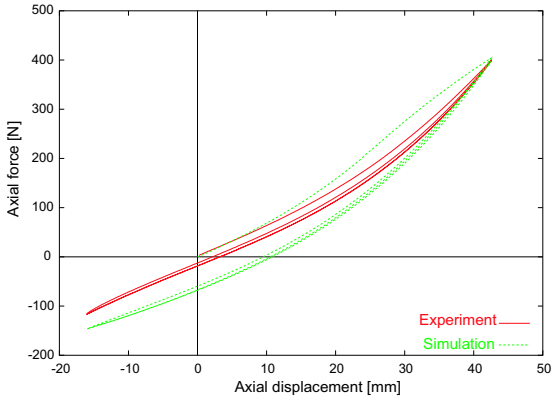

Figure 6.7: Experimental cyclic curves obtained at 77 K and numerical simulation for the RF contact bellows

Figures 6.8 and 6.9 illustrate the behaviour of the QBX bellows (heat exchanger line) at room temperature and at 77 K, respectively. This bellows is composed of two plies. The experimental and the numerical results are similar. Nevertheless, the extremum forces (both in compression and in tension) and the plastic dissipation, computed numerically, are smaller than in the experiment. The difference is higher at cold than at room temperature. The simulation gives smaller absolute values of the force in compression. The maximum relative error in terms of axial force does not exceed 15 % and

19 % at room temperature and at 77 K, respectively. This difference of behaviour is due to the interaction between the plies, which is not taken into account in the model. The local friction of the two plies induces higher forces and more dissipation.

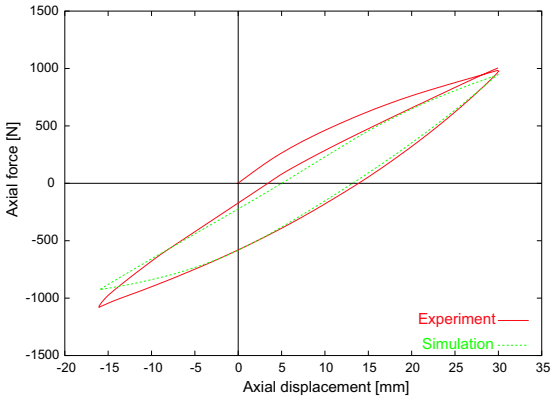

Figure 6.8: Experimental cyclic curves obtained at 293 K and numerical simulation for the QBX 2-ply bellows

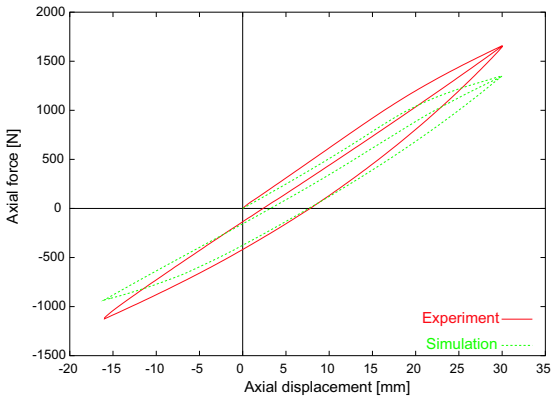

Figure 6.9: Experimental cyclic curves obtained at 77 K and numerical simulation for the QBX 2-ply bellows

6.2 $\gamma \rightarrow \alpha'$ phase transformation and evolution of ductile damage at 77 K and 4.5 K

The model UPTDAMEM has been implemented in the FE code CASTEM2000 (Section 5.2). It is applied to half-convolution of U-shaped bellows expansion joint (Fig. 4.9), subjected to axial deformation. Evolution of the plastic strain induced martensitic transformation and damage fields, along the internal and external surface and through the thickness, are presented in Figs. 6.10 through 6.13. The variables are normalized with respect the maximum value in the bellows.
The plastic strain induced damage and intensity of the martensitic transformation are maximum at root and at crest of the bellows, due to the localisation of the plastic strains (Figs. 6.10 and 6.12). The evolution of the variables through the thickness of the wall is presented in Figs. 6.11 and 6.13. It turns out that the damage and the phase transformation are very localised on the surface at root and at crest of the convolution.

6.3 Fatigue life of corrugated bellows at cryogenic temperatures

The fatigue life of the bellows expansion joints is determined by the evaluation of damage in the critical points of the convolution. The analysis is made in two points

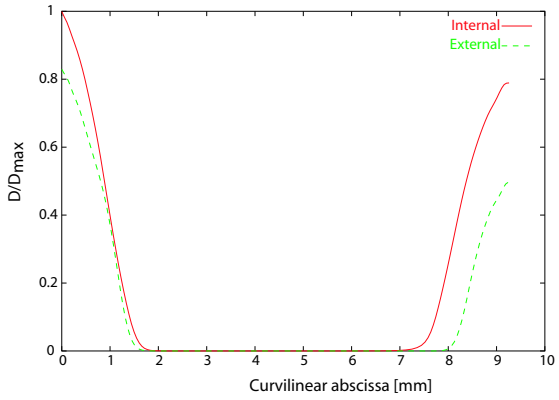

Figure 6.10: Typical damage evolution along bellows convolution

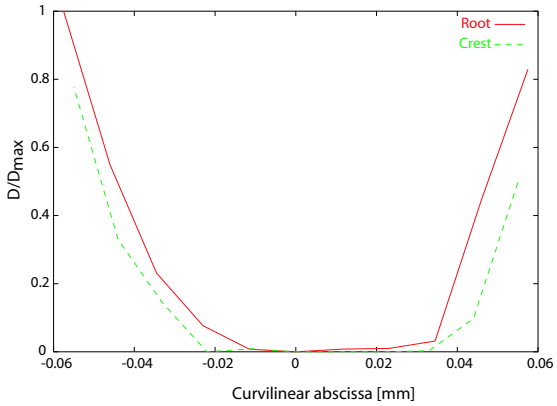

Figure 6.11: Typical damage evolution through bellows thickness

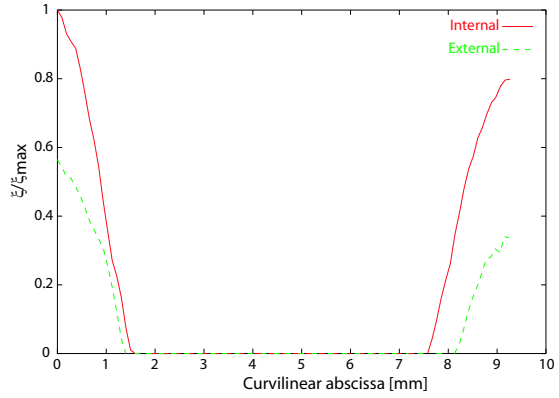

Figure 6.12: Typical intensity of plastic strain-induced phase transformation along convolution

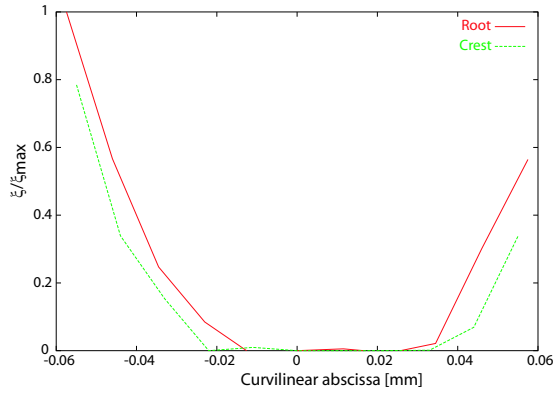

Figure 6.13: Typical intensity of plastic strain-induced phase transformation through thickness

by a post-processor, which computes the damage evolution from the evolution of the total strain tensor. The critical points are determined either by the the maximum of the Von Mises equivalent stress or by the maximum of the damage equivalent stress, σ^*_{eq}, which is defined by:

$$\sigma^*_{eq} = \sigma_{eq} R_\nu^{1/2} \tag{6.1}$$

where σ_{eq} is the Von Mises equivalent stress and R_ν is defined by:

$$R_\nu = \frac{2}{3}(1+\nu) + 3(1-2\nu)\left(\frac{\sigma_h}{\sigma_{eq}}\right)^2 \tag{6.2}$$

where σ_h denotes the hydrostatic stress.
The most intensive damage evolution occurs at the point where damage equivalent stress is the highest (due to the triaxiality ratio).

The critical point, numerically determined, corresponds to the place where the cracks are observed experimentally. For the U-shaped bellows expansion joints, the critical point is located at root of the convolution, whereas for the nested bellows, the critical point is at crest, where the local meridional curvature is the highest.
The number of cycles to failure, obtained for different critical levels of damage are compared in Tables 6.2 and Table 6.3 to the average number of cycles to failure, $\bar{N}_f$, obtained experimentaly, at room temperature and at 77 K, respectively. The bellows are subjected to internal vacuum and to axial cyclic displacement. The strokes are as follows: -16 mm/+30 mm for the heat exchanger and bus-bar bellows, -11.5 mm/+13.5 mm and -16 mm/+42.5 mm for the short nested and RF contact bellows, respectively. The average number of cycles to failure is given by:

$$\bar{N}_f = \frac{1}{n}\sum_{i}^{n} N_{f_i} \tag{6.3}$$

where n denotes the number of tests and N_{f_i} is the number of cycles to failure for test i.

	Nested bellows (7 convolutions)	RF contact bellows	Heat exchanger bellows (QBX)	Bus-bar bellows (M)
$D_{cr} = 0.4$	2418	2120	1514	209
$D_{cr} = 0.6$	2543	2361	1577	210
$D_{cr} = 0.9$	2736	2799	1678	211
$\bar{N}_f$	2778	4990	1627	429[a]

[a] Failure of the internal ply has been detected at about 230 cycles

Table 6.2: Number of cycles to failure at 293 K for different types of bellows under the above specified cyclic loads

	Nested bellows (7 convolutions)	RF contact bellows	Heat exchanger bellows (QBX)
$D_{cr} = 0.4$	shakedown	shakedown	2157
$D_{cr} = 0.6$	shakedown	shakedown	2165
$D_{cr} = 0.9$	shakedown	shakedown	2178
$\bar{N}_f$	> 14000	> 14000	2588

Table 6.3: Number of cycles to failure at 77 K for different types of bellows under the above specified cyclic loads

It turns out that the theoretical results, for low-cycle fatigue, give a conservative es-

timate of the number of cycles to failure when compared to experiments. Several phenomena can explain the difference:

- The criterion used in the numerical analysis allows to define the number of cycles to initiation of a mesocrack. The mesocrack grows from cycle to cycle until it crosses the wall. The fracture mechanics can define the additional number of cycles related to the crack propagation. Nevertheless, given the thin wall of the bellows (~ 0.15 mm), it is likely that the propagation of the crack through the wall is very fast. Fast vacuum degradation process seems to confirm this hypothesis.

- The approach is fully uncoupled. It means that it consists in neglecting the coupling between the strains and the damage. Thus, there is no redistribution of the stresses during the cyclic load.

In case of high-cycle fatigue, for example for the RF and short nested bellows at 77 K, the model is not adapted to evaluation of the number of cycles to failure. Other approaches, like two-scale model [78, 105, 109–111] have to be used. In such model, a damageable elasto-plastic inclusion embedded in the elastic matrix is considered to be the weak point of the material. The inclusion has a yield stress equal to the fatigue limit, σ_f, determined from the Woehler curves. Localisation relationship is given by the Kröner equation [96].
The effect of the free surface of the material (in contact with ambiant air) on the high-cycle fatigue has to be taken into account [112]. The surface effect (plastic deformation can develop easier) can reduce the number of cycles to failure by 10 to 40%, in case of high-cycle fatigue. The decrease of the number of cycles to failure depends on the stress state [112]. This effect is not relevant in case of low-cycle fatigue. The impact of surface effects on the fatigue life is negligible [113].

Chapter 7

Influence of damage and phase transformation on local stability of thin-walled shells at cryogenic temperatures

7.1 Introduction

Several types of instability can occur in the LHC interconnection expansion joints:

- The local buckling, for which the shell collapses locally without global change of the shape of the bellows (Figs 7.1 and 7.2). The buckling zone is of the order of the size of convolution. In case of nearly homogeneous stress and material properties in the buckling zone, this phenomenon can be described by the Axelrad equation [7]:

$$N_\theta + H^2 N_\Phi = \frac{2Et^2}{r_\Phi \sqrt{12(1-\nu^2)}}(1 + kH^2) \tag{7.1}$$

  where t denotes the wall thickness, N_θ and N_Φ are the normal circumferential and meridional forces in the mid-surface of the shell, $H = c_\theta / c_\Phi$ is the ratio between the dimensions of buckling zone and $k = r_\Phi / r_\theta$ is the ratio between the current local radii of curvature.

- The instability of bellows, for which the general shape of the bellows changes, is called semi-global buckling. Two cases can be distinguished. A pressurised bellows behaves like a flexible Euler's column, subjected to an axial stress (cf. [39, 114, 115]). The axis of the bellows is not straight after buckling. The associated mechanism of instability is called column buckling. Typical buckling mode is shown in Fig. 7.3. Bellows can show another instability mode, called in-plane

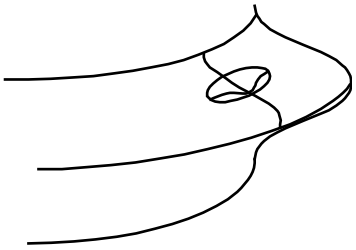

Figure 7.1: Principle of local buckling

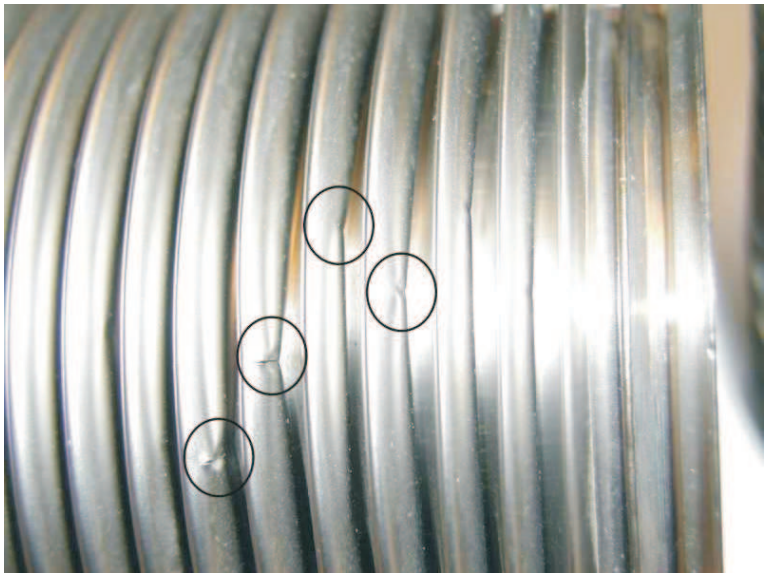

Figure 7.2: Local buckling of nested bellows (initial thickness 0.15 mm)

squirm. The axis of expansion joint is still straight but the convolutions are warped (Fig 7.4).

Figure 7.3: Column buckling of bellows

Figure 7.4: In plane squirm of nested bellows

- The global buckling of entire line, for which the set bellows and adjacent tubes loses the stability. Similary to the column instability of bellows, the system com-

posed of the tubes and a bellows under pressure, behaves similarly to the Euler column. Stability depends on boundary conditions [39, 116, 117]. Principle and example of global buckling of an interconnection line are given Fig. 7.5 and 7.6.

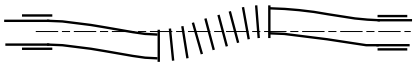

Figure 7.5: Principle of global buckling of an interconnection line

Figure 7.6: Global buckling of an interconnection line

The stability is related to the stiffness of bellows, that depends on the material properties. Generally, the properties evolve during the lifetime of the component (damage, phase transformation) and this effect can lead to the instability after a certain time of operation. The section 7.4 is dedicated to the effect of the evolution of material properties on stability.

7.2 Mechanism of structural instability

Theoretic definition of stability of structure is defined mathematically [118] but resumes to the following statement: *a struture (or a system) is stable if a small change in the initial conditions (input) leads to a small change in the solution (output, response)* [119].
Stability of structure can be determined by energy methods. According to the theorem of Lagrange-Dirichlet [120], a system is stable if the potential energy has a strict minimum.
A stucture is considered in different states:

- The initial state, Ω_0.

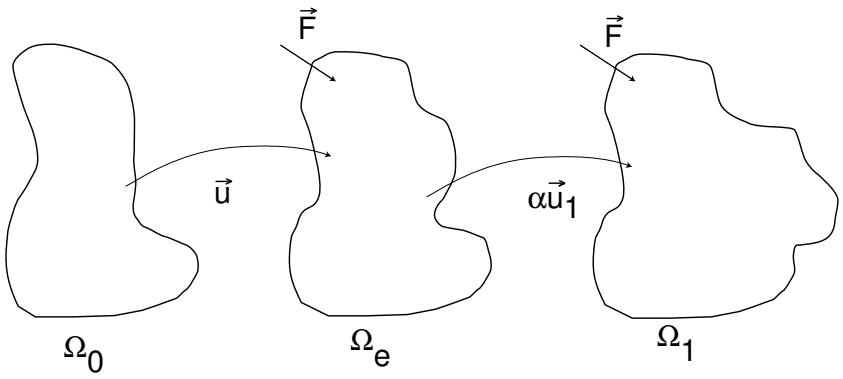

Figure 7.7: Structure in different states

- The equilibrum state, Ω_e.
- The equilibrum state after a perturbation, Ω_1.

For the state of equilibrum Ω_e,

$$\underline{\underline{\epsilon}}\left(\vec{u}\right) = \frac{1}{2}\left(\underline{\underline{\underline{\underline{\text{grad}}}}}^T \vec{u} + \underline{\underline{\underline{\underline{\text{grad}}}}}\vec{u} + \underline{\underline{\underline{\underline{\text{grad}}}}}^T \vec{u}\ \underline{\underline{\underline{\underline{\text{grad}}}}}\vec{u}\right) \tag{7.2}$$

$$\underline{\underline{\epsilon}}\left(\vec{u}\right) = \underline{\underline{\epsilon}}^L\left(\vec{u}\right) + \underline{\underline{\epsilon}}^Q\left(\vec{u}\right) \tag{7.3}$$

with

$$\begin{aligned} \underline{\underline{\epsilon}}^L\left(\vec{u}\right) &= \frac{1}{2}\left(\underline{\underline{\underline{\underline{\text{grad}}}}}^T \vec{u} + \underline{\underline{\underline{\underline{\text{grad}}}}}\vec{u}\right) \\ \underline{\underline{\epsilon}}^Q\left(\vec{u}\right) &= \frac{1}{2}\left(\underline{\underline{\underline{\underline{\text{grad}}}}}^T \vec{u}\ \underline{\underline{\underline{\underline{\text{grad}}}}}\vec{u}\right) \end{aligned}$$

where $\underline{\underline{\epsilon}}^L\left(\vec{u}\right)$ denotes the linear part of the strain and $\underline{\underline{\epsilon}}^Q\left(\vec{u}\right)$ denotes the non-linear parts of the strain.
The energy of elastic deformation of the structure for this state is given by the following relationship:

$$E_d^e = \frac{1}{2}\int_\Omega \underline{\underline{\sigma}} : \underline{\underline{\epsilon}} \mathrm{d}\Omega \tag{7.4}$$

The potential energy is given by:

$$E_p^e = E_d^e - \vec{F}^T\ \vec{u} \tag{7.5}$$

where $\vec{F}$ corresponds to the equivalent (in terms of energy) force vector.
A perturbation of the form $\vec{u}_1$ is applied to the structure in the equilibrum state Ω_e:

$$\vec{u}_{tot} = \vec{u} + \alpha\vec{u}_1 \tag{7.6}$$

By linearity, the corresponding linear strain field is given by:

$$\underline{\underline{\epsilon}}^{L}\left(\vec{u}_{tot}\right) = \underline{\underline{\epsilon}}^{L}\left(\vec{u}\right) + \alpha\underline{\underline{\epsilon}}^{L}\left(\vec{u}_1\right) \tag{7.7}$$

The non linear term is given by:

$$\underline{\underline{\epsilon}}^{Q}\left(\vec{u}_{tot}\right) = \underline{\underline{\epsilon}}^{Q}\left(\vec{u}\right) + \alpha^2\underline{\underline{\epsilon}}^{Q}\left(\vec{u}_1\right) + \alpha\underline{\underline{\epsilon}}^{Q}\left(\vec{u},\vec{u}_1\right) + \alpha\underline{\underline{\epsilon}}^{Q}\left(\vec{u}_1,\vec{u}\right) \tag{7.8}$$

The strain field for the state 1 can be expressed under the form:

$$\underline{\underline{\epsilon}}\left(\vec{u}_1\right) = \underline{\underline{\epsilon}}_0 + \alpha\ \underline{\underline{\epsilon}}_1 + \alpha^2\ \underline{\underline{\epsilon}}_2 \tag{7.9}$$

with

$$\begin{aligned}
\underline{\underline{\epsilon}}_0 &= \underline{\underline{\epsilon}}^{L}\left(\vec{u}\right) + \underline{\underline{\epsilon}}^{Q}\left(\vec{u}\right)\\
\underline{\underline{\epsilon}}_1 &= \underline{\underline{\epsilon}}^{L}\left(\vec{u}_1\right) + \underline{\underline{\epsilon}}^{Q}\left(\vec{u},\vec{u}_1\right) + \underline{\underline{\epsilon}}^{Q}\left(\vec{u}_1,\vec{u}\right)\\
\underline{\underline{\epsilon}}_2 &= \underline{\underline{\epsilon}}^{Q}\left(\vec{u}_1\right)
\end{aligned}$$

The energy of the state 1 is given by:

$$E^{e}_{d_1} = \frac{1}{2}\int_{\Omega_1} \underline{\underline{\underline{\underline{\sigma}}}} : \underline{\underline{\epsilon}}\ \mathrm{d}\Omega_1 \tag{7.10}$$

$$E^{e}_{d_1} = \frac{1}{2}\int_{\Omega_1} \left(\underline{\underline{\epsilon}}_0 + \alpha\ \underline{\underline{\epsilon}}_1 + \alpha^2\underline{\underline{\epsilon}}_2\right) : \underline{\underline{\underline{\underline{E}}}} : \left(\underline{\underline{\epsilon}}_0 + \alpha\ \underline{\underline{\epsilon}}_1 + \alpha^2\ \underline{\underline{\epsilon}}_2\right)\ \mathrm{d}\Omega_1 \tag{7.11}$$

with $\underline{\underline{\underline{\underline{E}}}}$ being the stiffness tensor. The energy can be decomposed as follows:

$$E^{e}_{d_1} = W_0 + \alpha W_1 + \alpha^2 W_2 + \alpha^3 W_3 + \alpha^4 W_4 \tag{7.12}$$

where

$$\begin{aligned}
W_0 &= \frac{1}{2}\int_{\Omega_1} \underline{\underline{\epsilon}}_0 : \underline{\underline{\underline{\underline{E}}}} : \underline{\underline{\epsilon}}_0\ \mathrm{d}\Omega_1\\
W_1 &= \int_{\Omega_1} \underline{\underline{\epsilon}}_1 : \underline{\underline{\underline{\underline{E}}}} : \underline{\underline{\epsilon}}_0\ \mathrm{d}\Omega_1\\
W_2 &= \frac{1}{2}\int_{\Omega_1} \underline{\underline{\epsilon}}_1 : \underline{\underline{\underline{\underline{E}}}} : \underline{\underline{\epsilon}}_1\ \mathrm{d}\Omega_1 + \int_{\Omega_1} \underline{\underline{\epsilon}}_0 : \underline{\underline{\underline{\underline{E}}}} : \underline{\underline{\epsilon}}_2\ \mathrm{d}\Omega_1\\
W_3 &= \int_{\Omega_1} \underline{\underline{\epsilon}}_1 : \underline{\underline{\underline{\underline{E}}}} : \underline{\underline{\epsilon}}_2\ \mathrm{d}\Omega_1\\
W_4 &= \frac{1}{2}\int_{\Omega_1} \underline{\underline{\epsilon}}_2 : \underline{\underline{\underline{\underline{E}}}} : \underline{\underline{\epsilon}}_2\ \mathrm{d}\Omega_1
\end{aligned}$$

The potential energy in the state with imposed perturbation is given by:

$$E^e_{p_1} = E^e_{d_1} - \vec{F}^T \ \vec{u}_1 \tag{7.13}$$

The difference of potential energy between the two states is given by:

$$\Delta E_p = E^e_{p_1} - E^e_p \tag{7.14}$$

After some rearrangements one obtains:

$$\Delta E_p = \alpha \left(W_1 - \vec{F}^T \vec{u}_1 \right) + \alpha^2 W_2 + \mathrm{O}(\alpha^2) \tag{7.15}$$

Assuming small strains, the first term of the equation 7.15 reads:

$$W_1 - \vec{F}^T \vec{u}_1 = \int_\Omega \underbrace{\underline{\underline{\underline{\underline{E}}}} : \underline{\underline{\epsilon}}_0}_{\underline{\underline{\sigma_0}}} : \epsilon_1 \ \mathrm{d}\Omega - \vec{F}^T \vec{u}_1 \tag{7.16}$$

By application of the virtual power principle at the equilibrium state (point of stationarity of the potential energy), with the virtual displacement equal to $\vec{u}_1$, this term is equal to 0.
The variation of the potential energy ΔE_p is given by:

$$\Delta E_p = \alpha^2 W_2 + \mathrm{O}(\alpha^2) \tag{7.17}$$

which has the sign of W_2. So the stability of the equilibrium is defined by:

- If $W_2 < 0$, the equilibrum is unstable.
- If $W_2 > 0$, the equilibrum is stable.

Under the assumption of small strains, the term W_2 reads:

$$W_2 = \frac{1}{2} \int_\Omega \underline{\underline{\epsilon}}^L(\vec{u}_1) : \underline{\underline{\underline{\underline{E}}}} : \underline{\underline{\epsilon}}^L(\vec{u}_1) \ \mathrm{d}\Omega + \int_\Omega \underline{\underline{\sigma}} : \underline{\underline{\epsilon}}^Q(\vec{u}_1) \ \mathrm{d}\Omega \tag{7.18}$$

7.3 General equations of theory of thin shells

In the theory of thin sheels (Fig. 7.8), the following geometrical objects and variables are defined:

- The mid-surface of the shell,
- The normal to the mid-surface $\vec{n}$,

- The current point M is defined by $\vec{M} = \vec{m} + z\vec{n}$ where m is the point on the mid-surface and z is the coordinate aligned with respect to the normal $\vec{n}$

Generally, motion of the points in the shell is refered to the mid-surface of the shell. In the shell theory, the stress tensor is assumed to satisfy the following assumption:

$$\underline{\underline{\sigma}}\vec{n} = \vec{0} \tag{7.19}$$

It means that the stress tensor has the form:

$$\left(\begin{array}{cc|c} & \hat{\underline{\underline{\sigma}}} & \begin{matrix}0\\0\end{matrix} \\ \hline 0 & 0 & 0 \end{array}\right)_{(-,-,\vec{n})}$$

It can be represented only by the in-plane part $\hat{\underline{\underline{\sigma}}}$.
In the shell theory, the assumption for the displacement is the following:

$$\vec{u}(\vec{M}) = \underbrace{\vec{V}(\vec{m})}_{\text{in the tangent plane}} + w(\vec{m})\vec{n} + \vec{\Omega}(\vec{m}) \wedge z\vec{n} \tag{7.20}$$

where $\vec{V}$ denotes the tangent displacement to the mid-surface, $\vec{\Omega}$ stands for the rotation vector and the symbol "$\wedge$" means vectorial product. Here also $\vec{\Omega}.\vec{n} = 0$.
Considering the Kirchhoff-Love hypothesis (normal to the mid-surface remains normal after deformation), $\vec{\Omega}$ reads:

$$\vec{\Omega} = -\vec{n} \wedge \overrightarrow{\text{grad}}\,(w(\vec{m})) \tag{7.21}$$

The equation 7.20 becomes:

$$\vec{u}(\vec{M}) = \underbrace{\vec{V}(\vec{m})}_{\text{in the tangent plane}} + w(\vec{m})\vec{n} - z\overrightarrow{\text{grad}}\,(w(\vec{m})) \tag{7.22}$$

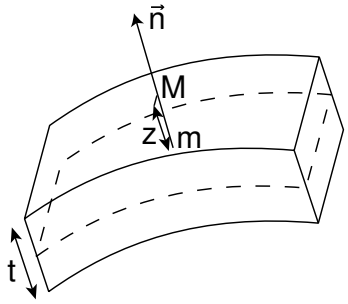

Figure 7.8: Thin-walled shell

From this displacement field, the strain field can be determined. The in-plane part of the strain is considered $\underline{\underline{\hat{\epsilon}}}$.
The constitutive equation for elastic material reads:

$$\underline{\underline{\hat{\sigma}}} = \frac{E}{1-\nu^2}\left(\nu Tr\left[\underline{\underline{\hat{\epsilon}}}\right] \mathrm{I}_2 + (1-\nu)\underline{\underline{\hat{\epsilon}}}\right) = \underline{\underline{\underline{\underline{E_{ps}}}}} : \underline{\underline{\hat{\epsilon}}} \tag{7.23}$$

where E and ν denote the Young modulus and the Poison coefficient, respectively. I_2 is the second order identity matrix.
The perturbation displacement $\vec{u}_1$ is introduced under the following form:

$$\vec{u}_1 = w\vec{n} - z\overrightarrow{\mathrm{grad}}\ w \tag{7.24}$$

with $\frac{\partial w}{\partial z} = 0$ (Love-Kirchhoff hypothesis). Hence, one obtains:

$$\underline{\underline{\mathrm{grad}}}(\vec{u}_1) = \vec{n} \otimes \overrightarrow{\mathrm{grad}}w - \overrightarrow{\mathrm{grad}}w \otimes \vec{n} - z\underline{\underline{\mathrm{grad}}}(\overrightarrow{\mathrm{grad}}w) \tag{7.25}$$

Thus, the linear strain is expressed as follows:

$$\epsilon^L(\vec{u}_1) = -z\underline{\underline{\mathrm{grad}}}(\overrightarrow{\mathrm{grad}}w) \tag{7.26}$$

From the equation 7.25, one obtains:

$$\begin{aligned}
\underline{\underline{\mathrm{grad}}}^T(\vec{u}_1)\underline{\underline{\mathrm{grad}}}(\vec{u}_1) \;=\; & \overrightarrow{\mathrm{grad}}w \otimes \overrightarrow{\mathrm{grad}}w + \vec{n} \otimes \vec{n}\ \overrightarrow{\mathrm{grad}}w.\overrightarrow{\mathrm{grad}}w \\
& + z\left[\underline{\underline{\mathrm{grad}}}\left(\overrightarrow{\mathrm{grad}}w\right)\ \overrightarrow{\mathrm{grad}}w\right] \otimes \vec{n} \\
& + z^2\left(\underline{\underline{\mathrm{grad}}}\left(\overrightarrow{\mathrm{grad}}w\right)\right)\left(\underline{\underline{\mathrm{grad}}}\left(\overrightarrow{\mathrm{grad}}w\right)\right)
\end{aligned} \tag{7.27}$$

The rough estimates of different terms of the equation 7.27 are as follows:

$$\begin{aligned}
\overrightarrow{\mathrm{grad}}w \otimes \overrightarrow{\mathrm{grad}}w &\propto \left(\frac{1}{\mathrm{L}}\right)^2 \\
\vec{n} \otimes \vec{n}\ \overrightarrow{\mathrm{grad}}w.\overrightarrow{\mathrm{grad}}w &\propto \left(\frac{1}{\mathrm{L}}\right)^2 \\
z\left[\underline{\underline{\mathrm{grad}}}\left(\overrightarrow{\mathrm{grad}}w\right)\ \overrightarrow{\mathrm{grad}}w\right] \otimes \vec{n} &\propto \frac{\mathrm{t}}{\mathrm{L}}\left(\frac{1}{\mathrm{L}}\right)^2 \\
z^2\left(\underline{\underline{\mathrm{grad}}}\left(\overrightarrow{\mathrm{grad}}w\right)\right)\left(\underline{\underline{\mathrm{grad}}}\left(\overrightarrow{\mathrm{grad}}w\right)\right) &\propto \left(\frac{\mathrm{t}}{\mathrm{L}}\right)^2\left(\frac{1}{\mathrm{L}}\right)^2
\end{aligned} \tag{7.28}$$

where L is a typical size of the shell. So $t \ll L$.
Under the assumption that the term $\left(\frac{\mathrm{t}}{\mathrm{L}}\right)^2$ is negligible with respect to the others, the

equation 7.27 reduces to:

$$\begin{aligned}\underline{\underline{\underline{\underline{\mathrm{grad}}}}}^T(\vec{u}_1)\underline{\underline{\underline{\underline{\mathrm{grad}}}}}(\vec{u}_1) &= \overrightarrow{\mathrm{grad}}w \otimes \overrightarrow{\mathrm{grad}}w + \vec{n} \otimes \vec{n}\ \overrightarrow{\mathrm{grad}}w.\overrightarrow{\mathrm{grad}}w \\ &\quad + z\left[\underline{\underline{\underline{\underline{\mathrm{grad}}}}}\left(\overrightarrow{\mathrm{grad}}w\right)\ \overrightarrow{\mathrm{grad}}w\right] \otimes \vec{n} \end{aligned} \tag{7.29}$$

and leads to:

$$\begin{aligned}2\underline{\underline{\epsilon}}^Q(\vec{u}_1) &= \overrightarrow{\mathrm{grad}}w \otimes \overrightarrow{\mathrm{grad}}w + \vec{n} \otimes \vec{n}\ \overrightarrow{\mathrm{grad}}w.\overrightarrow{\mathrm{grad}}w \\ &\quad + z\left[\underline{\underline{\underline{\underline{\mathrm{grad}}}}}\left(\overrightarrow{\mathrm{grad}}w\right)\ \overrightarrow{\mathrm{grad}}w\right] \otimes \vec{n} \end{aligned} \tag{7.30}$$

The instability of the shell is given by the sign of W_2. Let us calculate the nonlinear term of W_2 given by:

$$W_2^Q = \int_\Omega \underline{\underline{\sigma}} : \underline{\underline{\epsilon}}^Q(\vec{u}_1)\ \mathrm{d}\Omega \tag{7.31}$$

whereas the following conditions are satisfied:

$$\underline{\underline{\sigma}} : \left[\left[\underline{\underline{\underline{\underline{\mathrm{grad}}}}}\left(\overrightarrow{\mathrm{grad}}w\right)\ \overrightarrow{\mathrm{grad}}w\right] \otimes \vec{n}\right] = 0 \tag{7.32}$$

$$\underline{\underline{\sigma}} : [\vec{n} \otimes \vec{n}] = 0 \tag{7.33}$$

From the equations (7.32, 7.33), the equation (7.31) becomes:

$$\int_\Omega \underline{\underline{\sigma}} : \underline{\underline{\epsilon}}^Q(\vec{u}_1)\ \mathrm{d}\Omega = \frac{1}{2}\int_\Omega \underline{\underline{\sigma}} : \left(\overrightarrow{\mathrm{grad}}w \otimes \overrightarrow{\mathrm{grad}}w\right)\ \mathrm{d}\Omega \tag{7.34}$$

Let us calculate the second term of W_2 given by:

$$W_2^L = \frac{1}{2}\int_\Omega \underline{\underline{\epsilon}}^L(\vec{u}_1) : \underline{\underline{\underline{\underline{E_{ps}}}}} : \underline{\underline{\epsilon}}^L(\vec{u}_1)\ \mathrm{d}\Omega \tag{7.35}$$

with

$$\underline{\underline{\epsilon}}^L(\vec{u}_1) = -z\underline{\underline{\underline{\underline{\mathrm{grad}}}}}(\overrightarrow{\mathrm{grad}}w) \tag{7.36}$$

The equation 7.35 becomes:

$$W_2^L = \frac{1}{2}\int_S \underline{\underline{\underline{\underline{\mathrm{grad}}}}}(\overrightarrow{\mathrm{grad}}w) : \int_{-\frac{t}{2}}^{\frac{t}{2}} z^2 \underline{\underline{\underline{\underline{E_{ps}}}}}\ \mathrm{d}z\ : \underline{\underline{\underline{\underline{\mathrm{grad}}}}}(\overrightarrow{\mathrm{grad}}w)\ \mathrm{d}S \tag{7.37}$$

where S denotes the mid-surface of the shell.
In case of material and geometrical symmetry:

$$\int_{-\frac{t}{2}}^{\frac{t}{2}} z^2 \underline{\underline{\underline{\underline{E_{ps}}}}}\ \mathrm{d}z = 2\int_0^{\frac{t}{2}} z^2 \underline{\underline{\underline{\underline{E_{ps}}}}}\ \mathrm{d}z \tag{7.38}$$

which is a term depending only on material properties and geometry. In case of plasticity and under certain assumptions, the elastic stiffness tensor can be replaced by the tangent modulus.
Finally, the instability condition is expressed by:

$$\frac{1}{2}\int_{\Omega}\underline{\underline{\sigma}} : \left(\overrightarrow{\text{grad}}w \otimes \overrightarrow{\text{grad}}w\right) \text{d}\Omega + \int_{S}\underline{\underline{\underline{\underline{\text{grad}}}}}(\overrightarrow{\text{grad}}w) : \int_{0}^{\frac{t}{2}} z^2 \underline{\underline{\underline{\underline{E_{ps}}}}}\ \text{d}z : \underline{\underline{\underline{\underline{\text{grad}}}}}(\overrightarrow{\text{grad}}w)\text{d}S = 0 \tag{7.39}$$

Considering the generalized stress for the shell, defined by:

$$\underline{\underline{N}} = \int_{-\frac{t}{2}}^{\frac{t}{2}} \underline{\underline{\sigma}}\text{d}z \tag{7.40}$$

the equation 7.39 reads:

$$\frac{1}{2}\int_{S}\underline{\underline{N}} : \left(\overrightarrow{\text{grad}}w \otimes \overrightarrow{\text{grad}}w\right) \text{d}S + \int_{S}\underline{\underline{\underline{\underline{\text{grad}}}}}(\overrightarrow{\text{grad}}w) : \int_{0}^{\frac{t}{2}} z^2 \underline{\underline{\underline{\underline{E_{ps}}}}}\ \text{d}z : \underline{\underline{\underline{\underline{\text{grad}}}}}(\overrightarrow{\text{grad}}w)\text{d}S = 0 \tag{7.41}$$

A single load parameter is introduced λ, that satisfies the equation:

$$\underline{\underline{N}} = \lambda \underline{\underline{N}}_0 \tag{7.42}$$

The associated Rayleigh coefficient is given by [121]:

$$\lambda = \frac{\int_S \underline{\underline{\underline{\underline{\text{grad}}}}}(\overrightarrow{\text{grad}}w) : \int_0^{\frac{t}{2}} z^2 \underline{\underline{\underline{\underline{E_{ps}}}}}\ \text{d}z : \underline{\underline{\underline{\underline{\text{grad}}}}}(\overrightarrow{\text{grad}}w)\text{d}S}{\frac{1}{2}\int_S \underline{\underline{N}}_0 : \left(\overrightarrow{\text{grad}}w \otimes \overrightarrow{\text{grad}}w\right) \text{d}S} \tag{7.43}$$

Let us consider w, kinematically admissible, under the form:

$$w = \sum_{i=1}^{n} q_n w_q \tag{7.44}$$

The Rayleigh coefficient reads:

$$\lambda = \frac{\vec{q}^T \underline{\underline{A}} \vec{q}}{\vec{q}^T \underline{\underline{B}} \vec{q}} \tag{7.45}$$

with

$$\vec{q} = \begin{pmatrix} q_1 \\ \vdots \\ q_n \end{pmatrix} \tag{7.46}$$

$$Aij = \int_S \underline{\underline{\underline{\underline{\text{grad}}}}}(\overrightarrow{\text{grad}}w_i) : \int_0^{\frac{t}{2}} z^2 \underline{\underline{\underline{\underline{E_{ps}}}}}\ \text{d}z : \underline{\underline{\underline{\underline{\text{grad}}}}}(\overrightarrow{\text{grad}}w_j)\text{d}S \tag{7.47}$$

$$B_{ij} = \frac{1}{2}\int_S \underline{\underline{N}}_0 : \left(\overrightarrow{\text{grad}}w_i \otimes \overrightarrow{\text{grad}}w_j\right) \text{d}S \tag{7.48}$$

The critical value of the loading parameter is the minimum of the Rayleigh coefficient:

$$\frac{\partial \lambda}{\partial \vec{q}} = 0 \tag{7.49}$$

which leads to:

$$\det[\underline{\underline{A}} - \lambda \underline{\underline{B}}] = 0 \tag{7.50}$$

The critical loading parameter is obtained from an eigenvalue problem and it corresponds to the minimum of the eigenvalues:

$$\lambda_{cr} = \min\{\lambda_1, \lambda_2, \ldots, \lambda_n\} \tag{7.51}$$

7.4 Effect of evolution of material properties on local stability of shells

The previous theory has been developed for elastic structures. The material properties play a role in the following term:

$$\underline{\underline{\underline{\underline{A}}}} = \int_{-\frac{t}{2}}^{\frac{t}{2}} z^2 \underline{\underline{\underline{\underline{E_{ps}}}}} \, \mathrm{d}z \tag{7.52}$$

Damage can occur during the lifetime of the structure. To take into account the evolution of damage, first the elastic modulus affected by damage is considered.

$$\left\{ \begin{array}{ccc} E(z) & \leftarrow & E(1 - D(z)) \\ \underline{\underline{\underline{\underline{E_{ps}}}}} & \leftarrow & \underline{\underline{\underline{\underline{\tilde{E}_{ps}}}}} \end{array} \right.$$

The damaged material below the yield point can be considered elastic and the classical stability theory can be applied.
Stability theory is based on searching the equilibrium infinitely close to the point of bifurcation. In the plasticity domain, the material behavior can be modelled by the tangent stiffness tensor, defined from the tangent modulus in case of an active plastic process.

$$\left\{ \begin{array}{ccc} E & \leftarrow & E^t \\ \underline{\underline{\underline{\underline{E_{ps}}}}} & \leftarrow & \underline{\underline{\underline{\underline{E^t_{ps}}}}} \end{array} \right.$$

At points where plastic process is active at equilibrium, a strain increment induces either an elastic unloading or a plastic loading. Application to elastic-plastic column has been developed by Shanley [122] (bilinear material) and shows the influence of plastic zone during bifurcation process. Generally, description of a plastic structure is

more complex [123], since often there is no unique solution to the problem (Karman and Shanley bifurcation loads)
Here, for bellows expansion joints, the plastic zone is very localised on the surface at root and at crest (plastic hinges) (Fig. 7.9). So during the bifurcation process,

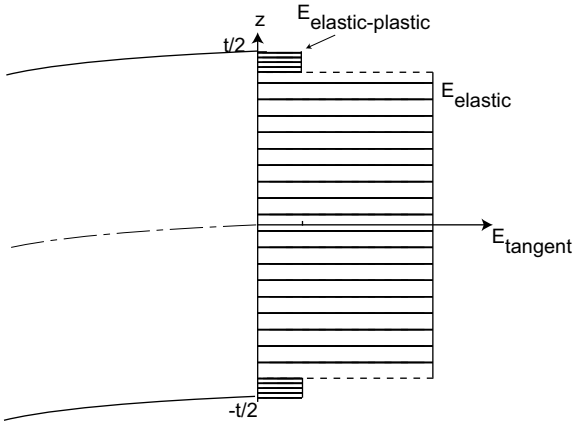

Figure 7.9: Typical profile of the tangent modulus through thickness at root and at crest ot the convolution

the increment of plastic energy is negligible with respect to the elastic energy of the bellows. It allows to treat the bellows expansion joint as a pseudo-elastic structure with a tangent modulus for the plastic zone. The assumption that there is no redistribution of the elastic-plastic zones during buckling is made. Finally, for an elastic-plastic damageable structure the term A is replaced by:

$$\underline{\underline{A}} = \int_{-\frac{t}{2}}^{\frac{t}{2}} z^2 \underline{\underline{E^t_{ps}}}(1 - D(z))\ \mathrm{d}z \tag{7.53}$$

To define the evolution of the damage parameter D as a function of the number of cycles, the following main assumptions are made [39]:

- Kinetic law of damage evolution is defined by Eq. 4.13, with $s = 1$
- Description of the hysteresis is based on the Ramberg-Osgood model [124]
- Variation of the damage parameter over a cycle is neglected
- Plastic strain range, $\Delta\epsilon_p$ is constant on cycle (stabilized hysteresis)

The damage parameter is computed from the relationship [39]:

$$D = N \left(\frac{A^2}{4ES} \beta \Delta\epsilon_p^{\frac{1}{\beta}} \right) H(N - N_D) \tag{7.54}$$

where E denotes the Young modulus, S is the energy strength of damage, A and β represent two material parameters. The parameter N_D stands for the damage threshold (equivalent of p_D) expressed in terms of number of cycles.
The components are subjected to cryogenic temperatures in normal service conditions. Thus, creep buckling, as defined in [125], can be neglected and is not treated.

Influence of the material properties on the local buckling of bellows expansion joints

Local stability of U shaped bellows is analysed taking into account the evolution of the material properties. The expansion joint with a free length L_0 is subjected to a symmetric axial displacement $\pm\Delta$. The bellows is simultaneously subjected to the outer pressure. The buckling pressure is calculated over the entire cycle. 3D modelling leads to a very long calculation time. Thus, the bellows is modelled by shell elements with several integration points across the thickness. The thickness is considered uniform in the whole struture. There exist sheel elements in the software INCA, developed for 2D axisymmetric analysis [126], that are capable of describing the kinetics of a shell subjected to non-axisymmetric loads and with initial geometrical imperfections around the circumference by means of Fourier series [127]. The influence of circumferential thickness variation on the buckling has been studied for cylindrical shells under external pressure [128, 129]. It turns out that short shells ($Z < 20$) are not sensitive with respect to such imperfections. Here, Z stands for the Batdorf parameter, defined by:

$$Z = \sqrt{1-\nu^2}\left(\frac{L}{R}\right)^2 \frac{R}{t} \tag{7.55}$$

An equivalent pseudo-elastic stiffness tensor is calculated from the equation 7.53:

$$\underline{\underline{\underline{\underline{E_{eq}}}}} = \frac{12}{t^3}\int_{-\frac{t}{2}}^{\frac{t}{2}} z^2 \underline{\underline{\underline{\underline{E^t_{ps}}}}}(1-D)\,\mathrm{d}z \tag{7.56}$$

This term is calculated by integration based on the trapeze method. Elastic-plastic structure is replaced by an elastic structure with the equivalent elastic modulus. Evolution of the ratio of equivalent elastic modulus to the inital Young modulus along bellows half convolution (Fig. 4.9) is shown in Fig. 7.10. It has been obtained for bellows subjected to an important axial stretch of 32 % with respect to the initial free corrugated length. It confirmes that the major part of the convolution remains elastic and that the plastic zones are localised at root and at crest.
The material parameters, β and A, for the damage law (Eq. 7.54), are: $A = 984$ MPa and $\beta = 0.5$ (cf. [39]). The other parameters, that depend on temperature, have been determined previously.

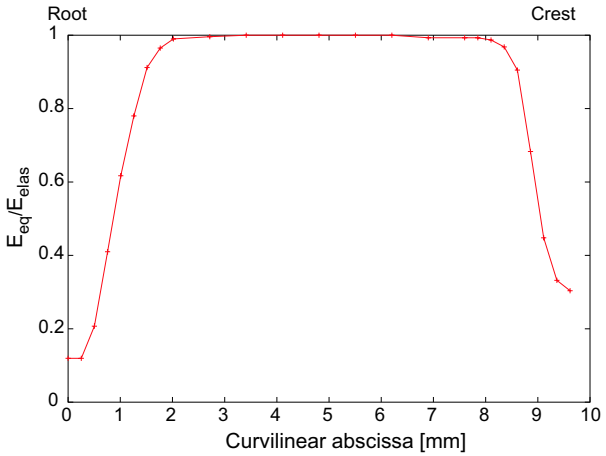

Figure 7.10: Evolution of equivalent elastic modulus along the convolution

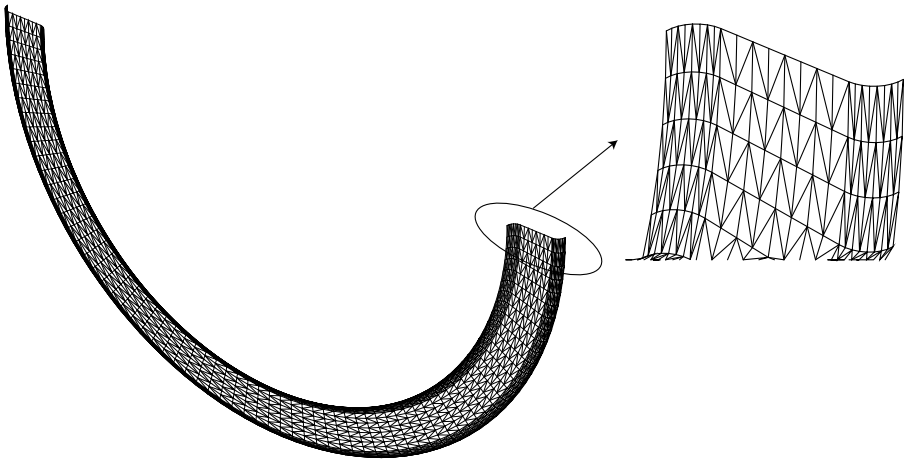

Figure 7.11: Model for the local stability analysis

The local stability is analysed by using a quarter of convolution model (Fig. 7.11). The model is stiffer than the real structure, due to the boundary conditions of symmetry. The effect of plasticity on local buckling is shown in Fig. 7.12. P_{cr}^{0} denotes the critical pressure for the bellows without axial displacement (initial state). The figure 7.12 shows that the elastic buckling pressure decreases non linearly as a function of the displacement, normalized with respect to the free length of bellows (Δ/L_b). It is due to the geometrical nonlinearity. The critical pressure decreases considerably in the elastic-plastic domain. The curve shows an appearance of another buckling mode for large axial displacement. The effect of the yield point on the critical buckling pressure is shown in Fig. 7.13.

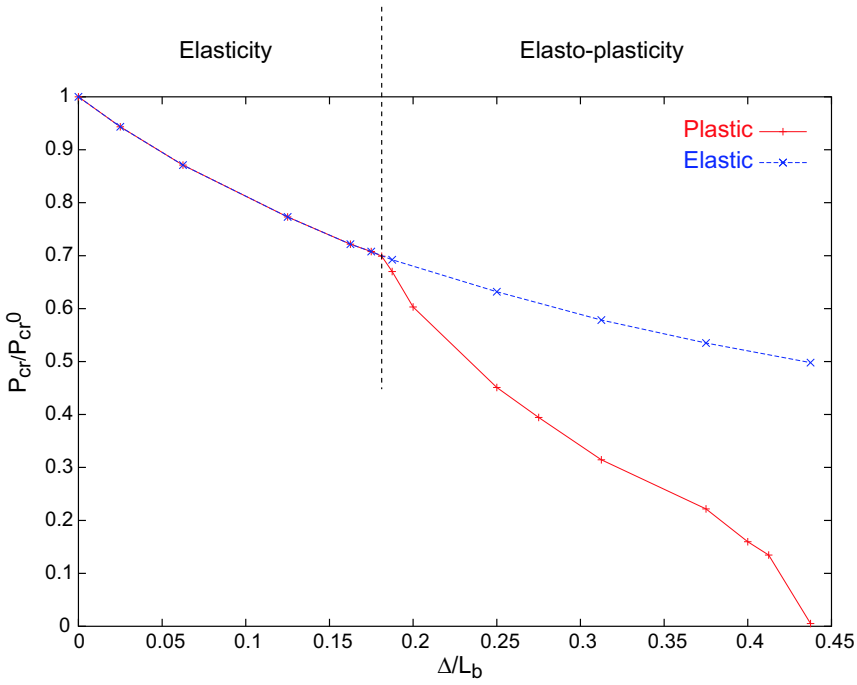

Figure 7.12: Critical pressure for local buckling mode

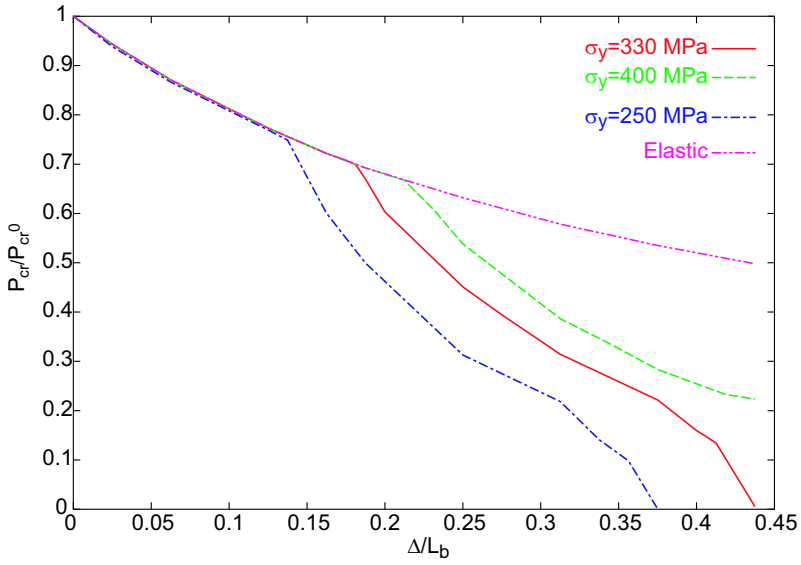

Figure 7.13: Influence of the yield point on the critical pressure for local buckling

Also, the influence of the plasticity is observed for the semi-global stability of the bellows expansion joints. A half bellows model (presented in Fig. 6.2) is used to analyse

semi-global stability. Figure 7.14 shows the critical load for the global stability of bellows under internal and external pressure. Critical values are lower under internal pressure than under external pressure, as expected from the theory of buckling of pressurized pipes [119]. For external pressure in-plane squirm is observed, whereas for internal pressure, the bellows has a mixed buckling mode: column buckling and in-plane squirm. The results can be compared to the EJMA pressure limitations [8], obtained for the same bellows parameters (material and design):

- Limiting design pressure based on in-plane instability, P_{si}, is equal to 0.22 MPa.
- Limiting internal design pressure based on column instability, P_{sc}, is equal to 0.11 MPa.

As for the numerical analysis, the internal pressure is more restrictive in the present case. The EJMA design pressures do not depend on the axial displacement. For small stroke, the limitations, obtained from EJMA code, seem to be conservative. But for large displacements, when high plastic strain fields develope in bellows, the critical buckling pressures obtained from numerical analysis are smaller than the EJMA limitations.
Comparison between semi-global buckling under external pressure and local buckling under external pressure shows that the curves are similar for a certain domain and that local buckling analysis presents higher critical values, as expected (stiffening of the model). The relative difference between the two models is in the order of 15 %. It is worth pointing out that in the elastic domain, the semi-global stability increases significantly with displacement. The change of the slope of the curves is associated with transition to a different buckling mode.
The results can be presented as a function of the normalized critical pressure (Fig. 7.15). In the elastic domain ,the increase of critical pressure as a function of the displacement can reach some 50 % for internal pressure and about 15 % for external pressure.

7.5 Application to the corrugated bellows under cryogenic conditions

7.5.1 Influence of plastic strain induced martensitic transformation

The martensitic transformation induces locally, on one hand, a high hardening of the material which means an increase of the tangent modulus and of the equivalent modulus and, on the other hand, a modification of stresses (notably, an increase in tension).

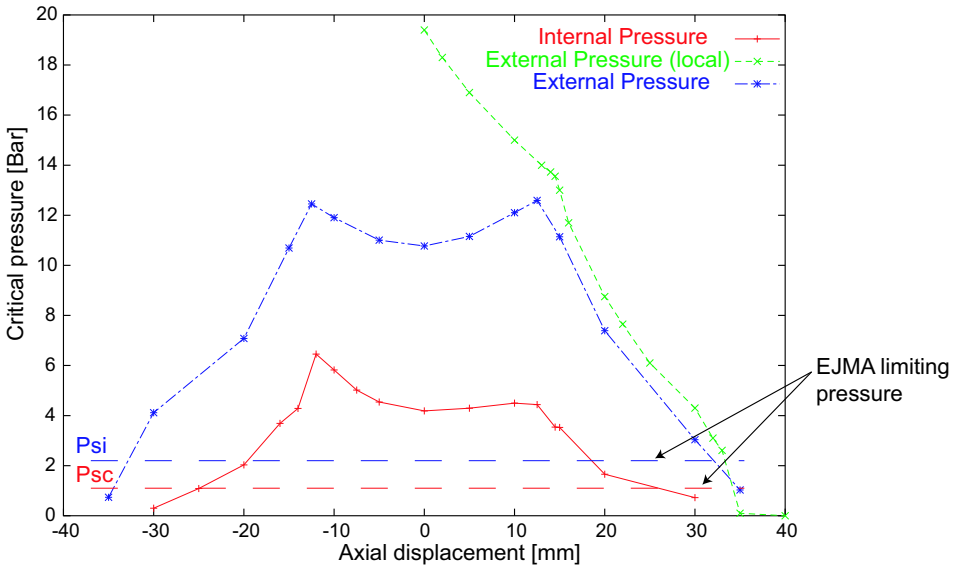

Figure 7.14: Local and global stability of bellows expansion joints under pressure

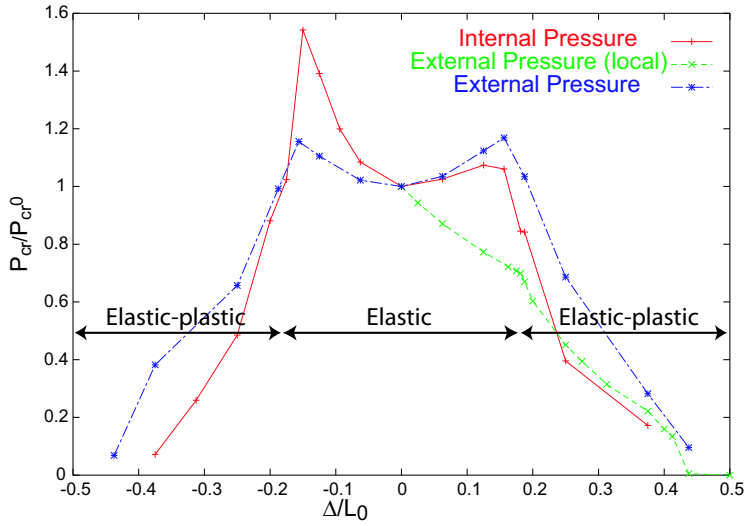

Figure 7.15: Normalized critical pressure for local and global buckling

Thus, the impact of phase transformation on stability is difficult to predict. The evolution of critical pressure for local buckling under external pressure with the number of cycles (so with the phase transformation intensity) is given in Figures 7.16 and 7.17, for tension and compression, respectively. In tensile range, the phase transformation is beneficial for stability (Fig. 7.16), whereas, in compression, the influence is different in two domains (Fig. 7.17): first, the critical pressure decreases for small martensite

content (maximum martensite content in the material not exceeding 8 %) and then it slightly increases. The impact of phase transformation remains small in both cases. The decrease of buckling pressure does not exceed 4 %.

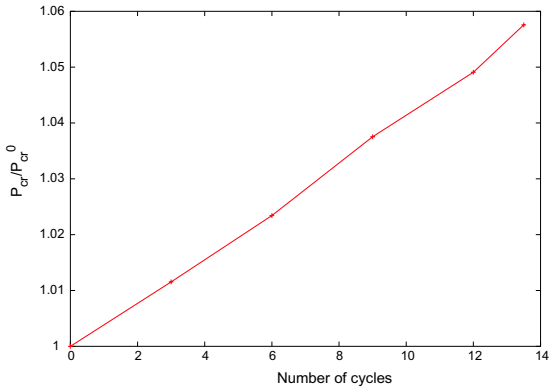

Figure 7.16: Influence of phase transformation on critical external pressure in tension (bellows axially stretched)

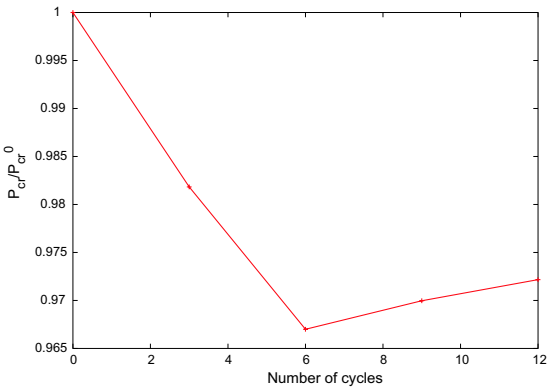

Figure 7.17: Influence of phase transformation on critical external pressure in compression (bellows axially stretched)

7.5.2 Influence of damage evolution on the local buckling of bellows

The damage evolution induces a softening of the material and so of the structure. Critical buckling pressure decreases when the damage increases. The impact of damage remains small, due to the strong localization of plastic straining, and small depth of local plastic zones (Fig. 7.18) and is of the order of 1 % in the present case. The critical pressure decreases slowly as a function of damage parameter except when a buckling mode change occurs.

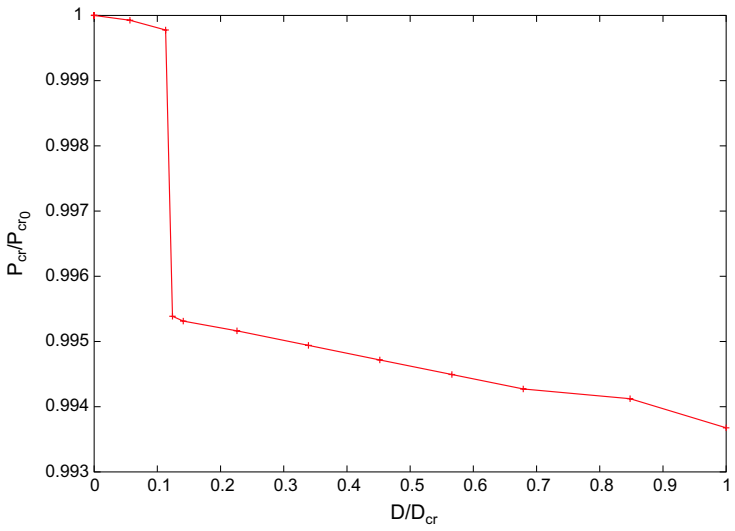

Figure 7.18: Influence of damage evolution on critical external pressure (local buckling)

Chapter 8

Reliability Analysis

About 17000 compensation elements will be used in the LHC interconnections. If one of these units fails, the operation of the accelerator is compromised and it has to be stopped for a repair. Thus, to maximize time for physics, all components of accelerator like bellows expansion joints have to be reliable. Reliability is a new issue in the world of particle accelerators.
Generally, the word reliability implies the notion of endurance and effective operation (run time) of a machine. The objective of reliability analysis is the study of the performance of systems over their lifetimes. Here, by a system is understood a physical structure or a machine that, unless action is taken, will eventually fail. There are different types of failures. At its simplest level a system performs perfectly well until, at some usually unpredictable or random time, it stops working. In a more complex approach, the performance of the system may deteriorate, as for example, mechanical parts wear out. Another possibility is that parts of the system fail allowing the main function of the system to be carried out but at a reduced efficiency (a leak of a beam line bellows), or alternatively increased cost (a leak of a cryogenic bellows).
Mathematical theory of reliability is an applied mathematical discipline based on the concepts of probability theory. It deals with mathematical models of systems, that can be constructed on the basis of the theory and statistically checked. If the model is constructed, then it can be manipulated purely formally. Models of systems can be divided into:

- Event schemes dealing with finite sets of random events,
- Time-dependent shemes, considering the behaviour of a system and its components in time.

Fault trees are amongst the most useful models for the desciption of system failure. Conceived by H.A. Watson in 1961, they form simple and visual tools for describing

and evaluating the events which may lead to failures. They represent graphically and logically how the various combinations of basics events, both failures and normal operations of components, lead to the failure of the system. In case of the LHC mechanical compensation system, the failure of the system is defined by the failure of one of its components (series system).

8.1 General introduction to reliability theory

8.1.1 Probability density functions and identification of parameters

The reliability $R(t)$, of a system S, is the probability that the system performs without failure a specified function under given conditions for a specified time t (cf. [130–133]). Let $T \geq 0$ be a random variable describing the lifetime of a system S. T is the length of the time interval during which the system S operates without failure. The reliability $R(t)$ is the probability that $T > t$ or

$$R(t) = P\left(T > t\right) = 1 - F\left(t\right)$$

where $F\left(t\right) = P\left(T \leq t\right)$ is the distribution function of the lifetime T. $F(t)$ is the failure distribution of the system S. In an independent series system, composed of n_s subsystems, the reliability is given by:

$$R(t) = \prod_{i=1}^{n_s} R_i(t)$$

For a continuous random variable, the failure density function is defined by:

$$f(t) = \lim_{\Delta t \to 0} \frac{F\left(t + \Delta t\right) - F\left(t\right)}{\Delta t} = F'(t)$$

The distribution function of the lifetime T (a positive random variable) may be defined by (cf. [134]):

$$F(T) = \int_0^T f(t)\mathrm{d}t$$

The failure rate funtion λ of S is defined by:

$$\lambda(t) = \frac{f(t)}{R(t)}$$

This function defines the probability that the system S, having reached the age t, will fail during the interval $[t; t + \Delta t]$:

$$\lambda(t) = \lim_{\Delta t \to 0} \frac{P\left(T \in [t; t + \Delta t] \mid T > t\right)}{\Delta t}$$

Generally, failures may be classifed into three categories: early, chance and wearout failures [133]. The lifetime of components is approximately characterised by the failure rate profile shown in Fig. 8.1, known as bathtub diagram. The early failures are

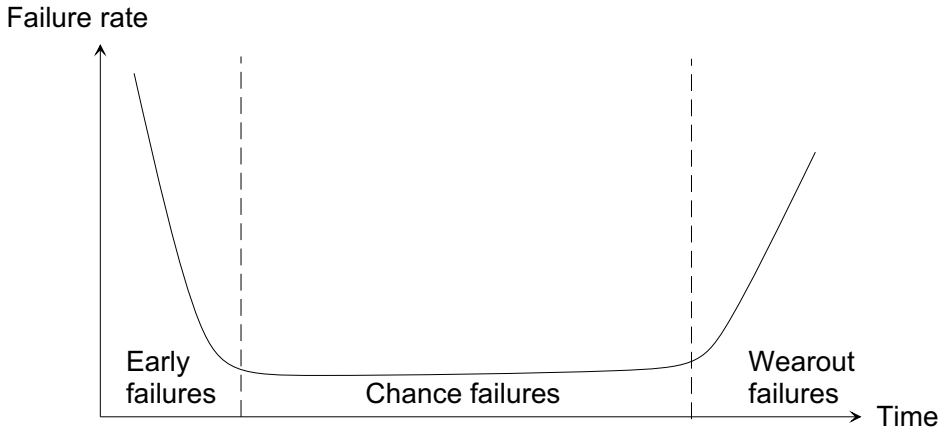

Figure 8.1: Bathtub diagram

controlled by quality of the manufacturing processes, inspections and factory tests (Quality control). The random failure period (chance failures) is normally considered to be the operating period of a system.
The Mean Time To Failure (MTTF), denoted μ, is defined as the expected value of the lifetime T of the system and is given by (cf. [135]):

$$MTTF = E(T) = \mu = \int_0^\infty t f(t) \mathrm{d}t$$

The variance is defined as:

$$Var(T) = \sigma^2 = E\left(T - \mu\right)^2 = \int_0^\infty \left(t - \mu\right)^2 f(t) \mathrm{d}t$$

8.1.2 Reliability of a system and redundancy levels

Mechanical systems are often composed of separate components which may or may not function independently. The reliability of a system depends on two factors: the reliability of its components as well as the manner in which they are connected.

Parallel systems

A parallel system will function if at least one of its components functions. It does not function if all of its components fail. Such system is illustrated by the block diagram

in Fig. 8.2
If n components function independently then the reliability of the system R_S is given

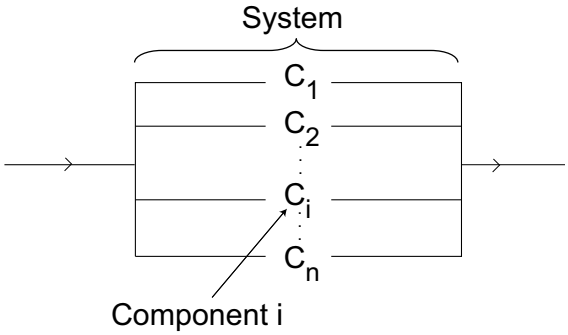

Figure 8.2: Parallel system

by:

$$1 - R_S = \prod_{i=1}^{n} (1 - R_i) \tag{8.1}$$

Series systems

A series system will function if all of its components function. It is represented by the block diagram in Fig. 8.3.

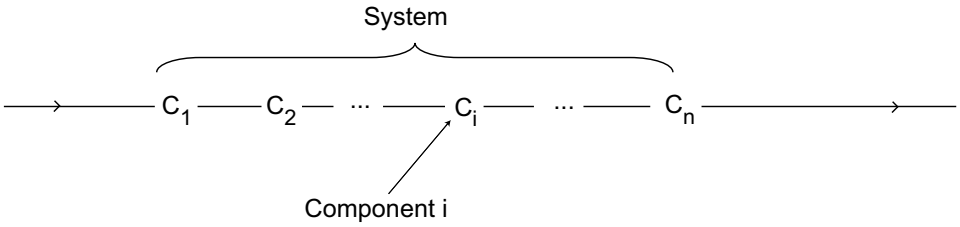

Figure 8.3: Series system

If the components function independently then the reliability of the system R_S is given by:

$$R_S = \prod_{i=1}^{n} R_i \tag{8.2}$$

The LHC compensation system is a series system without any redundancy. Thus, the reliability of the system is given by the eq. 8.2 where n stands for the number of bellows expansion joints in the system S.

8.2 Reliability of the LHC bellows expansion joints

8.2.1 The Weibull probability density function

The Weibull law is one of the well known functions used in the mechanical application to define the reliability of structures. The cumulative distribution function is defined by:

$$F(t) = 1 - exp\left(-\left(\frac{t}{\delta}\right)^{\beta}\right) \tag{8.3}$$

where δ and β denote the scale and the shape parameters, respectively.
The probability density function is given by:

$$f(t) = \frac{\beta}{\delta^{\beta}} t^{\beta-1} exp\left(-\left(\frac{t}{\delta}\right)^{\beta}\right) \tag{8.4}$$

The failure rate is given by:

$$\lambda(t) = \frac{\beta}{\delta^{\beta}} t^{\beta-1} \tag{8.5}$$

The Mean Time To Failure reads:

$$MTTF = \int_0^{\infty} \beta \left(\frac{t}{\delta}\right)^{\beta} exp\left(-\left(\frac{t}{\delta}\right)^{\beta}\right) \mathrm{d}t = \delta\Gamma\left(\frac{1}{\beta} + 1\right) \tag{8.6}$$

with

$$\Gamma(r) = \int_0^{\infty} e^{-x} x^{r-1} \mathrm{d}x \tag{8.7}$$

Identification of the Weibull law from a set of data

Let us consider a set of n times to failure obtained under the same conditions of test:

$$(T_1, T_2, \ldots, T_i, \ldots, T_n)$$

with $T_1 \leq T_2 \leq \ldots \leq T_i \leq \ldots \leq T_n$.
The cumulative distribution function, $\hat{F}_i$, defined for the test i is given by:

$$\hat{F}_i = \frac{i - 0.5}{n} \tag{8.8}$$

The equation 8.3 gives the linear relation between $ln\left(ln\left(\frac{1}{1-F(T)}\right)\right)$ and $ln(T)$:

$$ln\left(ln\left(\frac{1}{1 - F(T)}\right)\right) = \beta ln(T) - \beta ln(\delta) \tag{8.9}$$

The least square linear interpolation, from the pairs $\left(ln(T_i); ln\left(ln\left(\frac{1}{1-\hat{F}_i}\right)\right)\right)$, gives an approximation of the parameter β (from the slope of the line) and δ (from the intersection with the coodinate system and β) of the Weibull law.

In the application to the bellows expansion joints, the random variable is the number of cycles to failure: N. The Weibull distribution function reads:

$$F(N) = 1 - exp\left(-\left(\frac{N}{\delta}\right)^{\beta}\right) \tag{8.10}$$

Number of cycles to failure is regarded as a time-like parameter.

8.2.2 Accelerated life testing of components at cryogenic temperatures

Accelerated life tests of bellows have been carried out by fatigue testing on the machine presented in Annex B. Bellows are tested both at room temperature and in the liquid nitrogen (77 K). They can be installed with a transversal offset. The units are evacuated then the axial displacements are imposed with a frequency of about 1 cycle per 10 s. The stroke of each LHC bellows is given in Table 8.1. The rupture of bellows is declared when a leak is detected.

Type of bellows	Axial stroke [mm]
Nested bellows (14 convolutions)	-30 / +32
Nested bellows (7 convolutions)	-10 / +12
RF contact bellows	-16 / +42.5
Heat exchanger bellows	-16 / +30
Bus bar bellows	-16 / +30

Table 8.1: Axial stroke for different types of LHC bellows

8.2.3 Results of tests. Identification of the parameters of the Weibull law

The Tables 8.2 and 8.3 present the results of the fatigue tests without imperfection (transversal offset or twist), at room temperature and at 77 K, respectively.
The parameters β and δ of the Weibull law (Eq. 8.10) are calculated by using the methodology described in Section 8.2.1. As an example of the method of identification of the Weibull parameters, the RF contact bellows has been chosen. The analysis has been carried out on the set of data obtained at room temperature (Fig. 8.4).

Type of bellows	Number of cycles to failure	Weibull parameters	
		β	δ
Nested bellows (old design) (14 convolutions)	1520 , 1586 , 1640 1760	18.3	1670
Nested bellows (new design) (14 convolutions)	Lack of data (Tests in process)		
Nested bellows (old design) (7 convolutions)	1160 , 1437 , 1640 1928	5.4	1666
Nested bellows (new design) (7 convolutions)	4327 , 5074	9.9	4909
RF contact bellows	4468 , 5317 , 6153 4680 , 4900 , 4426	8.4	5281
Heat exchanger bellows	1636 , 1604 , 1675 1602 , 1645 , 1600	56.9	1642
Bus bar bellows	1100 , 1360	7.4	1301

Table 8.2: Parameters of the Weibull law obtained from fatigue tests at room temperature

Type of bellows	Number of cycles to failure	Weibull parameters	
		β	δ
Nested bellows (old design) (14 convolutions)	2176		
Nested bellows (new design) (14 convolutions)	Lack of data (Tests in process)		
Nested bellows (old design) (7 convolutions)	2565 - 3390 - 3808	5.6	3512
Nested bellows (new design) (7 convolutions)	Lack of data (Tests in process)		
RF contact bellows	Lack of data		
Heat exchanger bellows	2588		
Bus bar bellows	Lack of data		

Table 8.3: Parameters of the Weibull law obtained from fatigue tests at 77 K

8.2.4 Reliability of bellows

Given the parameters of the Weibull law (Table 8.2 and 8.3), the reliability of each bellows expansion joints has been defined with respect to 50 cycles (target value). The results are given in Table 8.4. For all types of bellows, further experiments have to be carried out to improve the statistics and the confidence level. Results obtained from

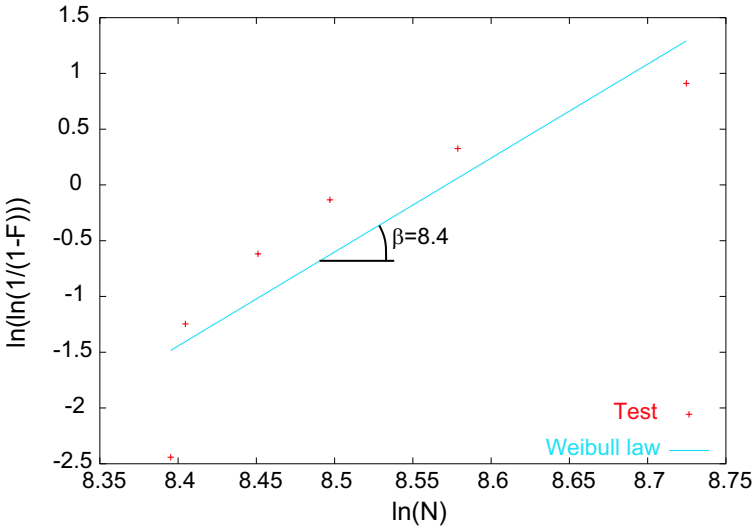

Figure 8.4: Identification of the Weibull parameters for the RF contact bellows at room temperature

two tests have to be confirmed by other experiments Typical evolution of the reliability as a function of the number of cycles is presented in Fig. 8.5.

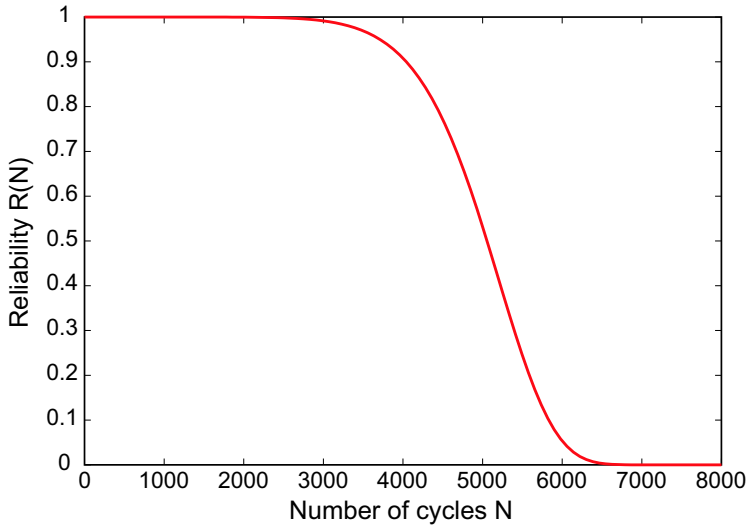

Figure 8.5: Evolution of the reliability as a function of the expected number of cycles for the RF contact bellows at room temeprature

It is worth pointing out that the results have been obtained in laboratory conditions without geometrical imperfections (twist, transveral offset, angular displacement) and

at constant temperature. Even if a limited number of data are available, it is clear

Type of bellows	Expected values	Reliability [%]	
		293 K	77 K
Nested bellows (old design) (14 convolutions)	99.999999	99.99999999...	Lack of data
Nested bellows (new design) (14 convolutions)	99.999999	Lack of data	Lack of data
Nested bellows (old design) (7 convolutions)	99.999999	99.9999994	99.999999995
Nested bellows (new design) (7 convolutions)	99.999999	99.99999999...	Lack of data
RF contact bellows	99.999999	99.99999999...	Lack of data
Heat exchanger bellows	99.999995	99.99999999...	Lack of data
Bus bar line bellows	99.999995	99.999999996	Lack of data

Table 8.4: Reliability of bellows, based on fatigue tests at room temperature and 77 K

that decrease of temperature induces an increase of the number of cycles to failure (Tables 8.2 and 8.3) and of reliability (Table 8.4). It is compatible with the fact that at low temperatures the plastic strain fields are reduced by the increase of yield point.

8.3 Extrapolation to the real cycle

8.3.1 Influence of imperfections

Generally, imperfections can occur during the assembly of the interconnections. Bellows can be subjected to additional transversal offset, angular displacement or twist. To estimate the impact of defect on the reliability of a component, the following methodology is applied:

- Evaluation of the plastic strain range at the critical point in bellows convolutions over the stabilized cycle: $\Delta\epsilon^p$. The plastic strain range on cycle $\Delta\epsilon^p$ can be defined in two different ways:
  - The first has been used and checked by Hamada and Tanaka [136] for bellows subjected to tension-compression cycling. It is defined by:

$$\Delta\epsilon^p = \sqrt{\frac{2}{3}\Delta\underline{\underline{\epsilon}}^p : \Delta\underline{\underline{\epsilon}}^p} \tag{8.11}$$

with $\Delta\underline{\underline{\epsilon}}^p$ defined from the extremum plastic strains on cycle in tension and in compression, $\underline{\underline{\epsilon}}^p_t$ and $\underline{\underline{\epsilon}}^p_c$, respectively:

$$\Delta\underline{\underline{\epsilon}}^p = \underline{\underline{\epsilon}}^p_t - \underline{\underline{\epsilon}}^p_c \tag{8.12}$$

This formulation does not take into account the path in the plastic space. It is applicable when extremum plastic strains are well defined. In case of complex loading path, it would be more difficult to apply.

– The second approach is based on the evolution of the accumulated plastic strain over a cycle. Then, $\Delta\epsilon^p$ has a physical basis and is defined by:

$$\Delta\epsilon^p = \int_{t_c}^{t_t} \sqrt{\frac{2}{3}\dot{\underline{\underline{\epsilon}}}^p : \dot{\underline{\underline{\epsilon}}}^p}\mathrm{d}\tau \tag{8.13}$$

where t_c and t_t denote the values of the time parameter corresponding to the extrema on the stabilized cycle.

Both approaches have been compared with respect to axial cyclic loading. The difference between them does not exceed 1.5 %. However, it may have a significant impact on the fatigue life calculated by using the Manson-coffin formula. Figs. 8.6 and 8.7 show the bellows expansion joint and the boundary conditions for the transversal offset and the angular displacement, respectively.

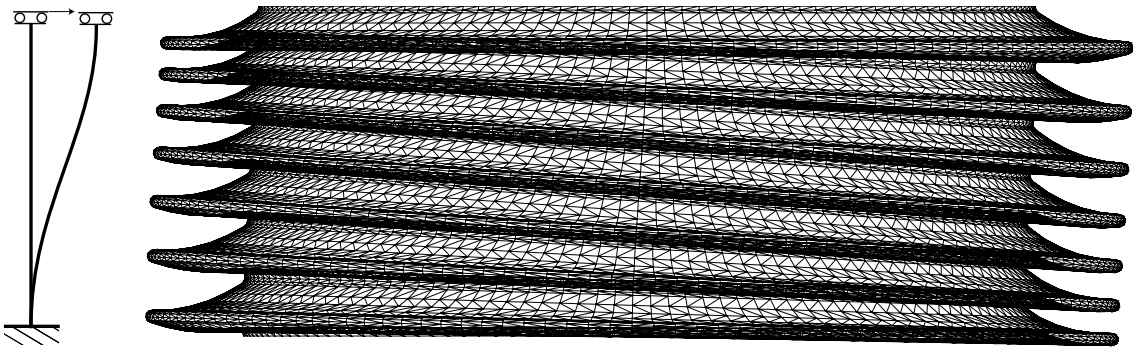

Figure 8.6: Transversal offset (simple beam model on the left)

- The Manson Coffin relationship (Eq. 8.14) is used to determine the impact of geometrical imperfection on the number of cycles to failure (Eq. 8.15).

$$N_f^\beta \Delta\epsilon^p = const \tag{8.14}$$

where N_f denotes the number of cycles to failure, $\Delta\epsilon^p$ stands for the plastic strain range on cycle and β is a material parameter. Thus, the relationship between

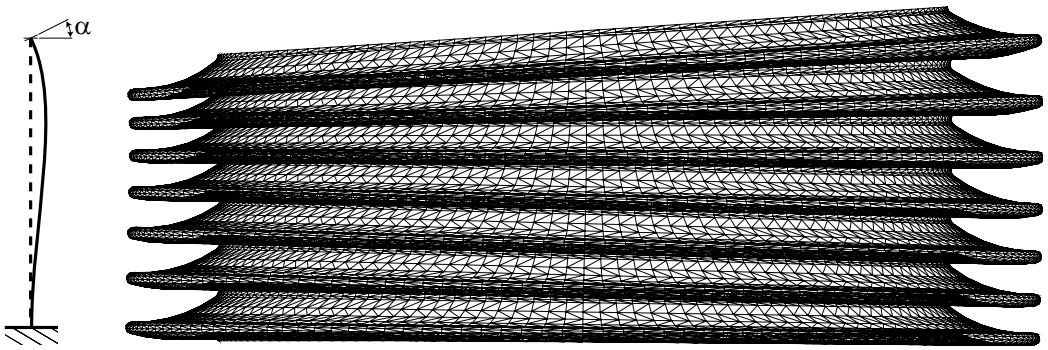

Figure 8.7: Angular displacement (simple beam model on the left)

the number of cycles to failure for the structure with and without imperfection reads:

$$\frac{N_f}{N_{f_0}} = \left(\frac{\Delta\epsilon_0^p}{\Delta\epsilon^p}\right)^{\frac{1}{\beta}} \tag{8.15}$$

The subscript 0 is related to the variables obtained without geometrical imperfection. As an example, Fig. 8.8 shows the decrease of the number of cycles to failure as a function of the angular displacement for the nested bellows with 7 convolutions. The parameter β of the Eq. 8.15 is equal to 0.5.

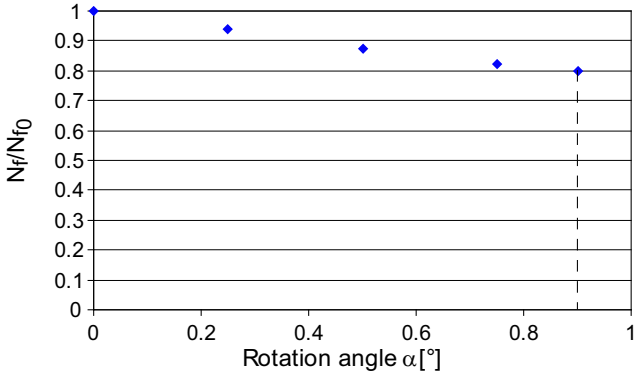

Figure 8.8: Impact of the angular displacement on the fatigue life N_f (short nested bellows)

- Consider that for a component, that has been tested without imperfection, the parameters δ and β of the Weibull function (Eq. 8.3) have been identified from fatigue tests. It is assumed that if each test, leading to a number of cycles to failure N_{f_0} in normal conditions (without imperfections), had been carried

out with an imperfection, the corresponding number of cycles to failure with a defect would have been $N_f = N_{f_0} d$, where d is a constant depending on the imperfection. Then, the Weibull distribution function becomes:

$$F(t) = 1 - exp\left(-\left(\frac{t}{\delta d}\right)^{\beta}\right) \tag{8.16}$$

Fig. 8.9 shows the reliability with and without imperfection. The curve called R(N,1) represents the reliability without defect as a function of the number of cycles, whereas R(N,0.8) illustrates the reliability with an impecfection, that induces the parameter d equal to 0.8 (for example, an angular displacement of 0.9° for nested bellows with 7 convolutions (Fig. 8.8)). The reliability for 50 cycles (target value) is equal to 99.9999994%

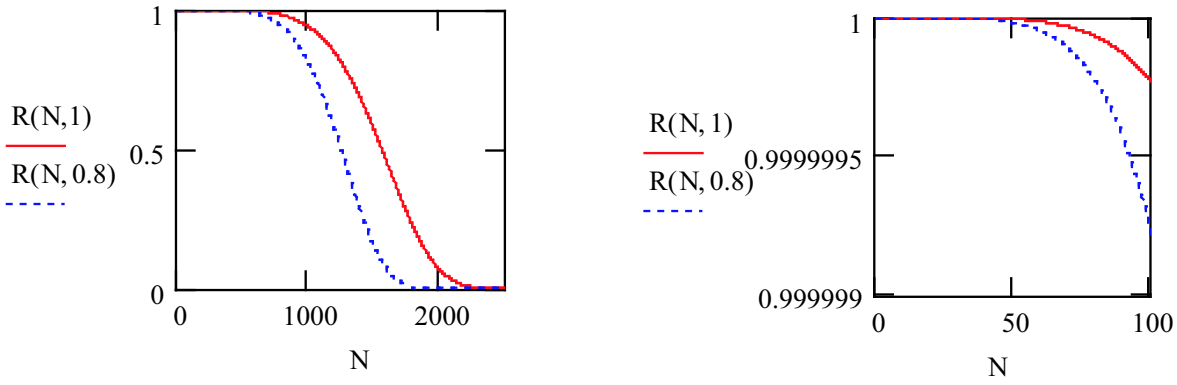

Figure 8.9: Influence of geometrical imperfections on reliability of the short nested bellows

and 99.999998% without and with imperfection, respectively.
The impact of the parameter d on the reliability for 50 cycles is shown in Fig. 8.10. In this particular case, the effect of imperfection seems to be negligible down to around $d = 0.9$ and critical from $d = 0.85$ downwards.
The above presented methodology allows a rough estimate of the decrease of reliability of the components of the LHC mechanical compensation system, resulting from different types of geometrical imperfections like twist, transverse offset or angular displacement. These imperfections usually occur due to misalignement of the magnets, during the process of assembly of the collider and later on during the operation, given the local tunnel floor instabilities.

8.3.2 Influence of thermo-mechanical cycles

All the bellows were tested at constant temperature. Nevertheless, during the operation of LHC they will be subjected to thermo-mechanical cycles: axial displacement

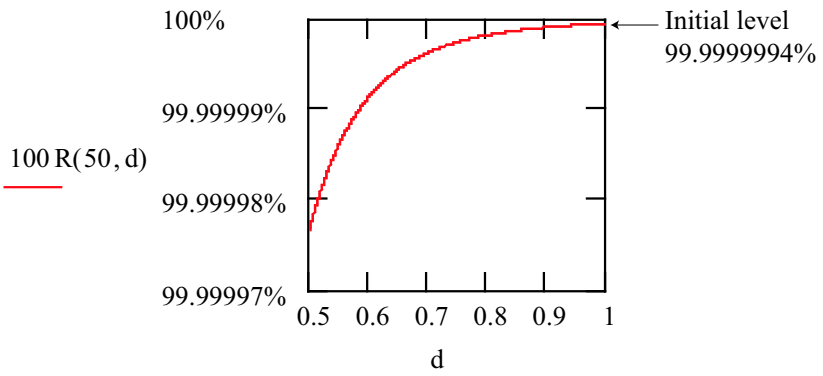

Figure 8.10: Reliability for 50 cycles as a function of the parameter d (related to the imperfection) for the short nested bellows

associated with evolution of the temperature. A linear interpolation of the material properties has been derived out from the experimental values obtained at three temperature levels: room temperature (293 K), 77 K and 4.5 K. The thermal strain field has been taken into account in the analysis. As in the Section 6.3, first the stabilised thermo-mechanical cycle was determined by a FE analysis, then a post-processor evaluation of the damage evolution at the critical point of convolution was carried out.
It seems that for a combined thermo-mechanical cyclic loading, the number of cycles to failure is close to the results obtained at 77 K. Figure 8.11 represents the evolution of the axial displacement as a function of the temperature. The evolution of the axial force, corresponding to this thermo-mechanical load, is shown for the QBX bellows in Fig. 8.12. It is worth pointing out that elastic evolution occurs at sub-zero temperature due to the increase of the yield point.

Table. 8.5 gives the evolution of damage at room temperature, 77 K and for a thermo-mechanical cyclic load between 293 K and 4.5 K, for the QBX bellows.

	293 K	77 K	Combined thermo-mechanical cycle
$D_{cr} = 0.4$	1514	2157	1964
$D_{cr} = 0.6$	1577	2165	2103
$D_{cr} = 0.9$	1678	2178	2227

Table 8.5: Comparison of the fatigue life of QBX bellows for thermo-mechanical cycles and for constant temperature cycles

Several phenomena explain the results:

- Axial displacement is rather constant below 77 K (little thermal contraction). So, the influence of the thermo-mechanical cycles on the fatigue life of bellows can be analysed mainly between 293 K and 77 K.

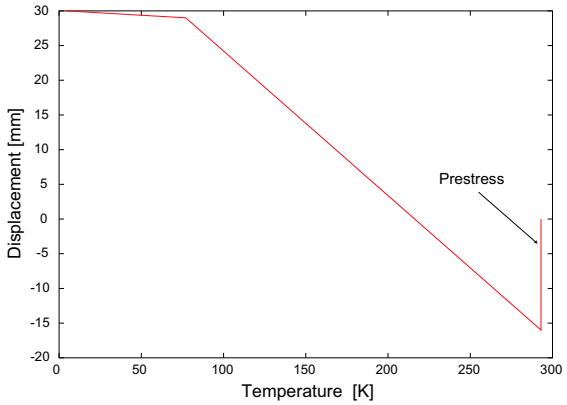

Figure 8.11: Evolution of the axial displacement with the temperature

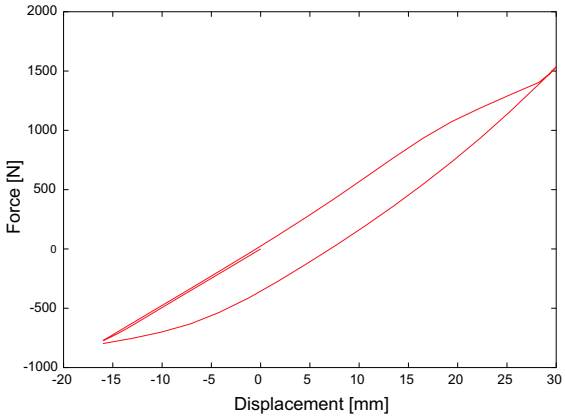

Figure 8.12: Axial force as a function of displacement for thermo-mechanical cycle

- At low temperatures, the plastic strain fields decrease due to the increase of the yield point and the hardening induced by the martensitic transformation. Damage developes slower than at room temperature. The number of cycles needed to reach the damage threshold is higher at low temperature than at room temperature (less dissipation of plastic energy on cycle at low temperature).

The results are valid under all the assumptions made previously for the constitutive model (small strains, ductile damage, plastic strain induced phase transformation)

Chapter 9

Conclusions and perspectives

Thesis presents a number of issues, which are very important for application of bellows expansion joints at cryogenic temperatures:

- Constitutive modelling of ductile materials at cryogenic temperatures,
- Stability of corrugated thin-walled shells (bellows),
- Reliability of bellows expansion joints under cryogenic conditions.

A constitutive modelling of ductile materials at cryogenic temperatures, especially oriented towards the austenitic stainless steels, has been proposed. Based on the classical theory of plasticity (motion of dislocations), it takes into account two phenomena, that occur at low temperatures: plastic strain induced martensitic transformation and ductile damage evolution.

A simplified kinetic law of $\gamma - \alpha'$ phase transformation has been developed for cryogenic temperatures. Hardening of the two-phase material has been studied in the framework of relatively small strain. Classical theory of plasticity has been applied and the relevant elastic-plastic model, based on mixed kinematic/isotropic hardening has been developed. The approach based on homogenization theory has been used in order to define the hardening moduli.

Ductile damage theory has been applied at cryogenic temperatures. Several approaches have been studied: a mesoscopic isotropic model with a damage evolution law as proposed by Lemaitre; a mesoscopic anisotropic model, for which a ductile damage evolution law has been postulated and, finally, a microscopic isotropic model, where damage is defined for both phases (martensite and austenite). Local state variables were defined with localisation relations, obtained from Eshelby's analysis. For each phase separately, an isotropic damage evolution law is used. This approach takes

into account the difference of behaviour of both phases, especially at cryogenic temperatures. The difficulties to identify correctly different parameters of these models lead finally to the choice of the mesoscopic isotropic model.

The material parameters of the damage evolution law and of the plastic strain induced martensitic transformation have been identified at three temperature levels: room temperature (293 K), at liquid nitrogen temperature (77 K) and at liquid helium temperature (4.5 K). Application of the model to the expansion joints shows the development of plastic strain fields at root and at crest of the bellows convolutions, that implies a localisation of the $\gamma - \alpha'$ phase transformation and ductile damage. The amount of the phase transformation depends on the material chemical composition of stainless steel (stability of the alloy), on the temperature and on the accumulated plastic strain. Damage evolution is a function of the temperature, of the stress state and of the accumulated plastic strain.

In the present Thesis, it is assumed that the shape of the yield surface is not affected neither by the texture of the material nor by the phase transformation. No plastic flow induced distorsion of the yield surface is taken into account. The yield surface has been assumed as a function of the second invariant of the stress tensor (Huber-Mises-Hencky concept). Since the damage and the martensitic phase transformation model is coupled to the model of plastic flow (mixed kinematic/isotropic hardening) via the accumulated plastic strain p, it is envisageable to introduce a fully anisotropic description of the plastic flow without reformulation of the damage and the phase transformation equations. For instance, in order to reflect the initial texture of the material the Hill yield surface can be applied. Moreover, the effect of plastic strains on the shape of the yield surface (plasticity induced anisotropy) can be introduced by the more complex formulations like Edelman and Drucker [137], Baltov and Sawczuk [138] or Mróz and Niemunis [139]. Thus, a combination of the initial (texture induced) anisotropy and plasticity induced anisotropy will fully describe the process of plastic flow in thin-walled shell structures.

These two approaches are applicable at cryogenic temperatures, with a limitation in terms of plastic strain rate at sub-zero temperatures. From a critical strain rate, discontinous serrated yielding occurs. Thin shear bands, in which the plastic strain localises, develop in the structure. Shear band development is accompanied by an increase of the temperature. Further analysis has to be carried out to obtain a constitutive modelling describing the phenomenon and applicable in numerical analysis.

Combined plastic strain induced $\gamma - \alpha'$ phase transformation and ductile damage model has been used to determine two failure modes: magnetic failure, which corresponds to an amount of ferromagnetic phase (martensite) higher than a critical value,

and damage failure, that allows to estimate number of cycles to failure for the components subjected to axial cyclic loads, pressure and variations of temperature. The number of cycles to failure is determined by a post-processor after an elastic-plastic analysis. The model is also used to determine global parameters of the interconnections, like axial and transversal forces and their impact on the accelerator alignment. The impact of the material properties on the stability of the bellows expansion joints has been evaluated. Phase transformation is localised at root and at crest of convolutions and its influence on stability remains small. The effect of local and global buckling on the fatigue life has to be studied in the future work. The collapse of structure may induce a strong localisation of plastic strains and may lead to a premature fatigue failure.

The reliability levels of the LHC bellows expansion joints have been determined from accelerated fatigue tests at 293 K and at 77 K. Weibull's law is used to define the cumulative distribution function of lifetime of the components. The impact of geometrical imperfections has been computed and confirmed experimentally for transversal offset. Further experiments have to be carried out to improve the statistics, especialy for the bellows with combined geometrical defects (transversal offset, angular displacement and twist). This study allows to define the tolerances of the assembly of the bellows expansion joints while assuring the required reliability of the components. A new material more stable at cryogenic conditions with respect to the plastic strain induced martensitic transformation and with low inclusion content will be use to manufacture the bellows. An improvement in terms of fatigue life and reliability has been made and leads to a higher safety factor for the LHC mechanical compensation system as well as to increase of availability of the accelerator for physics.

Appendix A

The Erichsen test

A.1 Principle of testing the formability of fine gauge stainless steel sheets

The test of Erichsen is used to cupping test for sheet and strip of low thickness. A sketch of the experimental dispositif is given in Fig. A.1.

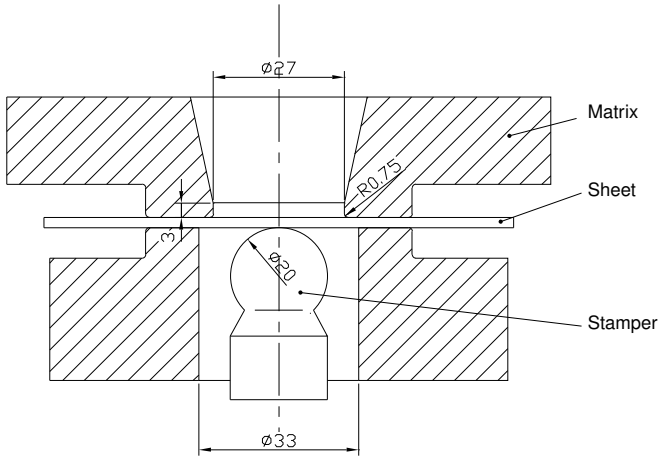

Figure A.1: Experimental set-up for the Erichsen's test

It occurs in the following way:

- The sheet is maintained on the matrix with a force of about 10 kN.
- The spherical stamper deformes the sheet by a translation movement

Lubricant is used to avoid the friction between the sheet and the spherical stamper and the matrix. The test is carried out till the rupture of the probe. So, the penetration is measured.

A.2 Numerical modelling

The test is numerically simulated [140], using a FE code. The test is simulated by an axisymetric model. The processus of large deformations is kinematically controled via the displacement of the stamper. It presents several non-linearities:

- The elastic-plastic behavior of the material
- The contact between sheet and stamper and the matrix

Contact elements with normal stiffness are used between the stamper and the sheet and between the matrix and the stamper.The geometrical non-linearities are taken into account. The deformated shape is given Fig. A.2 after a penetration of 7 mm of the stamper.

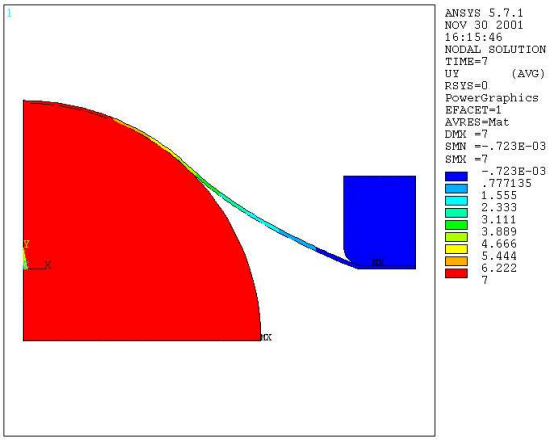

Figure A.2: Deformated shape after a penetration of 7 mm

This simple model allows to determine the stresses, the displacements and the plastic strain field during the process.
At the initial stage of material fabrication, few material parameters are known: the yield point, the ultimate strain, the elongation at rupture (Table A.1). This material properties allows to define a elastic-plastic behavior with the parameters presented in Table A.2. With this modelling, the results are the following (Fig. A.3, A.4).
A simplified criteria is considered: The equivalent stress has to be less than the ultimate

σ_y [MPa]	σ_u [MPa]	$A_5 = \epsilon_{ult}$ %
450	680	47

Table A.1: Material parameters after fabrication

E [GPa]	ν	σ_y [MPa]	H [MPa]
190	0.3	450	480

Table A.2: Material parameters of the elastic-plastic model

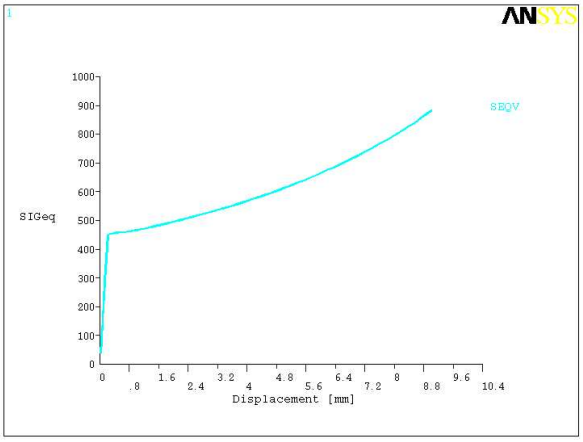

Figure A.3: Equivalent stress as a function of the displacement of the stamper

stress or the accumulated plastic strain has to be less than the elongation at rupture. The criteria reads formally:

$$F\left(\sigma_{eq},\ p\right) =< \sigma_u - \sigma_{eq} >< \epsilon_{ult} - p >$$

with $< . >$ defines by:

$$\begin{cases} < u >= u & \text{if} \quad u \geq 0 \\ < u >= 0 & \text{if} \quad u < 0 \end{cases}$$

The following results are obtained (Table A.3)

Maximum simulated depression	Maximum measured depression
6.4	6.6

Table A.3: Results of the Erichsen test

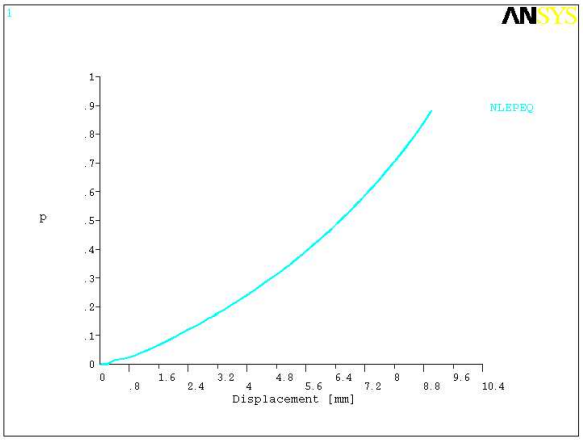

Figure A.4: Accumulated plastic strain as a function of the displacement of the stamper

Appendix B

Accelerated life testing set-up for bellows expansion joints

The machine used to test the bellows expansion joints is schematized in Fig. B.1 and shown in Fig. B.2.

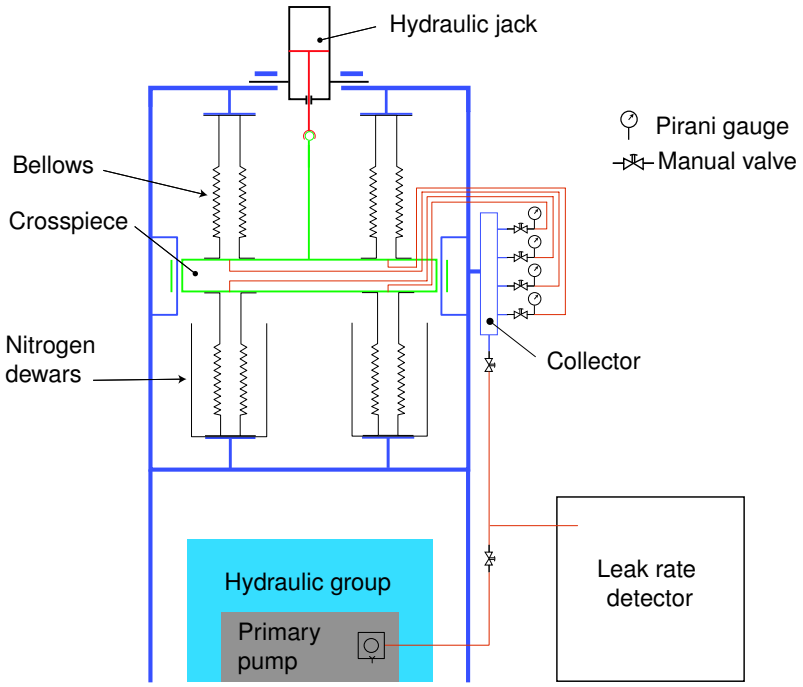

Figure B.1: Test bench

The machine is designed to test 4 bellows, with the ability to test two of them at cryogenic temperature (77 K). The expansion joints, tested at low temperature, are

Figure B.2: Photography of the test bench

installed in an insulated tank, filled of liquid nitrogen.
The translation movement is generated by an hydraulic equipement: hydraulic group (motopump, tank, valve,...), jack and distributor. The jack, into which a displacement sensor is integrated, has an amplitude of 100 mm. The movement is imposed by a consign of speed, which controls the opening of the distributor. The signals, displacement and speed control, are both linked to a PC.
A force sensor may be used to measure the force over a cycle or cycle by cycle. It has a capacity of 2 kN with an accuracy of 0.03 % with respect to 2 kN.
For the fatigue tests, the failure of a bellows, that means the apparition of a macrocrack through the thin-walled shell, has to be detected. It is done via the measurement of the leak rate. Bellows are evacuated, first by a primary pump (the pressure obtained is about 10^{-2} mbar) and then by a turbopump to reach a vacuum less than 2.10^{-3} mbar. The four bellows are linked to a collector. The pressure is measured by Pirani gauge, which principle is to measure the thermal conductance. The leak rate is measured by leak detector based on a mass spectrometer. The output signal is linked to the PC. A failure is declared when the leak rate increases more than a decade with respect to the initial value.

Appendix C

Measurements of magnetic susceptibility

C.1 Magnetostatic properties of material [141]

For a material, in which confined currents develope, the magnetic moment $\vec{m}$ can be defined as follow:

$$\vec{m} = \frac{1}{2}\int_V \overrightarrow{OM} \wedge \vec{j}(M)\mathrm{d}V \tag{C.1}$$

where $\vec{j}$ is the current density.
The magnetisation of the material is defined by:

$$\vec{M} = \frac{\vec{m}}{V} \tag{C.2}$$

The magnetic field is determined from the relation:

$$\mathrm{rot}\vec{H} = \vec{j_0} \tag{C.3}$$

where $\vec{j_0}$ denotes the free current density.
Induction $\vec{B}$ and magnetic field $\vec{H}$ are related with the magnetisation by the relationship:

$$\vec{B} = \mu_0(\vec{H} + \vec{M}) \tag{C.4}$$

The magnetic response of the material (magnetisation) to of magnetic field reads:

$$\vec{M} = \chi\vec{H} \tag{C.5}$$

where χ stands for the susceptibility. Eq. C.4, defining the induction, can reads:

$$\vec{B} = \mu_0\mu\vec{H} \tag{C.6}$$

where μ denotes the relativ permeability and is related to the susceptibility by:

$$\mu = 1 + \chi \tag{C.7}$$

C.2 Magnetisation measurements

C.2.1 Reciprocity theorem [142]

Given the figure C.1, the flux sent by a ponctual magnetic moment $\vec{m}$ into a measure coil is equal to:

$$\phi = \frac{\vec{B}}{I}.\vec{m} \tag{C.8}$$

where $\vec{B}$ is the inductance in the ponctual moment created by a fictiv current I circulating in the measure coil.

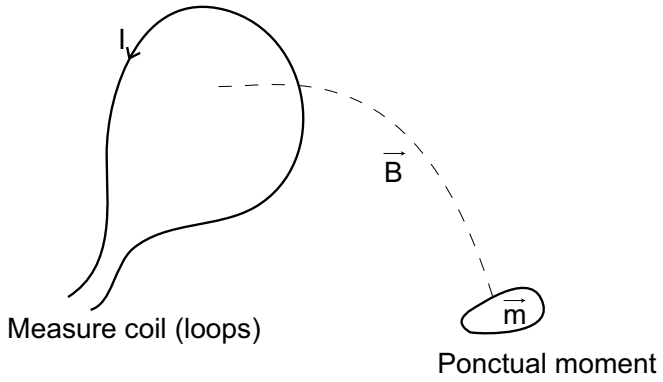

Figure C.1: Evolution of the kinematic and isotropic hardening rates

The induced voltage at the boundaries of the measure coils is given by:

$$e = -\frac{\mathrm{d}\phi}{\mathrm{d}t} \tag{C.9}$$

C.2.2 Magnetometers

The movement of the sample induces magnetic flux variation in the measure coils and so induces a voltage. Different magnetometers, based on different movement of the sample (periodic, monotonic) can be used.
Here, Vibrating Sample Magnetometer (VSM) is presented in Fig. C.2. A sinusoidal alternatif movement is applied to the sample subjected to an inductance due to magnetic field $\vec{H}$ and magnetisation $\vec{M}$. Sensivity of such set-up is $10^{-8} - 10^{-10}$ [A.m^2].
The magnetic field (H) is imposed and the magnetisation (M) is deduces on the basis of the reciprocity theorem. Typical magnetisation curve is shown Fig.C.3 (corresponding here to 1 % strain at liquid helium temperature).

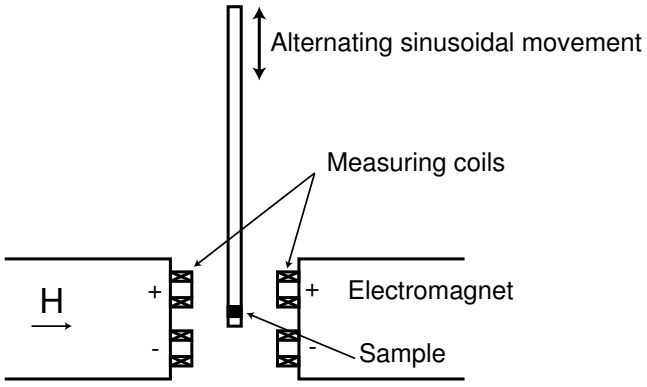

Figure C.2: Vibrating sample magnetometer principle

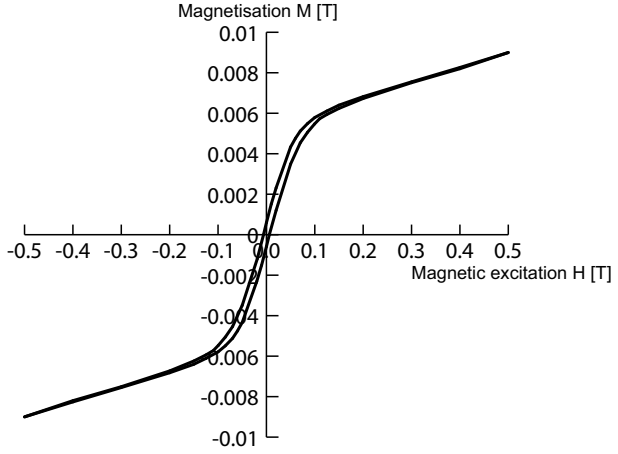

Figure C.3: Typical magnetisation curve

C.3 Susceptibility measurements

Reference diagram Fig. 5.2 in section 5.1.1 is established for a magnetic field of 1000 Oe = 0.1 T. Secant method is used to define the susceptibility for a magnetic field of 0.1 T (Fig. C.4).
Susceptibility is equal to:

$$\chi = \frac{M|_{H=0.1\mathrm{T}}}{0.1} \tag{C.10}$$

The permeability is easily deduced by the equation C.7.
For low ferromagnetic materials, the magnetisation curve presents a small hysteresis. Thus, the secant method gives two values, χ_1 and χ_2, nearly equal.

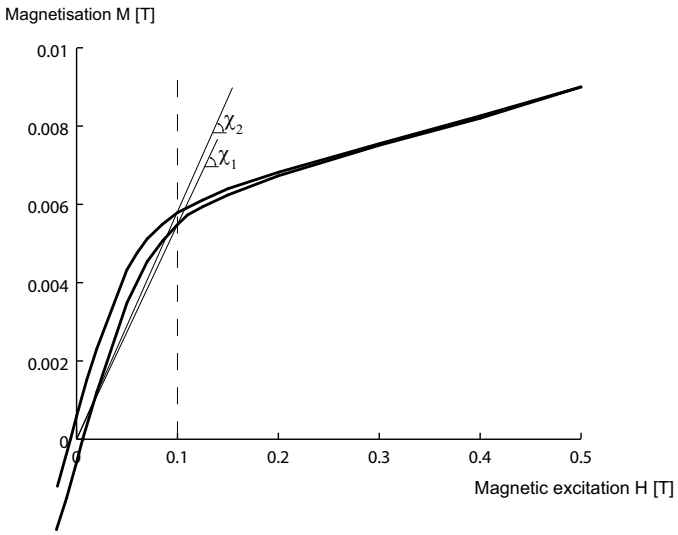

Figure C.4: Secant method

Bibliography

[1] Lefèvre P. and Pettersson T. *The Large Hadron Collider*. CERN (1995).

[2] Skoczen B., Garion C., Jacquemod A., Poncet A., Schauf F., Tock J.-P. *On the reliability oriented optimisation of the LHC interconnections*. Proceedings of the EPAC-02, European Particule Accelerator Conference, Paris, pp. 374–376 (2002).

[3] Skoczen B. *Stability, fatigue and optimization of thin-walled structures under cryogenic conditions: Application in the structural design of colliders and cryogenic transfer lines*. Yellow Report No. 2001-001 CERN (2001).

[4] Garion C., Marquis D., Skoczen B. *Reliability oriented optimum design of the LHC magnet-to-magnet interconnections*. Mécanique et Industries (sent to Editor) (2002).

[5] Coffin L. *A study of the effects of cyclic thermal stresses on ductile metal*. Trans. ASME **76**, pp. 931-950 (1954).

[6] Manson S. *Behavior of materials under conditions of thermal stress*. Technical note No. 1170 National Advisory Committee for Aeronautics (1954).

[7] Axelrad E. L. *On local buckling of thin shells*. Int. J. Non-linear Mechanics pp. 249–259 (1985).

[8] EJMA STANDARDS, *Standards of the expansion joint manufacturers association*. New York (1998).

[9] *Sheets and tubing for special cryogenic applications stainless steel type X2CrNiMo17-12-2 (1.4404, AISI 316L)*. Technical specification No. 525 Ed. 3 CERN (1999).

[10] Suzuki K., Fukakura J. and Kashiwaya H. *Cryogenic fatigue properties of 304L and 316L stainless steels compared to mechanical strength and increasing magnetic permeability*. American society for testing and materials pp. 190–197 (1988).

[11] Morris J. W., Chan J. W. and Mei Z. *The influence of deformation-induced martensite on the cryogenic behavior of 300-series stainless steels*. Cryogenics ICMC supplement **32** (1992).

[12] Larbalestier D. C. and King H. W. *Austenitic stainless steels at cryogenic temperatures, structural stability and magnetic properties*. Cryogenics **13**, pp. 160-167 (1973).

[13] Reed R. P. and Walsh R. P. *Tensile strain rate effect in liquid helium*. Adv. Cryogenic Engineering Materials **34**, pp. 199-208 (1988).

[14] Reed R. P., Walsh R. P. and Tobler R. L. *Strain rate effect on tensile properties at 4K of a vamas round-robin austenitic steel*. Adv. Cryogenic Engineering Materials **36**, pp. 1061-1068 (1990).

[15] Reed R. P. and Simon N. J. *Discontinuous yielding during tensile tests at low temperatures*. Adv. Cryog. Eng. Mater. **36**, pp. 1077-1086 (1990).

[16] Ogata T. and Ishikawa K. *Time-dependent deformation of austenitic stainless steels at cryogenic temperatures*. Cryogenics **26**, pp. 365-369 (1986).

[17] Ogata T., Ishikawa K., Umezawa O. and Yuri T. *Effects of specimen geometry on temperature and discontinous deformation during tensile tests at liquid helium temperature*. Adv. Cryog. Eng. Mater. **34**, pp. 209-215 (1988).

[18] Ogata T., Ishikawa K., Reed R. P. and Walsh R. P. *Loading rate effects on discontinuous deformation in load-control tensile tests*. Adv. Cryog. Eng. Mater. **34**, pp. 233-240 (1988).

[19] Ogata T., Umezawa O. and Ishikawa K. *Low temperature creep behaviour of stainless steels*. Adv. Cryog. Eng. Mater. **36**, pp. 1233-1239 (1990).

[20] Hall E. *The deformation and ageing of mild steel*. Proc. Phys. Soc. London **64B**, pp. 747-753 (1951).

[21] Petch N. *The cleavage strength of polycrystals*. J. Iron Steel Inst. London **174**(1), pp. 25-28 (1953).

[22] Reed R. P., Simon N. J., Purtscher P. T. and Tobler R. L. *Alloy 316LN for low temperature structures: a summary of tensile and fracture data*. International Cryogenic Engineering Conference pp. 15–26 (1986).

[23] Purtscher P. T., Walsh R. P. and Reed R. P. *Effect of chemical composition on the 4 K mechanical properties of 316 LN-type alloys*. pp. 191–198 ().

[24] Simon N. J. and Reed R. P. *Strength and toughness of AISI 304 and 316 at 4 K*. Journal of Nuclear Materials **141**, pp. 44-48 (1986).

[25] Drucker D. *Some Implications of Work Hardening and Ideal Plasticity*. Quart. Appl. Math. **7**, pp. 411-418 (1950).

[26] Drucker D. *A Definition of Stable Inelastic Material*. Journal of Applied Mechanics **26**, pp. 101-106 (1959).

[27] Reed R. P. and Simon N. J. *Discontinuous yielding in austenitic steels at low temperatures*. International Cryogenic Material conference, Boulder, **2**, pp. 851-863 (1988).

[28] Tobler R. L., Beekman D. H. and Reed R. P. (1983) *Factors influencing the low-temperature dependence of yielding in AISI 316 stainless steels*. In *Austenitic stainless steel at low temperatures*, edited by Reed R. P. and Horiuchi T. pp. 135–157.

[29] Ogata T., Ishikawa K., Nagai K. and Umezawa O. *Low cycle fatigue and other mechanical properties of aged 316LN stainless steel at liquid helium temperature*. Adv. Cryog. Eng. Mater. **36**, pp. 1249 (1990).

[30] Obst B. and Nyilas A. *Experimental evidence on the dislocation mechanism of serrated yielding in f.c.c. metals ans alloys at low temperatures*. Materials Science and Engineering **A137**, pp. 141-150 (1991).

[31] Obst B. and Nyilas A. (1998) *Time-resolved flow stress behavior of structural materials at low temperatures*. In *Advances in Cryogenic Engineering (Materials)*, edited by Balachandran B. pp. 331–338.

[32] Institut International du Froid, *Cryogénie. Ses applications en supraconductivité*. Techniques de l'ingénieur (2000).

[33] Delsante M.-L. *Etude du matériau des soufflets du LHC*. DESS Techniques et applications de la physique. University of Grenoble 1, France (2001).

[34] ASTM *Standard Test Methods for Determining the Inclusion Content of Steel*. No. E45-97 (1997).

[35] Garion C., Matot S., Sgobba S., Skoczen B. *Private communication*. Working Group on materials for cryogenic bellows, CERN (2002).

[36] Perrot Y. *Etude de la formabilié de l'acier inoxydable constituants les soufflets d'interconnexion du LHC*. Stage of DUT University of Bordeaux 1, France (2002).

[37] ASTM *Standard Test Methods for Determining Average Grain Size*. No. E112-96 (1996).

[38] Garion C., Matet R. *Private communication*. Working Group on geometry of cryogenic bellows, CERN (2001).

[39] B. Skoczen , *Material and structural stabilty issues at cryogenic temperatures. Application in the structural design of accelerators for particle physics*. Politechnika Krakowska, monograph series, Mechanika 88, Krakow (2002).

[40] Riddone G. *Dimensions, pressures, temperatures and sizing of valves and piping in the LHC machine cryostat and cryogenic distribution line*. Engineering specification No. 90032 CERN (2000).

[41] Garion C., Skoczen B. *Reliability oriented optimum design of the LHC interconnections. Part I: mechanical compensation system*. LHC Project Note No. 245 CERN (2000).

[42] Ortin J. (1997) *Thermodynamics and Kinetics of Phase Transitions: an Introduction*. In *Mechanics of solids with phase changes*, edited by Berveiller M. and Fischer F. D. pp. 1–52.

[43] Stüwe H. P. (1997) *Interaction of Stresses and Strains with Phase Changes in Metals: Physical Aspects*. In *Mechanics of solids with phase changes*, edited by Berveiller M. and Fischer F. D. pp. 53–68.

[44] Garion C., Skoczen B. *Modelling of stainless steels at cryogenic temperatures. Strain induced martensitic transformation*. CRI Technical Note No. CERN/LHC/CRI (2000).

[45] Garion C., Skoczen B. *Plastic strain induced damage evolution and martensitic transformation in ductile materials at cryogenic temperatures*. LHC Project Report No. 509 CERN (2001).

[46] Garion C., Skoczen B. *Constitutive modelling of stainless steel for cryogenic application. Strain induced martensitic transformation*. LHC Project Note No. 252 CERN (2001).

[47] Garion C., Skoczen B. *Modelling of plastic strain induced martensitic transformation for cryogenic applications*. Journal of Applied Mechanics **69**(6), pp. 755-762 (2002).

[48] Garion C., Skoczen B. T. (2001) *Plastic strain induced damage evolution and martensitic transformation in ductile materials at cryogenic temperatures*. In *Advances in Cryogenic Engineering. Proceedings of the International Cryogenic Materials Conference - ICMC, Madison, 2001*, edited by Balachandran B., Gibser D. and Hartwig T. pp. 170–177.

[49] Iwamoto T., Tsuta T. and Tomita Y. *Investigation on deformation mode dependence of strain-induced martensitic transformation in TRIP steels and modelling of transformation kinetics*. Int. J. Mech. Sci. **40**(2-3), pp. 173-182 (1998).

[50] Olson G. B. and Cohen M. *Kinetics of strain-induced martensitic nucleation*. Metallurgical transactions **A**(6), pp. 791-795 (1975).

[51] Narutani T., Olson G. B. and Cohen M. *Constituitve flow relations for austenitic steels during strain-induced martensitic transformation*. Journal de physique **43**(12), pp. 429-434 (1982).

[52] Stringfellow R. G., Parks D. M. and Olson G. B. *Constitutive model for tranformation plasticity accompanying strain-induced martensitic transformations in metastable austenitic steels*. Acta Metallurgica **40**(7), pp. 1703-1716 (1992).

[53] Angel T. *Formation of martensite in austenitic stainless steel*. J. Iron Steel Inst. **177**, pp. 165-174 (1954).

[54] Levitas V. I., Idesman A. V. and Olson G. B. *Condinuum modeling of strain-induced martensitic transformation at shear band intersections*. Acta Mater. **47**(1), pp. 219-233 (1992).

[55] Lebedev A. A. and Kosarchuk V. V. *Influence of phase transformation on the mechanical properties of austenitic stainless steels*. Int. J. of Plasticity **16**, pp. 749-767 (2000).

[56] Fisher F. D., Reisner G., Werner E., Tanaka K., Cailletaud G. and Antretter T. *A new view on transformation induced plasticity (TRIP)*. Int. J. of Plasticity **16**, pp. 723-748 (2000).

[57] Cherkaoui M., Berveiller M. and Lemoine X. *Couplings between plasticity and martensitic phase transformation: overall behavior of polycristalline TRIP steels*. Int. J. of Plasticity **16**, pp. 1215-1241 (2000).

[58] Tomita Y. and Iwamoto T. *Computational prediction of deformation behavior of TRIP steels under cyclic loading*. Int. Jour. Mechanical Sciences **43**, pp. 2017-2034 (2001).

[59] Reed R. P. *Material at low temperatures*. American society for testing and materials (1983).

[60] Cailletaud G. *Une approche Micromécanique Phénoménologique du Comportement Inélastique des Métaux*. Thèse de doctorat d'état, Université Paris 6 (1987).

[61] Cailletaud G. *A Micromechanical Approach to Inelastic Behavior of Metals*. Int. Journal of Plasticity **8**(1), pp. 55-73 (1992).

[62] Pilvin P. *Approches Multiéchelles pour la Prévision du Comportement Anélastique des Métaux*. Thèse de doctorat, Université Paris 6 (1990).

[63] Armstrong P. and Frederick C. *A Mathematical Representation of the Multiaxial Bauschinger Effect*. CEGB Report No. RD/B/N731 Berkeley Nuclear Laboratories (1966).

[64] Marquis D. *Modélisation et Identification de l'Écrouissage Anisotrope des Métaux*. Thèse de $3^{\text{ème}}$ cycle, Université Paris 6 (1979).

[65] Benallal A., Marquis D. *Constitutive Equations for Nonproportional Cyclic Elasto-Viscoplasticity*. Journal of Engineering Materials and Technology **109**, pp. 326-336 (1987).

[66] Tanaka E. *A Nonproportionality Parameter and a Viscoplastic Constitutive Model Taking into Account Amplitude Dependences and Memory Effects of Isotropic Hardening*. European Jounal of Mechanics **13**, pp. 155-173 (1994).

[67] Calloch S. *Essais Triaxiaux Non-Proportionnels et Ingenierie des Modèles de Plasticité Cyclique*. Thèse de doctorat, Université Paris 6 (1997).

[68] Bornert M., Bretheau T., Gilormini P., *Homogénéisation en mécanique des matériaux 1: Matériaux aléatoires élastiques et milieux périodiques*. Hermès Science (2001).

[69] Mori T., Tanaka K. *Average stress in matrix and average energy of materials with mistfitting inclusions*. Acta Metallurgica **21**, pp. 571-574 (1973).

[70] Eshelby J. D. *The determination of the elastic field of an ellipsoidal inclusion and related problems*. Proc. Roy. Soc. **A**(241), pp. 376-396 (1957).

[71] Chaboche J. L. *Cyclic Viscoplastic constitutive equations: Part I - A thermodynamically consistent formulation*. Jour. Applied Mechanics **60**, pp. 813-828 (1993).

[72] Sadough-Vanini A. and Lehr P. *Comportement en fatigue oligocyclique de l'acier inoxydable Z3CN18-20 à 20 et -196 °C* . La revue de métallurgie-CIT/Science et Génie des matériaux pp. 781–788 (1994).

[73] Życzkowski M. *Combined loading in the theory of plasticity*. PWN Polish Scient. Publ. (1981).

[74] Ortiz M. and Simo J. C. *An analysis of a new class of integration algorithms for elastoplastic constitutive equations*. Int. J. for numerical methods in engineering **23**, pp. 353-366 (1986).

[75] Lemaitre J. *Formulation unifiée des lois d'évolution d'endommagement*. C. R. Acad. Sci. **305**(II), pp. 1125-1130 (1987).

[76] Li L. F., Yang K. and Rong L. J. (2001) *Strengthening mechanism of 316LN stainless steel at cryogenic temperatures*. In *Advances in Cryogenic Engineering. Proceedings of the International Cryogenic Materials Conference - ICMC, Madison, 2001*, edited by Balachandran B., Gibser D. and Hartwig T. pp. 165–169.

[77] Horiguchi K. and Shindo Y. (2001) *Validation of a small punch testing technique to characterize the cryogenic fracture properties of austenitic stainless steel welds*. In *Advances in Cryogenic Engineering. Proceedings of the International Cryogenic Materials Conference - ICMC, Madison, 2001*, edited by Balachandran B., Gibser D. and Hartwig T. pp. 178–185.

[78] Lemaitre J. , *A course on Damage Mechanics*. Springer-Verlag, Berlin and New York (1992).

[79] Kachanov L. M. *Time of rupture process under creep conditions*. Iyv. Akad. NAUK. SSR **8**, pp. 26-31 (1958).

[80] Rabotnov Y. N. (1968) *Creep rupture*. In *Proc. XII Int. Cong. Appl. Mech.*, edited by Springer.

[81] Dufailly J., Lemaitre J. *Modélisation et identification de l'endommagement plastique des métaux*. 3$^{\text{ème}}$ congrès français de mécanique Grenoble (1977).

[82] Chaboche J. L. *Continuous Damage Mechanics: A Tool to describe Phenomea Before Crack Initiation*. Nuclear Engineering and Design **64**, pp. 65-72 (1981).

[83] Lemaitre J., Chaboche J.L., *Mécanique des matériaux solides*. Dunod (1996).

[84] Chaboche J.-L. *Sur l'utilisation des Variables d'Etat Interne pour la Description du Comportement Viscoplastique et de la rupture par Endommagement*. Symp. Franco-Polonais de Rhéologie et Mécanique, Krakow (1977).

[85] Chaboche J. L. *Continuum damage mechanics: Part I-General concepts*. Jour. Applied Mechanics **55**, pp. 59-64 (1988).

[86] Lemaitre J., Sermage J. P. *One damage law for different mechanism*. Computational Mechanics **20**, pp. 84-88 (1997).

[87] Murakami S. (1987) *A continuum mechanics theory of anisotropic damage*. In *Yielding, damage, and failure of anisotropic solids*, edited by Boehler J. P. pp. 465–482.

[88] Murakami S. *Mechanical modelling of material damage*. Jour. Applied Mechanics **55**, pp. 280-286 (1988).

[89] Chaboche J. L. (1999) *Thermodynamically founded CDM models for creep and other conditions*. In *Creep and damage in materials and structures*, edited by Altenbach H. and Skrzypek J. pp. 209–283.

[90] Garion C., Skoczen B. *Orthotropic Damage and Phase Transformation in Ductile Materials at Cryogenic Temperatures*. Proceedings of Int. Symp. Anisotropic Behaviour of Damaged Materials, ABDM, Krakow (in print) (2002).

[91] Garion C., Skoczen B. *Combined model of strain induced phase transformation and orthotropic damage in ductile materials at cryogenic temperatures*. International Journal of Damage Mechanics **12**(4), pp. 331-356 (2003).

[92] Botshekan M. Degallaix S. D. Y. and J. P. *Tensile and LCF properties of AISI 316LN SS at 300 and 77 K*. Fatigue & Fracture of Engineering Materials **21**, pp. 651-660 (1998).

[93] Baffie N. S. J. and T.M. M. *Influence of strain-induced martensitic transformation on fatigue shorth crack behaviour in an austenitic stainless steel*. Matériaux & Techniques **5-6**, pp. 57-64 (2000).

[94] Vogt J.-B., Foct J., Regnard C., Robert G. and Dhers J. *Low-Temperature Fatigue of 316L and 316LN Austenitic Stainless Steels*. Metallurgical Transactions A **22A**, pp. 2385-2392 (1991).

[95] François D., Pineau A., Zaoui A., *Comportement mécanique des matériaux. Élasticité et plasticié*. Hermes (1995).

[96] Kröner E. *Zur plastischen verformung des vielkristalls*. Acta Metallurgica **9**, pp. 155-161 (1961).

[97] Berveiller M. and Zaoui A. *Self-consistent schemes for heterogeneous solid mechanics*. Comportements rhéologique et structure des matériaux - CR 15ème Coll. GFR. Paris (1980).

[98] Chaboche J. L. *Continuum damage mechanics: Part II-Damage growth, crack initiation and crack growth*. Jour. Applied Mechanics **55**, pp. 64-72 (1988).

[99] Billardon R., Doghri I. (1989) *Localization Bifurcation Analysis for Damage Softening Elasto-Plastic Materials*. In *Cracking and Damage-Strain localization and Size Effect*, edited by Mazars J. and Bažant Z. pp. 295–307.

[100] Hadamard J., *Leçons sur la propagation des ondes et les équations de l'hydrodynamique*. Hermann A. (1903).

[101] Rice J. R. *The localization of plastic deformation*. Proc. 14th Int. Congress on Theorical and Applied Mechanics, **1**, pp. 207-220 (1976).

[102] Delsante M.-L., Garion C., Sgobba S., Skoczen B. *A study of the plastic strain-induced martensitic transformation in 316L stainless steel at cryogenic temperatures and identification of the relevant constitutive equations*. Journal of Engineering Materials and Technology (under review) (2002).

[103] Delsante M.-L., Garion C. *Private communication*. Working group on characterisation of material for cryogenic bellows, CERN (2001).

[104] Chrysochoos A. *Dissipation et blocage d'énergie lors d'un écrouissage en traction simple*. Thesis of the Université des Sciences et Techniques du Lanquedoc (1987).

[105] Sermage J. P. *Fatigue thermique multiaxiale à température variable*. Thèse de doctorat, Université Paris 6 (1998).

[106] Wilkins M. L. *Calcultation of Elastic-Plastic Flow*. Methods Comput. Phys. **3**, pp. 211-263 (1964).

[107] Zieliński A., Frey F. *On linearization in non-linear structural finite element analysis*. Computers and Structures **79**, pp. 825-838 (2001).

[108] Tomita Y. and Shibutani Y. *Estimation of deformation behavior of TRIP steels - smooth/ringed-notched specimens under monotonic and cyclic loading*. Int. Journal of Plasticity **16**, pp. 769-789 (2000).

[109] Lemaitre J. and Doghri I. *Damage 90: a post-processor for crack initiation*. Comput. Methods Appl. Mech. Eng. **115**, pp. 197-232 (1994).

[110] Lemaitre J., Sermage J.-P., Sauzay M. *Post-processuer de Mécanique de l'endommagement Damage97*. Notice No. 19 LMT, Cachan (1999).

[111] Lemaitre J., Sermage J. and Desmorat R. *A two scale damage concept applied to fatigue*. Int. Journal of Fracture **97**, pp. 67-81 (1999).

[112] Sauzay M. *Effet de surface libre en plasticité confinée: Application à la fatigue à grand nombre de cycles*. Rapport interne No. 224 LMT, Cachan (1999).

[113] Garion C. *Fatigue de l'acier inoxydable austénitique 316L sous un chargement thermomécanique à basse température*. Mémoire de DEA, E.N.S. de Cachan, LMT-Cachan, Université Paris 6 (1999).

[114] Haringx J. *Instability of bellows subjected to internal pressure*. Research Report No. 7 Philips, Eindhoven (1952).

[115] Haringx J. *Instability of thin-walled cylinders subjected to internal pressure*. Research Report No. 7 Philips, Eindhoven (1952).

[116] Skoczen B. *Effect of shear deformation and relaxation of support conditions on elastic buckling of pressurised expansion bellows*. ASME Journal of Pressure Vessel Technology **121**, pp. 127-132 (1999).

[117] Skoczen B. *Mechanical stability of piping systems equipped with bellows expansion joints*. Technical Note EST-ESI No. 03 CERN (1997).

[118] Liapunov A. *The General Problem of Stability of Motion*. Dissertation, Kharkov. Reprinted in Ann. Math. Studies (1949) **17** (1892).

[119] Bažant Z. and Cedolin L., *Stability of structures,*. Oxford University press, New York (1991).

[120] Lagrange J.-L. *Mécanique analytique*. Courier, Paris (1788).

[121] Rayleigh J. *Theory of sound*. Vol. 1 Macmillan. Dover Publications (1945) (1894).

[122] Shanley F. *Inelastic Column Theory*. J. Aero. Sci. **14**(5), pp. 261-268 (1947).

[123] Bažant Z. *Stable states and Paths of structures with Plasticity and Damage*. Jour. Eng. Mech. **114**(12), pp. 2013-2034 (1988).

[124] Ramberg W. and Osgood W. *Description of Stress-Strain Curves by Three Parameters*. Technical Note No. 902 NACA (1943).

[125] Sammari A. and Jullien J. F. *Creep Buckling of Cylindrical Sheels Under External Lateral Pressure*. Thin-walled Structures **23**, pp. 255-269 (1995).

[126] Combescure A. *Formulation of the COMU element in elasto-plasticity*. Research report CEA, France (1985).

[127] Baillis C., Jullien J. F., Limam A. *An enriched 2D modelling of cooling towers. Effect of real damage on the stability under self weight and on the strength under wind pressure*. Engineering Structures **22**, pp. 831-846 (2000).

[128] Gusic G., Combescure A., Jullien J. F. *The influence of circumferential thickness variations on the buckling of cylindrical shells under external pressure*. Computers and Structures **74**, pp. 461-477 (2000).

[129] Combescure A., Gusic G. *Nonlinear buckling of cylinders under external pressure with nonaxisymmetric thickness imperfections using the COMI axisymmetric shell element*. International Journal of Solids and Structures **38**, pp. 6207-6226 (2001).

[130] Høyland A. and Rausand M. *System Reliability Theory*. Wiley-Interscience Publication (1994).

[131] Birolini A. *Reliability Engineering - Theory and Practice*. Springer (1999).

[132] Mitchell O. Locks, *Reliability, Maintenability and Availability Assessment*. Hayden book (1973).

[133] Kovalenko I., Kuznetsov N. and Pegg P. *Mathematical theory of reliability of time dependent systems with practical applications*. Chichester Wiley (1997).

[134] Ross M. *Introduction to probability model*. Academic Press (1997).

[135] Kinney J. *Probability - An introduction with statistical applications*. Wiley (1997).

[136] Hamada M. and Tanaka M. *A consideration on the Low-cycle Fatigue Life of Bellows*. Bull. JSME **17**(163), pp. 41-49 (1974).

[137] Edelman F. and Drucker D. C. *Some extensions to elementary plasticity theory*. J. Frankl. Inst. **251**, pp. 581-605 (1951).

[138] Baltov A. and Sawczuck A. *A rule of anisotropic hardening*. Acta. Mech. **1**, pp. 81-92 (1965).

[139] Mróz Z. and Niemunis A. (1990) *On the Description of Deformation Anisotropy of materials*. In *Yielding, Damage and failure of anisotropic solids*, edited by Boehler J. P. pp. 171–186.

[140] Garion C. and Skoczen B. *Définition des paramètres de la matière 316L à partir d'essais Erichsen, pour les soufflets des interconnexions* . LHC-CRI Technical Note No. 337748 CERN (2002).

[141] Trémolet de Lacheisserie E. and al., *Magnétisme 1: Fondements*. EDP Sciences (2000).

[142] Trémolet de Lacheisserie E. and al., *Magnétisme 2: Matériaux et applications*. EDP Sciences (1999).